5-2014

Atomic Structure of the Vicinal Interface between Silicon Carbide and Silicon Dioxide

Peizhi Liu
University of Tennessee - Knoxville, pliu5@utk.edu

To the Graduate Council:

I am submitting herewith a dissertation written by Peizhi Liu entitled "Atomic Structure of the Vicinal Interface between Silicon Carbide and Silicon Dioxide." I have examined the final electronic copy of this dissertation for form and content and recommend that it be accepted in partial fulfillment of the requirements for the degree of Doctor of Philosophy, with a major in Materials Science and Engineering.

Gerd Duscher, Major Professor

We have read this dissertation and recommend its acceptance:

Kurt E. Sickafus, Yanwen Zhang, Gong Gu, John R. Dunlap

Accepted for the Council:

Carolyn R. Hodges

Vice Provost and Dean of the Graduate School

(Original signatures are on file with official student records.)

Atomic Structure of the Vicinal Interface between Silicon Carbide and Silicon Dioxide

A Dissertation Presented for the

Doctor of Philosophy

Degree

The University of Tennessee, Knoxville

Peizhi Liu

May 2014

DEDICATION

To Mom and Dad

ACKNOWLEDGEMENTS

Many people helped me on my way to PhD. I would like to acknowledge all of them sincerely. First of all, I wish to express my sincere gratitude to Dr. Duscher, my advisor, who gave me the opportunity to further my graduate study in UT and to carry on my research in his group. Dr. Duscher taught me personally on lab operating, data analyzing and paper writing with his patience, enthusiasm, and enormous knowledge. I cannot achieve my PhD degree without his help. Besides my advisor, I would like to thank the rest of my committee members: Dr. Sickafus, Dr. Zhang, Dr. Dunlap and Dr. Gu for their encouragement, technical support, and insightful comments.

My research has been supported by the National Science Foundation Grant Opportunities for Academic Liaison with Industry (NSF GOALI). I would like to thank Dr. John R. Williams and members in his group at Auburn University, including Dr. Yogesh K. Sharma, Dr. Ayayi C. Ahyi, and Dr. Tamara Isaacs-Smith, who provided samples to me. And I also want to express my appreciation to Dr. Sokrates T. Pantelides, Dr. Xiao Shen, Dr. Sarit Dhar, Dr. Leonard C. Feldman, and Dr. Gang Liu for their valuable comments and discussions on the NSF GOALI meeting. I acknowledge the Joint Institute for Advanced Materials, the University of Tennessee and the Division of Materials Sciences and Engineering, Office of Basic Energy Sciences of the U.S. Department of Energy for the use of state-of-the-art TEM and STEM.

I’m grateful for advice and assistance from my lab colleagues in Dr. Duscher’s group, past and president: Dr. Guoliang Li, Dr. Ritesh Sachan, Dr. Chen Wang, Ondrej Dyck, Mengkun Tian and Jingxuan Ge. I have greatly benefited from the discussions with them, both in techniques and scientific thinking.

Last but not the least, I’m very grateful to my families and friends, who encourage and support me throughout my life.

ABSTRACT

The interface between silicon carbide (SiC) and silicon dioxide (SiO_2) is generally considered to be the cause for the reduced electron mobility of SiC power devices. Previous studies showed an inverse relationship between the mobility and the transition layer width at SiC/SiO_2 interface. In this research the transition region at the interface was investigated with atomic resolution transmission electron microscopy (TEM) and electron energy-loss spectroscopy (EELS).

From a tilting series of high resolution TEM imaging and a through focal series of Z-contrast imaging, the 3D atomic structure of the SiC/SiO_2 vicinal interface was constructed. The vicinal interface was revealed to consist of atomic steps and facets deviating from the ideal off-axis cut plane, which caused the atomic scale roughness of the interface. This is in strict contrast to previous studies that concluded on a chemical composition change.

During the Z-contrast imaging, simultaneous EELS spectra were collected at the interface. A new model based method was developed to quantify these EELS spectra more precisely. Composition profiles of Si, C and O across the interface were extracted from the spectra. Composition profiles showed that the transition region was due to the vicinal interface and its atomic scale roughness but minimal stoichiometric change. Compositions calculated with a chemometrics approach conformed that the interface was stoichiometric. The transition layer width had an intrinsic value of ~2 nm viewed from the step edge-on direction. In addition, the interface of oxide layers grown on an on-axis cut substrate was examined with the same method mentioned above. The results showed the on-axis cut interface had the same composition fluctuation region as the off-axis cut interface viewing from the step edge-on direction.

The roughness is directly correlated with processing conditions and the material system may have an intrinsic local roughness. This atomic scale roughness of the interface is limiting the electron mobility and reliability of SiC based devices.

Keywords

TEM/STEM, EELS, Vicinal interface, Roughness, Mobility

Table of Contents

List of Tables

List of Figures

Chapter 1. INTRODUCTION

1.1. Brief history of SiC and SiC based MOSFETs

Silicon Carbide (SiC) has wandered through the space for billions of years, but was not discovered until 1810 by a Swedish chemist Jöns Jacob Berzelius. It is so rare on earth that its natural mineral was first found almost 80 years later than the synthesized. Berzelius reported his synthesized SiC in 1824. Tens of years later American chemist Edward Goodrich Acheson produced SiC from carbon and corundum. He named it as "carborundum" and gave it the chemical formula "SiC". Very soon, in 1893, Acheson patented his method and the manufacture of bulk SiC became wide-scale. Natural SiC crystal was first found in 1893 as a small component of the Canyon Diablo meteorite in Arizona by Dr. Ferdinand Henri Moissan, after whom the material was named in 1905. That is why mineralogists call natural SiC moissanite [1].

During the first half of the 20th century most of the synthesized SiC was used as an abrasive in grinding wheels because of its excellent mechanical property. However SiC are better suited than diamond for electronic purposes because of its superior thermal and electronic properties. In 1907 H. J. Round produced the first light emitting diode (LED) by applying 10 V on a SiC crystal, shining yellow green luminescence at the cathode. However, it did not attract enough interests on people because of the difficulty of single crystal SiC growth. Until the 1950s, a sublimation process was developed which produced comparatively pure SiC suitable as a semiconductor material. Since then, the development of SiC as an electronic material on a world-wide basis has been phenomenal. In 1955 Jan Anderson Lely presented a new concept of growing high quality SiC crystals, which made it to be a more popular semiconductor material than Si and Ge. However, it was still too hard to purify a single crystal SiC. In 1978 Yu. M. Tairov and V. F. Tsvetkov managed to produce single crystal SiC with high purity by seeded sublimation growth [2]. Then the SiC wafer was born. And yellow LEDs made from 3C-SiC were manufactured in the Soviet Union in the 1970s. In 1987 high-quality epitaxial SiC wafers

were performed at low temperatures on off-axis cut substrates using “step-controlled epitaxy”. Cree Inc. was founded in 1989, as a result of this breakthrough. This American company manufactured the first commercial blue LED on 6H-SiC. Since then the commercial products such as SiC based Schottly diode product line and high frequency metal–oxide–semiconductor field-effect transistors (MOSFETs) have hit the market [3, 4].

1.2. Physical properties of SiC

Silicon carbide has many excellent physical and chemical properties and plays a very important role in the materials family. Because of its low density, high hardness and high strength SiC can be used as an abrasive material for cutting and polishing purposes. Because of its high thermal conductivity, high melting temperature, low thermal expansion coefficient SiC can be made into rotors of turbochargers, blades of gas turbines, bearings, annular seals, heat exchangers and so on. SiC has a very good chemical stability. It is the only ceramic that is resistant to hydrofluoric acid. Excellent optical properties of SiC make it widely used in Si-base photoelectric devices, antireflection films of solar batteries, window materials and short wave LED devices. SiC has a good anti-radiation performance and therefore it is a very important structure material in nuclear engineering. SiC can be coated on nuclear fuel particles. Besides giving a structure support to the nuclear fuel, SiC is the main diffusion barrier to the release of fission products.

SiC is a wide band-gap IV–IV compound, and its electrical properties can be tuned from insulating to conducting by doping. It plays a very important role in semiconductor materials used in electronic devices. Crystal parameters and some main properties of SiC and Si [5-7] are listed in Table 1-1. Because of its large breakdown electric field, large saturated electron drift velocity and large thermal conductivity, SiC is expected to be an advanced material for the new generation high-power, high-temperature and high-frequency microelectronic devices. Compared with Si based devices, SiC base devices can work on a much severer environment. At present, SiC is considered to have the best trade-off between intrinsic properties and commercial maturity [8].

Table 1-1 Physical properties of silicon and silicon carbide

	Si	**3C-SiC (β)**	**4H-SiC (α)**	**6H-SiC (α)**
Space group	$Fd\bar{3}m$	$F\bar{4}3m$	$P6_3mc$	$P6_3mc$
Lattice constants (Å)	5.431	4.360	3.073; 10.053	3.073; 15.11
Density ρ (g/cm^3)	2.3290	3.21	3.21	3.21
Bulk modulus (GPa)	97.6	250	220	220
Thermal conductivity κ (W/(cm·K))	1.5	3.6	3.7	4.9
Breakdown electric field strength E_c (MV/cm)	0.25	1.2	3.2	~4
Dielectric constant ε	11.8	9.66	9.7	9.7
Band gap E_g (eV)	1.12	2.38	3.26	3.02
Electron mobility μ (cm^{-2}/Vs)	1350	~900	~800	~500
Saturation velocity (10^7 cm/s)	1	2	2	2

1.3. Crystal Structure of SiC

SiC is the only stable intermediate compound in the Si-C binary system. SiC is a covalence compound and is stacked up with SiC_4 or CSi_4 tetrahedral unit, shown in Fig. 1-1. In the tetrahedral unit carbon and silicon atoms are bonded together with the bond length of 1.89 Å, and carbon atoms (or silicon atoms) are separated 3.08 Å away from each other. The C-Si bond has sp^3 hybridization with a little amount of polarization. The electronegativity of carbon and silicon is 2.55 and 1.90 respectively, and the ionic character of C-Si bond is about 12%.

SiC crystals can be treated as stacking of double atomic planes of silicon and carbon. Many poly-types of SiC are because of various stacking ways of the 6 fundamental double atomic plane of silicon and carbon, shown in Fig. 1-2 [9, 10]. Since H. Baumbauer first used the word “poly-type” in 1912 to describe the ability of SiC to crystallize into different forms varying only in their hexagonal layer stacking order in one direction, more than 200 poly-types of SiC have been found. Till 2005 an equation that described the relationship between the poly-type thickness and the number of hexagonal layers in the poly-type stacking suggested that there is a natural limit for the number of poly-types of SiC [11]. Different successive layer arrangements give rise to cubic (C), hexagonal (H), or rhombohedral (R) unite cells. The main types of silicon carbide ceramics are α-SiC and β-SiC. α-SiC is name for SiC of wurtzite structure (based on hexagonal structure) and rhombic structure, such as 2H-SiC, 4H-SiC, 15R-SiC etc. β-SiC has a zinc blende structure (face centered cubic structure). α-SiC is a stable phase of high temperature. 6H structure is the stable phase at high temperature. 4H structure is the equilibrium phase at lower temperature, with 15R being stable over a surprisingly wide range in between. Other higher order poly-types are likely to be equilibrium phases around the phase boundaries of 15R with 6H and 4H structure. The cubic structure is not stable at any temperature but it can be understood as a local constrained equilibrium during crystal growth [9]. The distance (lattice parameter a) between neighboring silicon or carbon atoms of poly-types with a hexagonal frame is approximately 3.08 Å, and the distance between two double-atomic layers is 2.54 Å. The height of a hexagonal unit cell, c, varies between the different poly-types. The ratio c/a, thus, differs from poly-type to

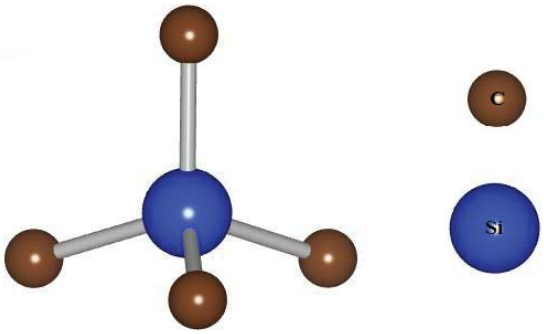

Fig. 1-1. Tetrahedral unit in SiC

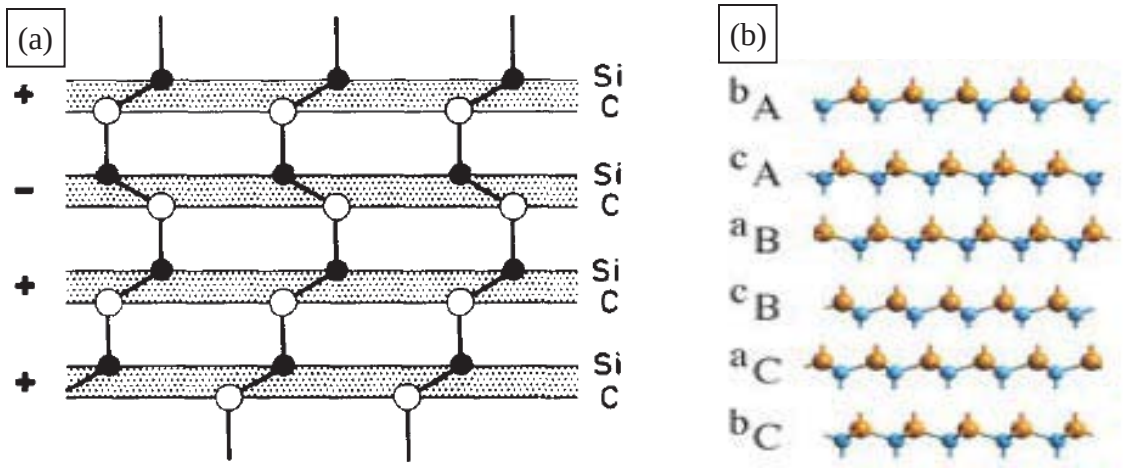

Fig. 1-2. Stacking of Si-C double layers. (a) Stacking of identical atomic double layers of SiC in two orientations, labeled plus and minus according to the direction of the bond in the layer [9]. (b) 6 fundamental bilayers in SiC [10].

poly-type, but is always close to the ideal for a closed packed structure. This ratio is for instance approximately 1.641, 3.271 and 4.908 for the 2H-, 4H- and 6H-SiC poly-types, respectively. The lattice parameter of β-SiC (3C-SiC) is 4.3596Å. Table 1-2 is stacking sequences, lattice parameters and densities of different SiC poly-types [6], and Fig. 1-3 shows the unit cell of 3C-, 4H- and 6H- SiC respectively.

Because of the layered structure of SiC, the high quality SiC wafers can be produced by epitaxy growth, which is the basis for device fabrication. SiC based MOSFET is one of new power devices developed in recent years.

Since the thermal oxidation layer of SiO_2 is amorphous, it does not have a definite crystal structure as crystalline SiC. SiO_2 layers grown by dry oxidation method have a density of 2.27 g/cm^3 [12], which is close to the density of α-quartz (2.65 g/cm3). Therefore, the crystal structure of α-quartz was used to represent the SiO_2 oxidation layer in the analysis of this research. α-quartz is in the trigonal crystal system, and has a space group of $P3_121$ or $P3_221$, with the lattice parameter a = 4.913 Å and c = 5.405 Å. A unit cell of α-quartz is shown in Fig. 1-4. The Si atom density is 48.27 nm^{-3} in SiC and 26.55 nm^{-3} in α-quartz. The number of SiC unit formula per cubic nanometer in SiC crystal is 48.3, compared with 26.6 SiO_2 unit formulas per cubic nanometer of α-quartz.

1.4. SiC based MOSFETs

In the coming years power electronic device will play a growing role for reducing the energy consumption in the world. The power electronic apparatus gives higher efficiency than by using traditional methods such as motor-generator sets and rheostatic control. It's estimated that 20% of global energy demand can be saved by improving the energy efficiency of power electronics [13]. SiC is one of excellent wide band gap materials for high temperature, high frequency and high power electronics. The major parameters (such as maximum operating temperature, maximum reverse voltage, admissible current density and switching speed) of SiC devices are substantially superior to those of silicon devices, in some instances by an order of magnitude: Maximum operating temperature

Table 1-2 Stacking order, lattice parameters and densities of different SiC poly-types

poly-types	stacking order	lattice parameters / Å			density /g·cm^{-3}
		a	b	c	
3C	ABC…	4.359	4.359	4.359	3.215
2H	AB…	3.081	3.081	5.031	3.219
4H	ABAC…	3.081	3.081	10.061	3.215
6H	ABCACB…	3.081	3.081	15.092	3.215
15R	ABCBACABACBCACB…	3.073	3.073	37.700	-
21R	-	3.073	3.073	52.780	-
33R	-	3.073	3.073	82.940	3.240

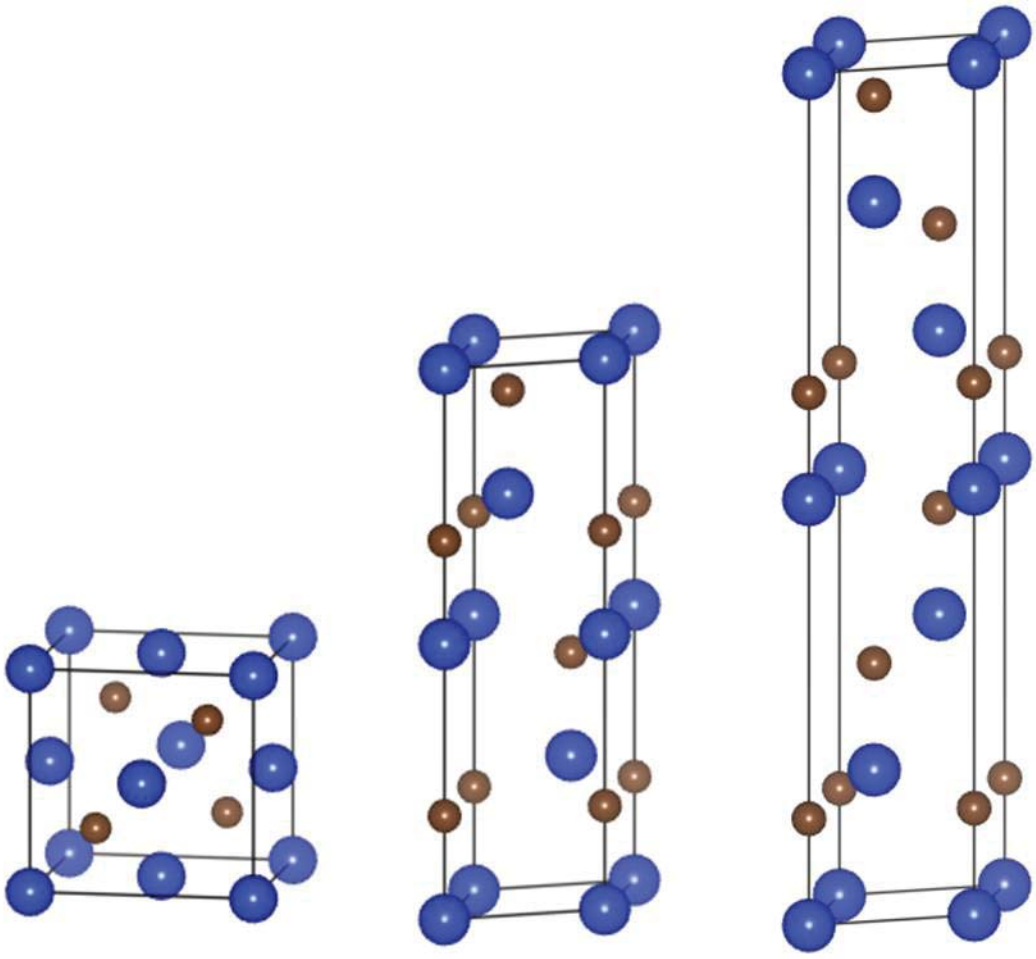

Fig. 1-3 Unit cell of 3C-, 4H- and 6H- SiC

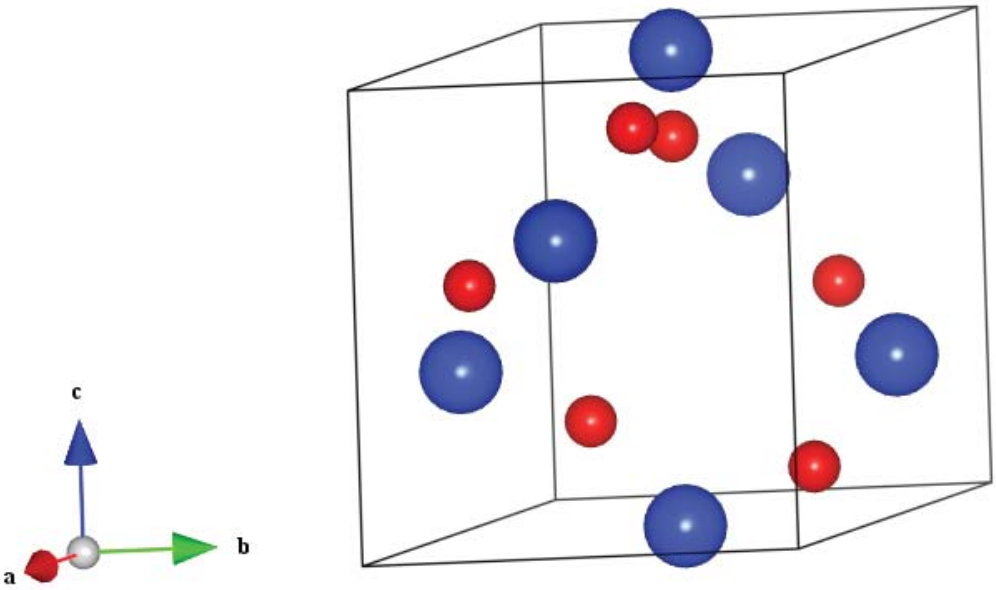

Fig. 1-4 Unit cell of α-quartz

for SiC junctions can reach 1000 °C, the current density is up to approximately 10^3A/cm^{-2}, the reverse voltage can go to 1000 V and the switching speed is in the range of 10^{-8}-10^{-9} s [14]. Its native oxide (SiO_2) insulating layer is the same as Si based devices, which makes the device fabrication process easier compared with other wide band gap semiconductors.

The first power MOSFET structure commercially introduced by the power semiconductor industry was the double-diffused or D-MOSFET structure. A 10 kV, 5 A 4H-SiC power DMOSFET was reported by Ryu et al. [15] in 2006, and A demonstration of 1200 V, 60A 4H-SiC DMOSFETs had been made by Hull et al. [16] in 2008. Fig. 1-5(a) shows an evolution of Cree's SiC DMOSFETs. As shown, the devices fall into 10 kV and 1.2 kV devices with currents ranging from 10 A up to 67 A [17]. Now quite a few new power SiC MOSFETs packaged devices are available from Cree. Fig. 1-5(b) is a SiC power

device produced in Cree (CMF20120D, N-Channel Enhancement Mode, 1200V, 42A) [18]. However, all these devices have not yet reached the expected optimal performances, due to some scientific and technological open issues related to surfaces and interfaces.

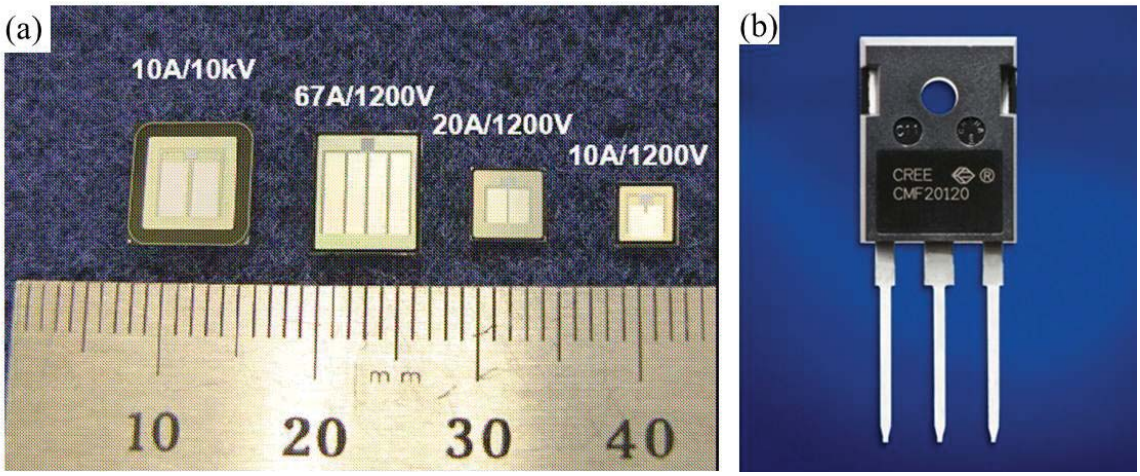

Fig. 1-5 (a) DMOSFETs developed at Cree Inc. [17]. (b) a commercialized SiC power MOSFET device at Cree Inc.

1.4.1. Operation Principle of MOSFETs

The operation of metal oxide semiconductor field effect transistor is based on the field effect, which means an electron field penetrates in to a semiconductor. As shown in Fig. 1-6 (a), when a voltage V is applied on a parallel metal plate capacitor, free conducting electrons with charge $-Q$ will be readily transferred from anode to the cathode metal plate. Electrons accumulate on the surface of cathode and positively charged metal ions with charge $+Q$ expose on the anode surface. A built-in electric filed E is built to balance the

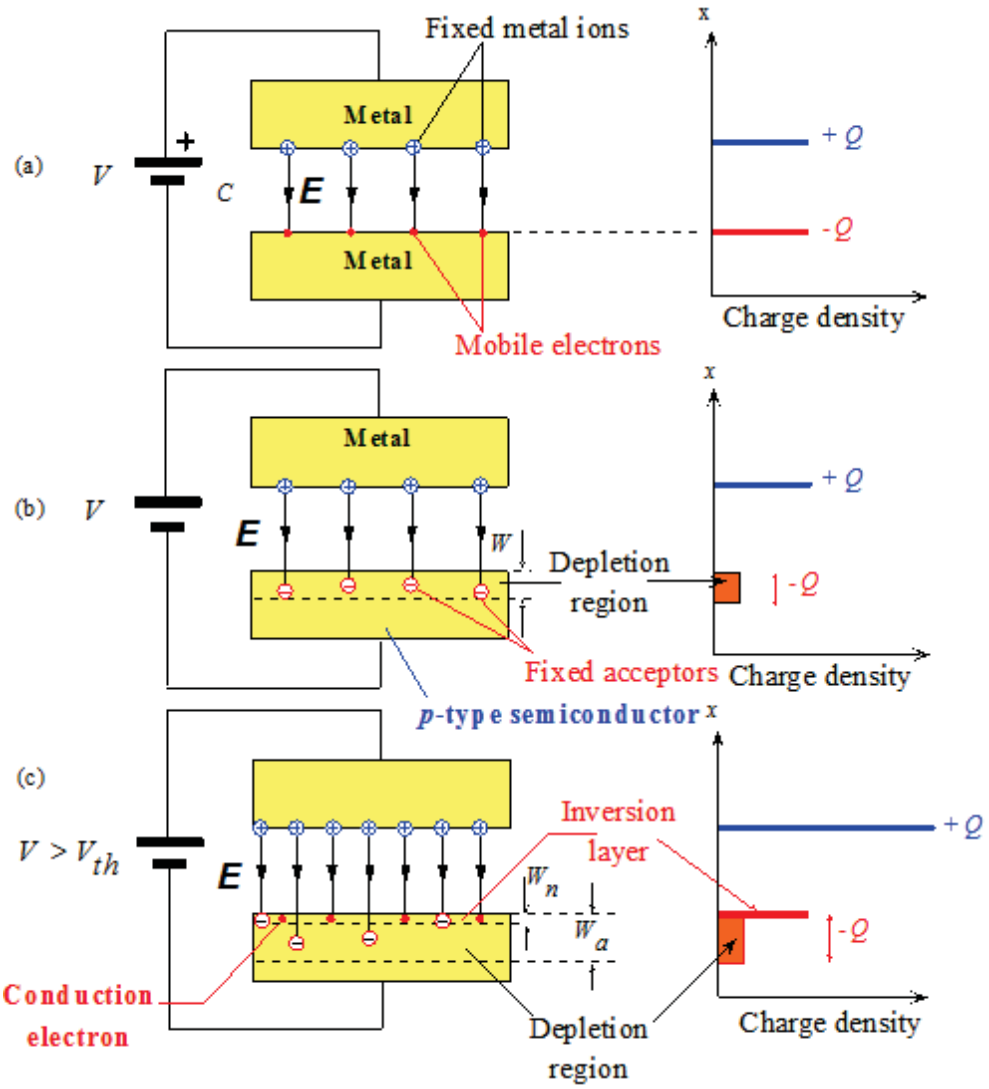

Fig. 1-6 The field effect [19]

applied field. The built-in field does not penetrate into the metal but terminates at the metal surface. If the cathode metal plate is replaced by a p-type semiconductor, shown in Fig. 1-6 (b), the surface metal ions with charge $+Q$ and the negatively charged acceptors with charge $-Q$ will form the built-in electric field. Since there is not a sufficient number of acceptors at the surface, acceptors in bulk must be exposed. That means the built-in field will penetrate into the semiconductor and a depletion layer is formed. The penetration depth is depended on the doping concentration. If the voltage increases, $-Q$ also increases and penetrates more into the semiconductor. However it becomes more difficult to make up the charge $-Q$ by simply extending the depletion layer width into the bulk. It becomes more favorable to attract conduction electrons into the depletion layer and form a thin electron layer near the surface. The charge $-Q$ is now made up of the fixed negative charge of acceptors in W_a and conduction electrons in W_n, as shown in Fig. 1-6(c). Since the electron concentration in the electron layer exceeds the hole concentration and this layer is within a normally p-type semiconductor, it is called an inversion layer. The operation of MOSFETs is based on the field effect and the inversion layer is the conducting channel in MOSFETs.

The basic structure of a MOSFET was depicted in Fig. 1-7. An aluminum electrode, a SiO_2 insulator layer and a *p*-type semiconductor form the metal-insulator-semiconductor structure. The metal electrode is called the gate (G). Two n^+ doped regions at the ends of the MOS device form the source (S) and drain (D). Usually a metal contact is also made to the substrate. The MOSFET device is normally worked on a reverse bias with source and substrate connected. When a positive voltage less than the threshold voltage V_{th} is applied to the gate (G), $V_{GS} < V_{th}$, as shown in Fig. 1-8 (a), the p-type semiconductor under the gate develops a depletion layer and no current can flow for any positive V_{DS}. As soon as V_{GS} is increased beyond V_{th}, an n-channel inversion layer is formed with in the depletion layer under the gate, as shown in Fig. 1-8 (b). This n-channel links the two n^+ regions of source (S) and drain (D). When a small V_{DS} is applied, a drain current I_D flows between S and D. The voltage variation along the channel is form zero at A (source end) to V_{DS} at B (drain end). The gate to the n-channel voltage is then V_{GS} at A and V_{GD} at B, and one can have

$$V_{GD} = V_{GS} - V_{DS}$$

As V_{DS} increases, the voltage at B (V_{GD}) decreases and thereby causes less inversion. Eventually when the V_{GD} decreases below V_{th}, the inversion layer at B disappears and a depletion layer is exposed, as illustrated in Fig. 1-8 (c). At that point the n-channel becomes pinched off and the I_D becomes saturation, as shown in Fig. 1-8 (D).

As $V_{DS(sat)}$ depends on V_{GS}, so does I_{DS}. The overall I_{DS} versus V_{DS} characteristics for various fixed gate voltages V_{GS} of a typical enhancement MOSFET is shown in Fig.1-9 (a). It can be seen that there is only a slight increase in I_{DS} with V_{DS} beyond $V_{DS(sat)}$. The I_{DS} versus V_{DS} when $V_{DS} > V_{DS(sat)}$ characteristics are shown in Fig.1-9 (b). It is apparent that as long as $V_{DS} > V_{DS(sat)}$, the saturated drain current I_{DS} in the source-drain circuit is almost totally controlled by the gate voltage V_{GS} in the source-gate circuit. This is what constitutes the MOSFET action. Variations in V_{GS} then lead to variations in the drain current I_{DS}, which forms the basis of the MOSFET amplifier [19].

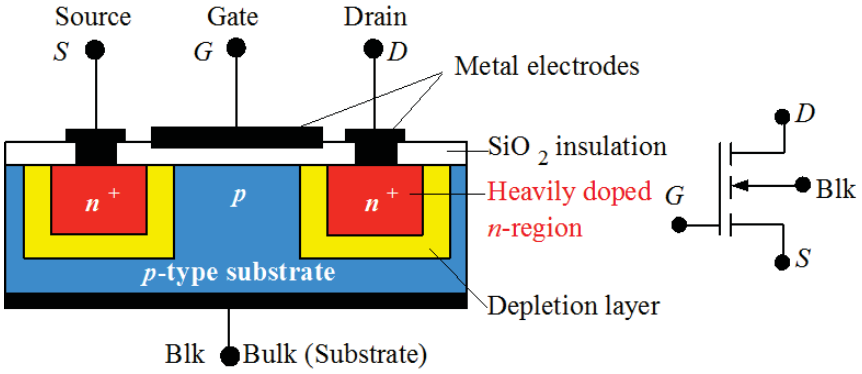

Fig. 1-7 The basic structure of the enhancement MOSFET and its circuit symbol [19]

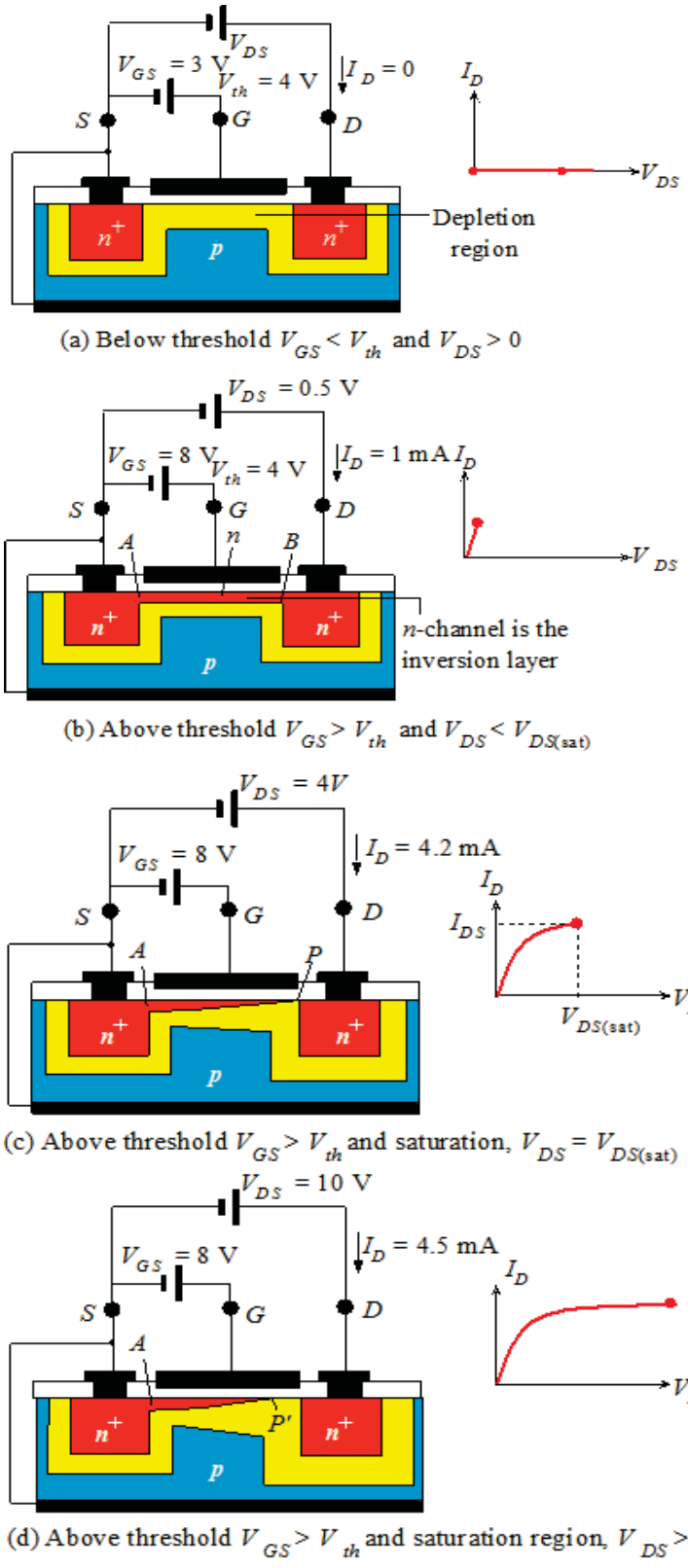

Fig. 1-8. Illustration of MOSFET operation principle [19]

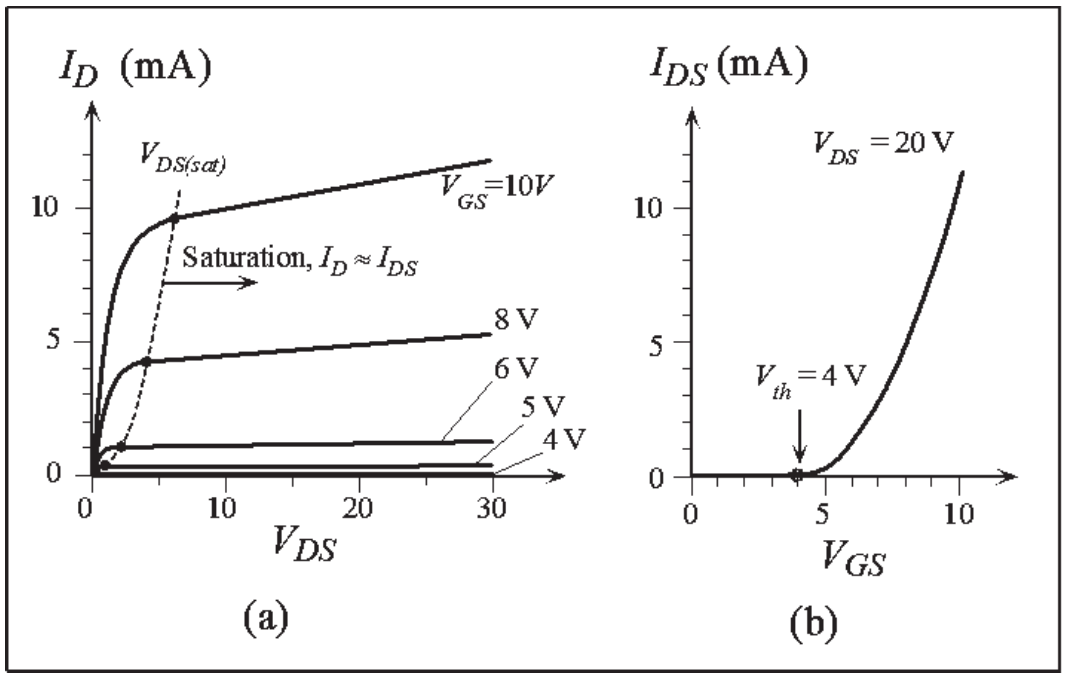

Fig. 1-9. Typical current-voltage characteristics of MOSFETs [19]

1.4.2. Fabrication of SiC MOSFETs

Large high quality SiC bulk crystal growth technology has brought about tremendous progress in the last decade. Four inch SiC wafers in diameter have been successfully demonstrated and three-inch SiC wafers have already been brought to market. Single crystal SiC wafers could be fabricated by epitaxial growth techniques such as physical vapor deposition (PVD), chemical vapor deposition (CVD), liquid phase epitaxy (LPE), vapor-liquid-solid (VLS) method and molecular beam epitaxy (MBE) [10]. Source, drain, and gate were fabricated on single crystal SiC wafer to form a MOSFET. Source and drain regions were formed by ion implantation to a total doping concentration of ~ 10^{15}

cm^{-3}. Gate oxides were thermally grown by dry or wet oxidation process, which is similar with silicon thermo oxidation [20]. That makes most of the processing techniques in the Si industry applicable to SiC devices. After the thermo oxidation, a postoxidation annealing (POA) process followed. At last metal electrodes and contacts were evaporated onto the source, gate, drain region and the substrate [21, 22].

High temperature oxidation of SiC to SiO_2 layer was performed over 1100 °C. Two oxygen atoms arrive at the SiC/SiO_2 interface and kick a carbon atom to form two Si-O-Si bridges. The process is enabled by the fact that the Si-Si distance in SiC is 3.1 Å, essentially the same as the preferred Si-Si distance in a Si-O-Si bridge. The ejection of the carbon atom can be facilitated by a third O, whereby a CO is emitted. SiC has the same native oxide as Si, and can, therefore, be singled out as the most promising choice for MOSFETs. However, SiC/SiO_2 interfaces are much more complex than Si/SiO_2 interface, and the trap densities at the SiC/SiO_2 interface are too high to give acceptable channel mobilities in SiC based MOSFETs. Channel electron mobilities in SiC were found to be about two orders of magnitude smaller than their bulk values. In contrast to Si, bulk mobilities are only cut by a factor of two in the channel adjacent to the Si/SiO_2 interface [23].

Postoxidation annealing, or postoxidation passivation, has been a key factor in the high performance SiC MOSFETs. It is an annealing process after the oxide growth, and it can be carried out in various ambient (such as NO, N_2O, NH_3, and H_2). The postoxidation annealing was believed to reduce the interface state density, and thus the electron mobility at the interface increased. Nitrogen oxide (NO) passivation is one of the most efficient ways to increase the channel electron mobility of SiC MOSFETs to 35 cm^2/Vs [24, 25]. Then phosphosilicate glass (PSG) passivation is another annealing method developed in recent years. It use phosphorous from P_2O_5 to passivate the SiO_2 layers. The PSG passivation is more effective than NO passivation, which can provide peak motilities of 80–90 cm^2/Vs. However, P_2O_5 converts the SiO_2 layer to phosphosilicate glass. The PSG is a polar material that introduces voltage instabilities which negate the benefits of lower interface trap density and higher mobility [26]. In general, after all

kinds of passivation, channel electron mobility of the MOSFET sample is still far from the theoretical limit, suggesting that further improvements are possible.

The biggest challenge in the development of SiC MOSFET devices is low electron mobility at SiC/SiO_2 interface. The low electron mobility at the interface dominates the channel resistance, which caused a high on-resistance of the SiC MOSFET. During the fabrication of SiC base MOSFETs, many processing conditions can affect the electron mobility at the SiC/SiO_2 interface. The process variables includes implant anneal temperature and ambient, oxidation procedure, postoxidation annealing, type of gate material and high-temperature ohmic contact anneal. Among these process conditions, postoxidation anneal produced a significant increase in mobility, while other process variables have little impact on the mobility [27].

1.4.3. Channel mobility in SiC MOSFETs

SiC MOSFETs show rather low channel electron mobility [28-30] (30 - 50 cm^2/Vs) compared to the mobility of bulk SiC. SiC/SiO_2 interface is generally considered to be the cause for the reduced mobility of SiC devices. The poor mobility behavior can be caused by a large density of electrically active defects present at the SiO_2/SiC interface, like carbon clusters, or near-interface traps [21, 22] and the surface morphology of the SiC substrate [31]. However, the exact structure and chemical composition of the interface is still under debate. Chang K. C. et al.[32, 33] reported a high carbon concentrations at the SiO_2/C-face SiC interface but no carbon excess showed in the Si-face interfaces. Nitrogen with an equivalent content of 1 monolayer of atoms was also detected at interface [32], however the bonding status and effect on the channel mobility are unclear. Recently, electron energy-loss spectrum (EELS) results from Zheleva et al. [34] and Biggerstaff et al. [35] showed an excess carbon non-stoichiometric transition layer in the interface, which may cause the decrease of the channel mobility. The C/Si ratio of the carbon rich transition layer could be as high as 1.2. The calculation result from Shen X. et al. [36] shows that the formation of dicarbon interstitial cluster is

kinetically favorable and isolated carbon cluster may exist inside in SiC substrate for the high carbon excess. Medium energy ion scattering (MEIS) measurements by Zhu X. et al. [37] and synchrotron X-ray photoelectron spectroscopy results from Watanabe H. et al. [38] reported a near perfect interface dominated by Si-O bonds. These contrastive results shows that more work is needed to identify the chemical compositions at the interface.

An inverse linear correlation between the width of a transition layer at the SiC/SiO_2 interface and the peak electron mobility of the MOSFET device has been reported by Biggerstaff et al.[35] and Taillon et at.[39]. The transition layer is not related to the oxidation growth conditions. In instead it is inherent to the SiC/SiO_2 interface. The oxidation growth parameters do not influence the presence of the transition layer, but they do affect the total width of the transition layer [35]. The thickness of the transition layers decreased nonlinearly with the annealing time, and reduced to ~5nm after 2 hours or even longer annealing time [39]. It has been suggested the existence of some kind of Si-C-O interlayer, or even Si-C-O-N-H layer, at the SiC/SiO_2 interface [23]. However, there has no strong experimental evidence to support that.

1.4.4. Si/SiO_2 interfaces and SiC/SiO_2 interface

It is well known that the (001) Si surface undergoes reconstruction by forming rows of dimers, eliminating half of the dangling bonds. Insertion of an O atom in a dimer leads to a stable configuration [40]. Because of the surface geometry of Si and the softness of the Si-O-Si angle, Si/SiO_2 interfaces have a high quality. The best-quality Si/SiO_2 interfaces are fabricated on Si (001) surface with almost perfectly abrupt in atomic scale. A Ge-implanted Si/SiO_2 interface was observed with atomic resolution Z-contrast imaging, and it showed an atomically sharp interface [41]. The density functional theory calculations showed that abrupt Si/SiO_2 interfaces were energetically favorable. Suboxide (Si^{1+} and Si^{3+}) bonds are energetically costly except for entropic considerations. Fig. 1-10 shows the superstructure of one layer of SiO_2 in Si viewing from [100] direction and [110] direction respectively. In the ideal interface all Si atoms are in the Si^{2+} oxidation state

[42]. The amorphous nature of the oxide and entropy effect lead to suboxide bonds (Si–Si bond on the SiO_2 side of the interface) and oxygen protrusions (Si–O–Si bond on the Si side of the interface) as the primary intrinsic deviations form an ideally abrupt interface, shown in Fig. 1-11. For all practical purposes there are no other intrinsic defects at Si/SiO_2 interface, and the oxygen protrusions causes strain in the last few atomic layers of crystalline Si [23, 43].

Oxygen has very low solubility in SiC and the oxidation of SiC is much slower than the oxidation of Si. The geometry favorable plane for oxidation is (0001) surface of hexagonal SiC. Oxygen atoms can enter the Si-Si dimers to form Si-O-Si bridges, however, all dangling bonds are then saturated and growth is terminated. Suboxide bonds, either isolated or in the form of steps, are inevitable at $SiC\text{-}SiO_2$ interfaces for further oxidation [42]. In addition, most of the SiC substrates have an off-axis cut angle. Steps caused by the off-axis cut introduced more complexities to understand the SiC oxidation process. One example is boron phosphide growth on the off-axis cut SiC substrate [44].

Atomic steps and terraces on a SiC wafer can be controlled by off-axis cut angle, which made SiC an excellent substrate for heteroepitaxial growth. Boron phosphide (BP) film is an example of heteroepitaxial epitaxy on SiC substrate. The basal plane of hexagonal SiC has a lattice parameter of 3.07Å, which is very similar to the interatomic distance along <110> directions in {111} planes of BP, 3.21Å. The lattice mismatch is only 4.5%. It was expected to be a good epitaxy system for a high quality BP single crystal film growth. Li [44] had a comprehensive study on this epitaxy system. The results showed that C-face of 4H-SiC with 4° off-axis cut along the $[11\bar{2}0]$ direction is the most suitable substrate for BP epitaxy growth. However, dislocations and lots of twin boundaries appeared in the BP film to release the strain caused by lattice mismatch between SiC and BP. The complex strain field at the BP/SiC interface may change the growing orientation of the BP film when the film thickness increased.

To fully understand the SiC/SiO_2 interface, it is necessary to learn the atomic structure of the vicinal surface.

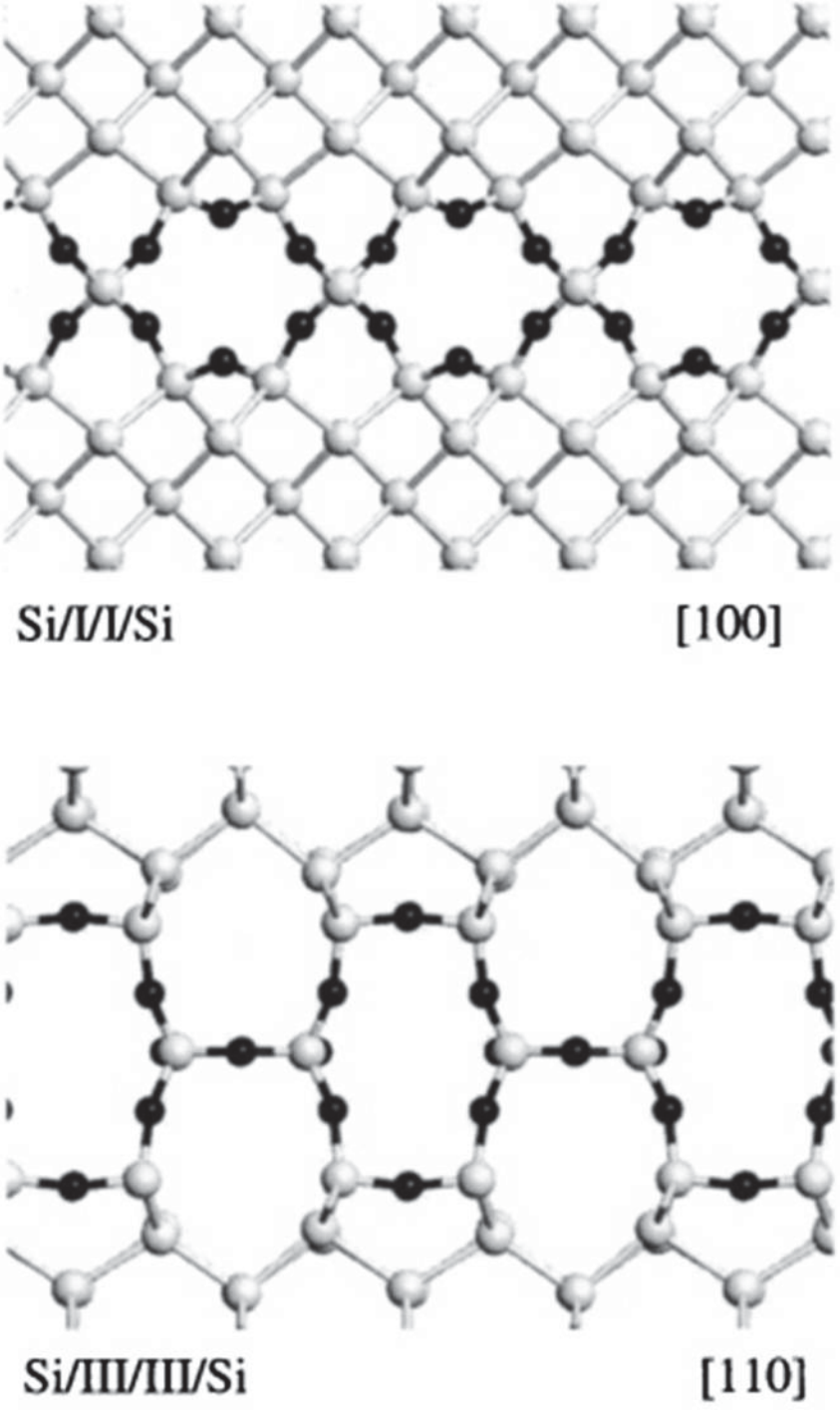

Fig. 1-10 Superstructure of abrupt Si/SiO_2 interface [42]. The grey balls are silicon atoms and the smaller black balls are oxygen atoms.

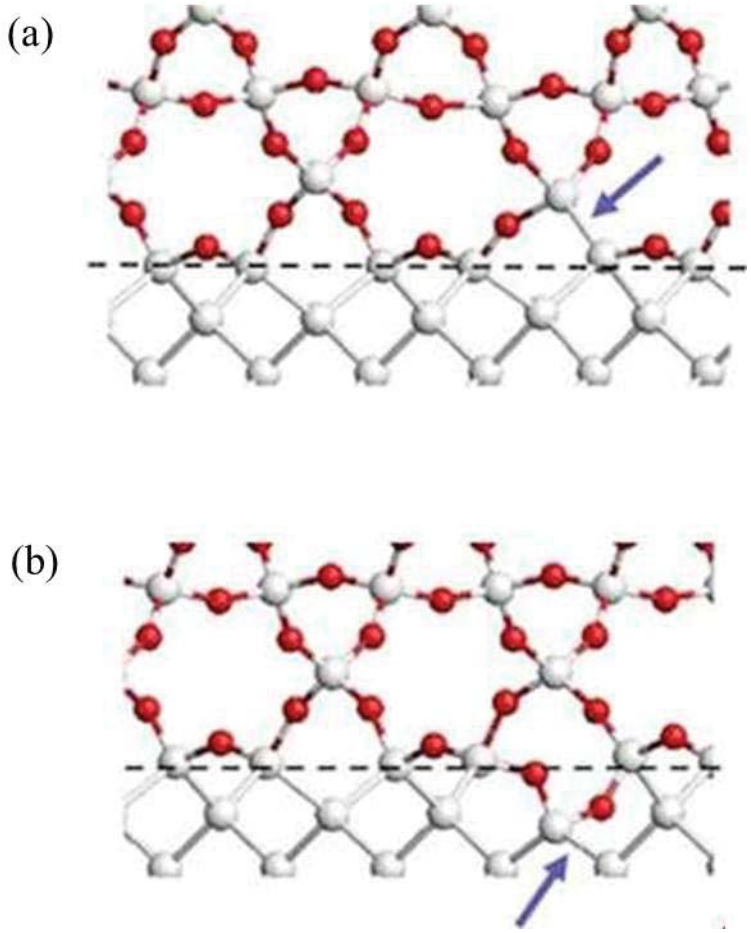

Fig. 1-11 (a) Suboxide and (b) oxygen protrusion at Si/SiO_2 interface, marked with arrows [45]. Si–Si bond on the SiO_2 side of the interface was named as suboxide and Si–O–Si bond on the Si side of the interface was named as oxygen protrusion.

1.5. Vicinal Surface

Steps of a vicinal surface are necessary for SiC homo-epitaxy [10, 46]. Presently, all SiC devices are implemented in homo-epitaxial films of the 4H- and 6H- SiC poly-types grown on commercial SiC wafers with surfaces polished 3° to 8° off the (0001) basal plane. This off-axis polish provides a high density of steps so that step-controlled epitaxy

can be used to grow homo-epilayers. The high step density and small terrace width ensures migration of mobile surface-adsorbed growth adatoms to step edges where they incorporate into the crystal [47].

Vicinal surfaces are obtained by cutting a single crystal with a small deviation angle with respect to the close-packed plane. Usually reconstruction will create a surface characterized with wide terraces separated by monoatomic steps. In some cases the steps may be 2 atomic layers high. In extreme cases, these steps may become of comparable size to the terraces and the surface forms relatively large facets (areas of low index planes).

The terrace-step-kink (TSK) model [48], developed by Burton, Cabrera and Frank in the early 1950s, elegantly describes the atomic-scale morphology of the vicinal surface, as shown in Fig. 1-12. The surface consists of terraces separated by steps; a kink is a step on a step. Atoms travelling over the vicinal surface will experience an energy barrier, known as Ehrlich–Schwoebel (ES) barrier, since the coordination number of the atom changes from a terrace to the edge or from a step to the kink. The inset is a scanning tunneling microscope image that shows the surface of a thin film of silicon (100 nm × 80 nm). Terraces separated by single-atom-high steps with many kinks can be seen, stepping down across the image from upper left to lower right. The white spots are atomic vacancies in the terraces [49].

The regular arrangements of atomic steps on a vicinal surface have the possibility to functionalize these surfaces for technical applications. Vicinal surfaces are currently attracting a lot of focus from various fields, such as step dynamics of vicinal surface, step-enhanced chemical reactions, epitaxy of film growth on vicinal surface, atomic wires growth, and so on. Electronic and chemical properties of the nano-objects on the vicinal surface can be tuned in a wide range by the coupling their nanostructures [50].

In a summary, SiC based MOSFETs are highly desirable for power electronics. However the real structure and chemistry of the interface are unknown. And the mechanisms to affect the MOSFET channel mobility are under debate. The structure of the SiC/SiO_2

interface at atomic level will likely be the final solution to all the problems concerning the device fabrication and applications.

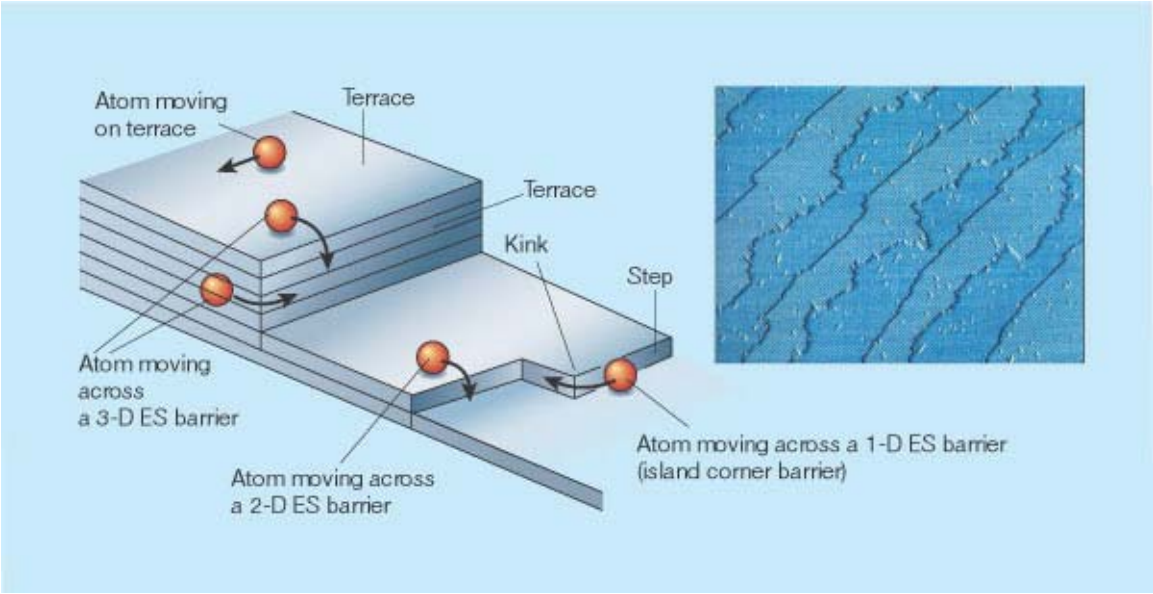

Fig. 1-12. Terrace-step-kink model of a vicinal surface and a scanning tunneling microscope image of terraces on a silicon thin film [49]

Chapter 2. RESEARCH METHODOLOGY

In this research crystal structure of the SiC/SiO_2 vicinal interface was carefully studied with atomic resolution TEM, scanning transmission electron microscopy (STEM) and simultaneous electron energy-loss spectrometry (EELS). Techniques including high-resolution transmission electron microscopy (HRTEM) imaging, Z-contrast imaging, EELS, and convergent beam electron diffraction (CBED) were used in the research. The measurements were performed on energy filtered (Zeiss) and aberration corrected (Nion) instruments.

2.1. Z-contrast Imaging

Z-contrast images are also known as high-angle annular dark field (HAADF) images. The contrast of Z-contrast images is a mass-thickness contrast arising from incoherent elastic scattering (Rutherford scattering) of electrons. The cross section for Rutherford scatter is a strong function of the atomic number Z, and therefore, these images contain both structural and chemical information. In addition, these images can be interpreted much more straightforwardly than conventional HRTEM images. Another important advantage of Z-contrast imaging is that chemical analyses can simultaneously be achieved with integrated electron energy-loss spectrometer or X-ray energy-dispersive spectrometer.

Z-contrast images are formed by scanning a highly convergent electron beam (convergence semi-angle α is 15-35 mrad) across the surface of a thin sample and collecting those transmitted electrons which are scattered to high angles onto a high-angle annular dark field detector. At high angles (> 90 mrad), where Bragg scattering is usually negligible, one can pick up low-intensity, incoherently scattered beams [51]. The intensity of these beams depends on atomic number Z only. Based on this, in the approximation of large collection angles, each atom can be considered an independent scattering source with a scattering cross-section of approximately Z^2 [52, 53]. The spatial

resolution is limited only by the size of the probe in the microscope, which is as small as 1 Å for a fifth order aberration corrected STEM at 100 kV [54]. In crystalline materials along a zone-axis orientation, the atomic spacing is greater than the probe size, and the columns are therefore illuminated sequentially as the probe is scanned over the specimen and an atomic resolution compositional map is subsequently generated.

2.2. Atomic Resolution Electron Energy Loss Spectroscopy

EELS has the tremendous advantage that the energy-loss electrons are predominantly forward scattered so one can easily collect most of the signal. Compared with X-ray energy-dispersive spectrometry (XEDS) this technique is inherently far more efficient. At the same time EELS has a higher energy resolution and sensitivity for light elements[55].

An energy-loss Spectrum is acquired by collecting the low-angle scattered electrons, so this technique can be combined with the Z-contrast imaging. This means that the Z-contrast image can be used to position the electron probe over a specific structural feature for the acquisition of a spectrum. This simultaneous analysis allows for direct chemical analysis of extremely localized structures. Fig. 2-1 is a schematic diagram of STEM operation with simultaneous EELS acquisition[56]. While the electron probe scans across the sample, electrons scattered to high angles are detected by a HAADF detector, and (in principle) all of electrons passing through the central hole of the HAADF detector enters the prism to form an EELS spectrum. A typical EELS spectrum was shown in Fig. 2-2 [57]. The intensity of valence-loss peaks and core-loss edges were amplified to fit the intensity scale of the zero-loss peak. From the low-loss structures of an EELS spectrum, band gap information, plasma response and thickness information of the material can be extracted. Chemical information such as bonding state and concentration of a certain element in the material can be extracted from the core-loss spectrum. The basic physical principle behind EELS relates to the interaction of fast electrons with the sample to cause either collective excitations of electrons in the conduction band, or discrete transitions between atomic energy levels. The ability to observe discrete atomic transitions allows

compositional analysis to be performed by EELS due to the face that the transitions occur at characteristic energy losses for a given element. Additionally, the transitions to unoccupied states above the Fermi level allows the degree of hybridization between atomic orbitals to be determined, that is, information on local electronic bonding structure changes can be established.

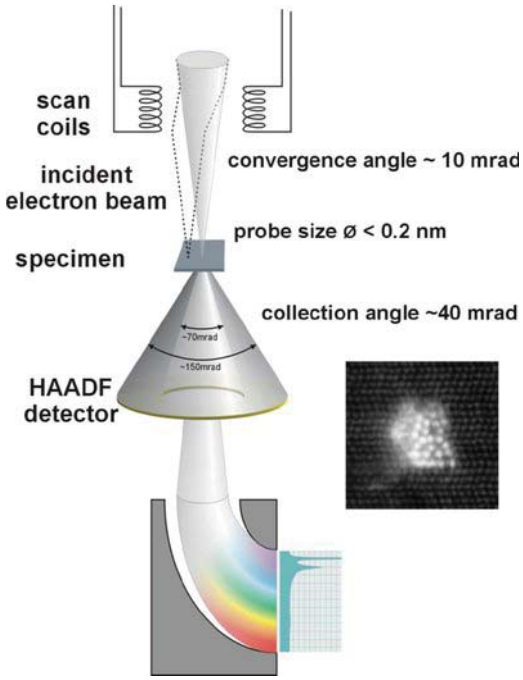

Fig. 2-1 A schematic diagram of STEM operation with simultaneous EELS acquisition [56]. While the probe scans across the sample, electrons scattered to high angles are detected by a HAADF detector, and (in principle) all of the electrons passing through the central hole of the HAADF detector enters the prism to form an EELS spectrum.

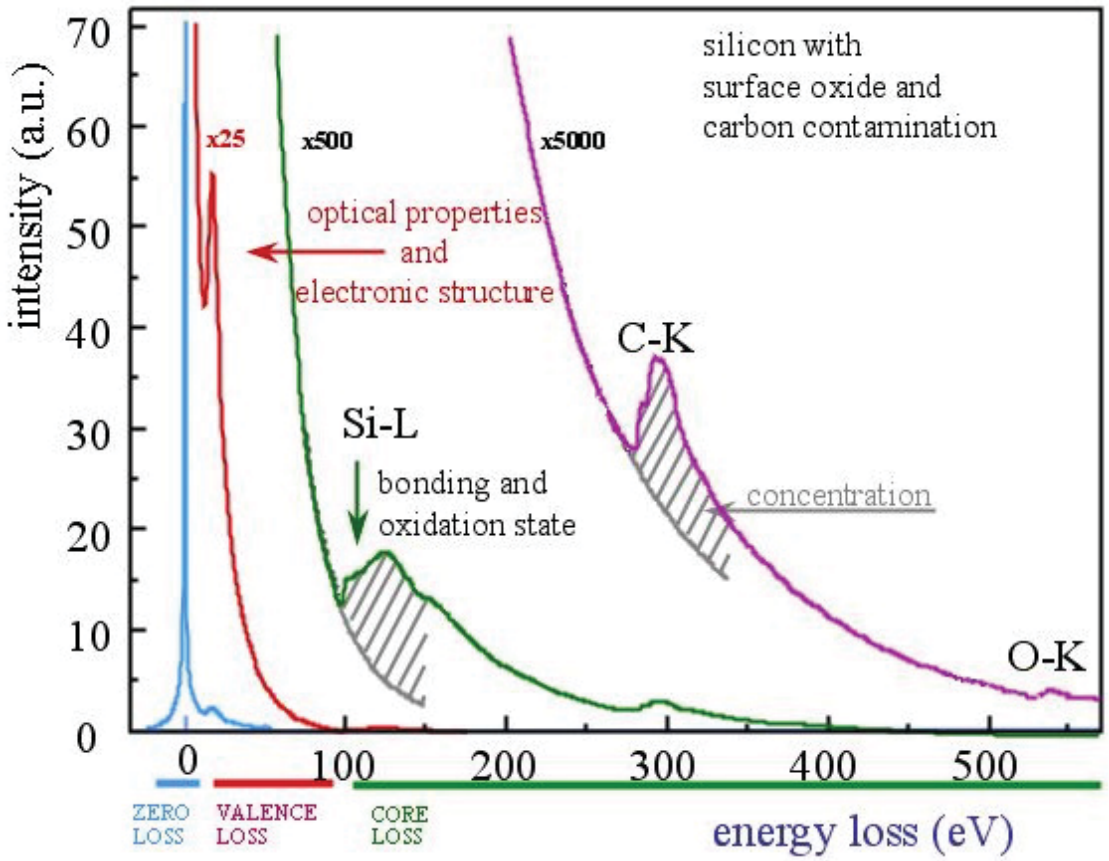

Fig. 2-2 A schematic diagram of a typical EELS spectrum [57]

2.3. Convergent Beam Electron Diffraction

Convergent beam electron diffraction (CBED) is a very powerful method to determine the crystal structure of a material. It was originally developed by Kossel and Möllenstedt in 1939, well before LePoole developed selected area diffraction (SAD) technique. Compared with the classic and well-known technique, selected area diffraction, CBED has several advantages. In SAD the electron beam which is incident into the specimen is parallel, with a typical beam diameter of 1-10 μm. The area involved in the SAD is determined by the size of the SAD aperture. Traditionally the diameter of the smallest area one can select by a SAD aperture is about 0.5 μm with an error of similar dimension. The resulting transmitted information is a spot pattern. The electron beam in CBED is focused to a converged point, typically from sub-nanometer to a few nanometers in diameter. The resulting transmitted diffraction pattern is in the form of discs that may or may not overlap. In spite of the patterns of a CBED forming form a much smaller region, they contain a wealth of quantitative data. Same as the conventional SAD patterns, CBED patterns give the crystallographic data of a crystalline sample including the unit cell and associated lattice parameters, and full 3D crystal symmetry. In addition, precise specimen thickness, lattice-strain, enantiomorphism and polarity can be measured by using CBED patterns. Characterization of line and planar defects can be done with the CBED pattern. Valence-electron distribution, structure factors, and chemical bonding information are also included in CBED patterns [51].

Fig. 2-3(a) is a (000) CBED disk of 4H-SiC viewing along $[1\bar{1}00]$ direction. The Kikuchi lines in CBED disk indicate the crystallographic directions of a crystal, which can be used as a map when tilt a sample under the electron beam. With the help of the Kikuchi 'map' one can easily find the right zone axis for imaging. In Fig. 2-3(b) the CBED disks ware taken at two-beam condition. In each disk the bright and dark stripes are thickness fringes of the 4H-SiC sample. The thickness of a thin sample can be measured locally and precisely.

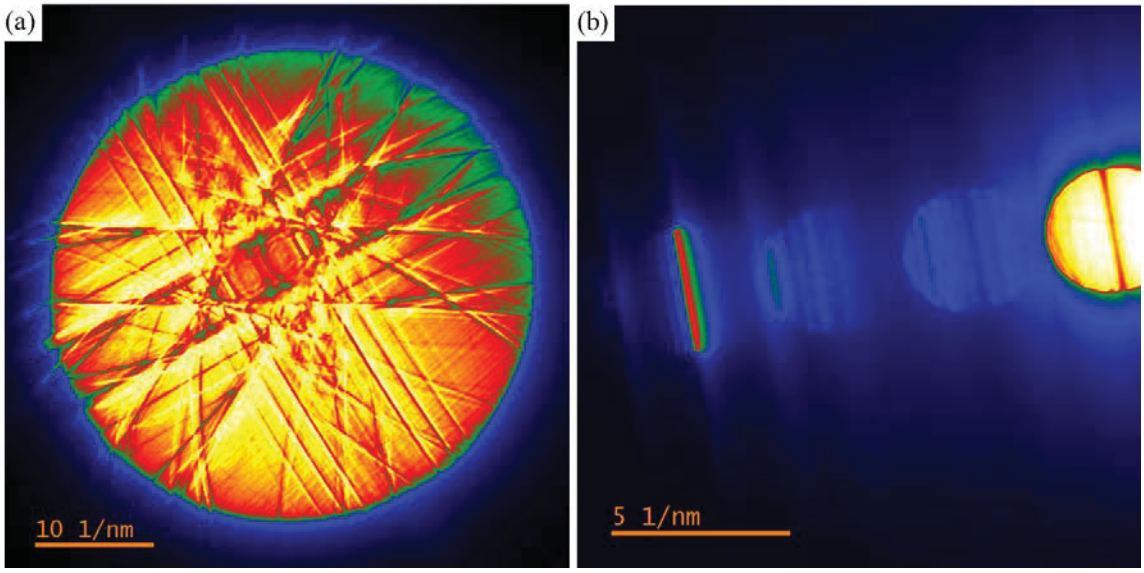

Fig. 2-3. (a) (000) CBED disk of 4H-SiC taken with [1$\bar{1}$00] zone axis. (b) Thickness fringes in 4H-SiC CBED discs.

2.4. TEM Sample preparation method

When conducting TEM, optimum analytical results are achieved by preparing the highest quality specimens. With proper specimen preparation instrumentation and techniques, TEM performance and the corresponding analysis will be greatly enhanced. TEM samples must be thinned to electron transparency. The requirements for samples which undergo quantitative EELS analysis are more stringent than conventional TEM, STEM, or HRTEM because the samples should ideally be between 0.3~0.7 times the mean free path of an electron in the sample. Two methods are usually used for preparing a cross sectional views of ceramic samples.

2.4.1. Conventional Sandwich/Ion Milling Sample Preparation

This sandwich/ion mill method involves creating a sandwich of material which is then mechanically thinned, dimpled, and then ion milled to form an electron transparent region. This method has been used for a long time and was first described by Abrahams et al in 1974 [58].

SiC is a particularly difficult sample to prepare using conventional sample preparation methods because the high bond strength and high hardness of SiC results in ion milling time which is much longer than other materials of the same thickness. Additionally, the SiO_2 film, which has notably lower bond strength than the SiC substrate, can be destroyed during ion milling if it is not properly shielded or if the milling is started when the sample is still too thick. In order to minimize these problems, the ion milling should be performed when the sample is less than 10 μm [59]. The multiprep system manufactured by Allied company is a sophisticated equipment for the SiC/SiO_2 cross section sample polishing and thinning. On this stage a sandwich foil can be polished down to 10 μm without dimpling.

2.4.2. Focused Ion Beam Milling Sample Preparation

Focused ion beam (FIB) is also widely utilized today for TEM sample preparation. The basic operational principle of FIB milling is sputtering atoms from the target material. A gallium liquid metal ion source (LMIS) was selected as the milling source. Ga has a relatively heavy nuclear and low melting point of 29.8 °C. The momentum transfer at a given acceleration voltage, usually 30 kV, is high efficiency. The LMIS is composed of a small Ga reservoir connected to a tungsten needle. The solid Ga is heated to its melting point and the liquid Ga flows to the tip of the needle by surface tension to form a point source of about 2-5 nm in diameter. Ga^+ ions are extracted from the point source by a strong electric field (10^8 V/cm) applied to the end of the tungsten tip. The Ga ions are then accelerated with the 30 kV high tension to form a continuous ion beam [60]. The

focused beam of gallium ions is used to thin an area of interest on the specimen to electron transparency. The sample can then be lifted out using a needle and loaded onto a lift out grid. A typical process is shown in Fig. 2-4. Fig. 2-4(a) is one type of standard TEM lift out grids of 3 mm in diameter. It has 3 posts for TEM lamellas attaching. The tip of the center post was magnified and shown in Fig. 2-4(d), where the lamella will be mounted finally. Usually a platinum layer was deposited first on the point of interest to protect the surface from iron beam damaging. Then the TEM lamella was milled by FIB on the protected spot, shown in Fig. 2-4(b). The FIB milled lamella was welded on a tungsten probe and then cut away from the substrate for lift out, as shown in Fig. 2-4(c). The lamella was transferred with the probe to the post of the TEM lift out grid, and was welded on the post, as shown in Fig. 2-4 (d) and (e). Finally the lamella was thinned down to electron transparency. The final state of a FIB milled TEM lamella is shown in Fig. 2-4 (f), where two thin windows were milled on, and the thicker frames of the window are helpful to support the thin windows.

FIB milling sample preparation has several advantages as opposed to conventional sample preparation. First, TEM samples can be milled from a point of interest on the substrate. The microstructure of the specific point can be directly studied. Conventional techniques used to make TEM samples, such as chemical polishing or ion-sputtering milling, cannot provide reliable opportunity to make TEM samples from a specific point of the substrate. Second, FIB allows for large electron transparent regions which are completely flat with no bending (typically 5-20 square microns). Third, FIB sample preparation consumes only a small volume of material, leaving most of the material essentially unaffected by the sampling process. What is more, FIB milling is time efficient compared with the conventional sample preparation methods. Because of these advantages, FIB technique spreads widely and is especially preferred for preparing TEM samples from semiconductor devices.

The disadvantage of FIB technique is the beam damage during the thinning. The high energy ion beam may cause an amorphization on the surface of a crystalline TEM sample. For example, a typical 30 keV Ga^+ ion beam can cause a damage depth as thick as 30 nm on Si [61]. The use of low energy FIB (5 or 10 kV) for the final stage of foil fabrication

or cleaning with conventional broad argon ion milling after FIB fabrication can extremely reduce the beam damage.

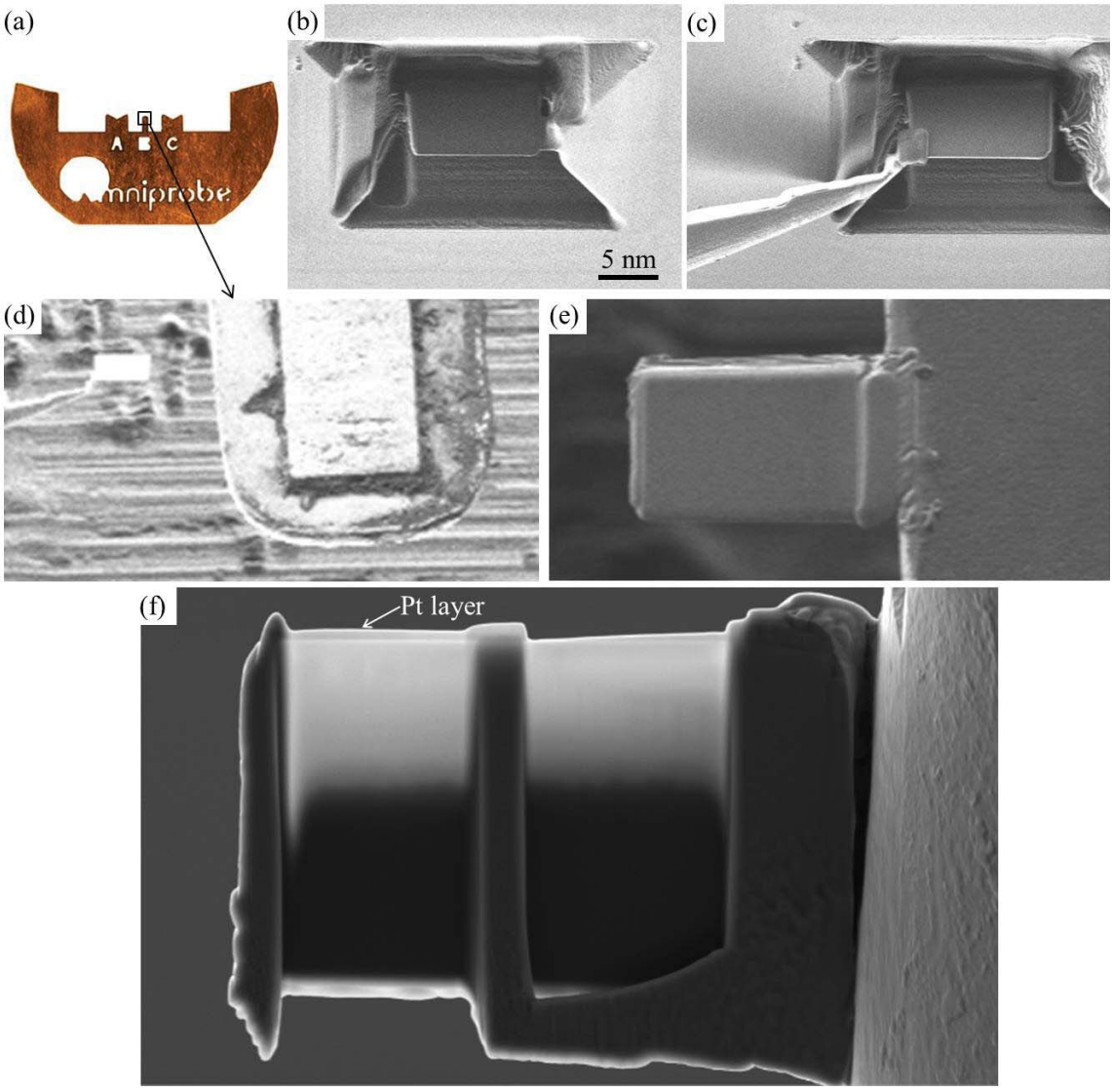

Fig. 2-4 Sample preparing procedures by FIB.

2.5. Samples

4H-SiC wafers were used as the MOSFET substrates. Two substrates of the MOSFETs had an 8° off-axis cut along [$11\bar{2}0$] direction at Si face, and the third one had an on-axis cut at Si face. A ~100 nm SiO_2 layer in total was grown on each substrate. Molybdenum was deposited on the SiO_2 layer to form a metal-oxide-semiconductor (MOS) capacitor. The oxidation details of the MOS capacitors were described as the following:

MOS capacitor 1 (8° off-axis cut substrate): First, thin NO oxidation was done for 2 minutes at 1175 °C. Then plasma-enhanced chemical vapor deposition (PECVD) was done at 400 °C for SiO_2 layer grown. Finally plasma enhanced nitride (PEN) passivation was done for 4 hours at 1160 °C, with the pressure 2.8 torr.

MOS capacitor 2 (8° off-axis cut substrate): First, NO oxidation was done for 2 hours at 1175 °C. Then phosphosilicate glass (PSG) passivation was done for 4 hours at 1000 °C. Finally, PECVD was done at 400 °C for SiO_2 layer grown.

MOS capacitor 3 (on-axis cut substrate): A standard thermal oxidation was done for ten hours followed by the NO passivation of 2 hours at 1175 °C.

According to the oxidation process, All the oxidation layers were well passivated, which gave a steady transition region, and therefore, prevented the effect of anneal time on the transition layer width, which has been studied previously [35, 39]. Cross-section TEM samples were prepared from the MOS capacitors by focused ion beam (FIB) milling with a Zeiss Auriga SEM/FIB crossbeam workstation. A Ga ion beam of 30 keV was used for coarse milling and a 10 keV 50 pA beam was used for final polishing. Lamellas ware thinned down to 50 nm-100 nm. TEM samples were examined with Nion UltraSTEM at 100 keV and Zeiss Libra200 MC TEM at 200 keV.

2.6. Electron Microscopes

Zeiss Auriga SEM/FIB crossbeam workstation combines the 3D imaging and analysis performance of the GEMINI e-Beam column with the ability of a FIB for material processing and sample preparation on a nanoscopic scale. TEM samples can be precisely milled from a specific area of interest on a bulk material or an electronic device. In addition to the FIB gun, a gas injection system was also integrated in the workstation. Micro to nano scale depositions can be carried out under the crossbeam workstation with high precision [62, 63].

The Nion UltraSTEM is a dedicated STEM with a high-performance 3rd generation C_3/C_5 aberration corrector. The spherical abreaction can be corrected up to the 5^{th} order so the STEM has a sub-angstrom spatial resolution. At the same time the Nion UltraSTEM provides an atom-size electron probe with high intensity for chemical analysis (100 pm electron probe with 30 pA current at 100 kV) [54].

Zeiss Libra200 MC is a 200 kV energy filter TEM. The electron beam emitting from the high efficiency field emission gun is filtered with a Ω-type monochromator (MC), which produces a fine electron probe (200 pm at 200 kV) for atomic resolution imaging and chemical analysis. The energy resolution of EELS spectrum acquired by Libra 200 MC is super high. Fig 2-4 showed a zero-loss spectrum acquired by Libra 200 MC. The zero-loss peak had a 0.3 eV resolution and a high intensity. The Köhler illumination system of Libra 200 MC incorporates an in-column energy filter of the corrected Ω-type. This Ω-type energy filter can be used as an imaging energy spectrometer. With the integration of the imaging energy spectrometer in the imaging beam path of the TEM, information contained in inelastically scattered electrons can be fully utilized, and spectrum imaging becomes 2nd order aberration corrected and 3rd order optimized. The quality of imaging and diffraction are considerably increased [63, 64].

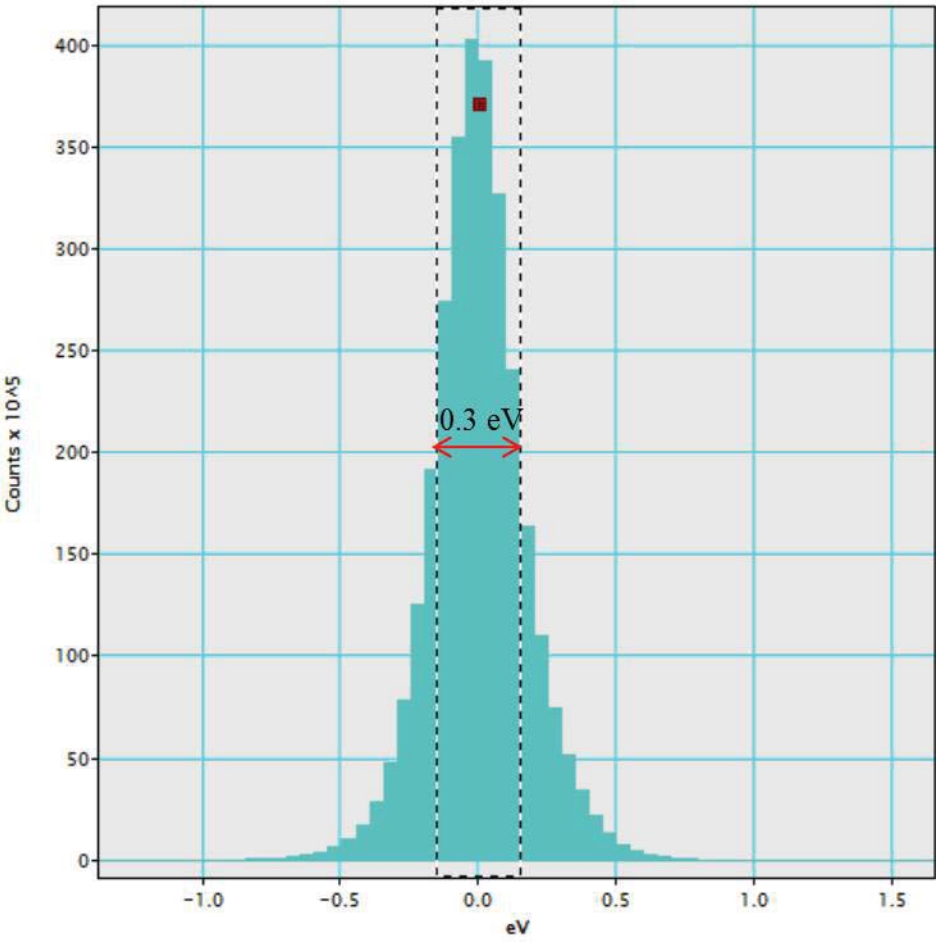

Fig. 2-5 High energy resolution EELS spectrum with high intensity taken with Libra 200 MC TEM.

Chapter 3. THICKNESS MEASUREMENT

3.1. Thickness estimation form EELS

It is often necessary to know the local thickness of a TEM specimen, to convert the areal density provided by EELS or EDX analysis into elemental concentration. Here CBED pattern and low-loss EELS spectrum were used to determine the thickness of a sample.

Log-ratio method is the most widely used method to estimate the local thickness of a TEM lamella. It is returned in relative units of the inelastic mean free path (IMFP) of electrons in the sample. If the IMFP are known, the absolute thickness can be calculated.

The most common procedure of the log-ratio method is to record a low-loss spectrum and compare the area I_0 under the zero-loss peak with the total area I_t under the whole spectrum [65]. According to Poisson statistics the thickness t is given by

$$t/\lambda = \ln\left(I_t/I_0\right)$$

Eq. 3-1

Thickness returned by these routines is influenced by a number of experimental parameters. Residual detector background can be a large source of error in a thickness calculation, particularly for samples less than one IMFP thick. Hence ensure spectra are acquired with dark signal and gain correction selected, ensuring both pixel-to-pixel variations and dark current are corrected. The collection angle must be large enough so that the plural scattering obeys Poisson statistics. A collection semi-angle β of 5-10 mrad suffices to ensure Poisson statistics to within 10% accuracy for typical beam and edge energies. In this case, the effect of the finite acceptance aperture can be subsumed as collection-angle dependence of the IMFP $\lambda(\beta)$. The zero-loss peak of the low-loss spectrum must be modeled and extracted accurately, which is important to calculate I_t and I_0.

To calculate the intensity of I_t and I_0 from a low-loss spectrum, zero-loss peak is need to be extracted first. Because the tails of the zero-loss peak can contain a substantial number of counts relative to the loss part of the spectrum, it is important to take account of them when performing the zero-loss peak separation. Several models of zero-loss peak are adopted, such as reflected tail, fitted logarithmic tail, fit pre-measured Zero-loss, Maxwell-Boltzmann tail, Maxwell-Boltzmann & Lorentzian tail, and so on [66]. Some of them are briefly described here.

In the reflected tail model, zero-loss peak is assumed to be relatively symmetric and a reflection of the left-side tail is used to model the tail on the energy-loss side. The "2 Gaussian" model uses least-squares fitting to fit two Gaussian functions to the zero-loss peak. It is reasonably robust, but is not well suited to zero-loss peaks with long tails arising from high detector point-spread function. To ensure a sensible fit, one of the Gaussian models has its center position constrained to the zero-loss center, whilst the second has its width constrained to that of the zero-loss peak. To complement the short tails of the "2 Gaussian" model, Gaussian & Lorentzian fit is introduced. This model uses least-squares fitting to fit the sum of a single Gaussian and a Lorentzian function to the zero-loss peak. The Lorentzian function has long tails and hence this model is suited to spectra recorded on detectors with high point-spread. Gaussian & Lorenzian^2 model has a tail in between. This model uses least-squares fitting to fit the sum of a single Gaussian and a Lorentzian function squared to the zero-loss peak. The squared Lorentzian has extended tails to suit detectors of high point-spread, but less so than the Gaussian & Lorentzian model. The fitting procedure is identical to that described above for the Gaussian & Lorentzian model. In Maxwell-Boltzmann model, zero-loss peak is fitted with a Maxwell-Boltzmann distribution of the form $I(E) = Aexp(-E/kT)$, where I is intensity, E is energy-loss, A is a constant, and T the emitter temperature (in Kelvin). The model produces an asymmetric distribution and is suitable for spectra acquired using a cold-FEG source. By default, the start value of T is 800 K.

Fig. 3-1 is a low-loss spectrum acquired with an e-beam of 100 keV at the SiC side of the SiC/SiO_2 cross section TEM sample. Zero-peak was separated with the Gaussian & Lorentzian model. The zero-loss peak is plotted in red and inelastic component of the

low-loss spectrum in blue. Then the zero-Loss peak integral I_0 = 196832960.0 and the inelastic integral I_{in} = 215356064.0, calculated by Digital Micrograph (DM). Then the Relative sample thickness $t/\lambda = ln((I_0 + I_{in}) / I_0)$ = 0.74.

The same procedure was also applied to a low-loss spectrum acquired at 200 keV on the same sample. Relative sample thickness is 0.45 times of electron IMFP in SiC at 200 keV. The results are shown in Fig. 3-2.

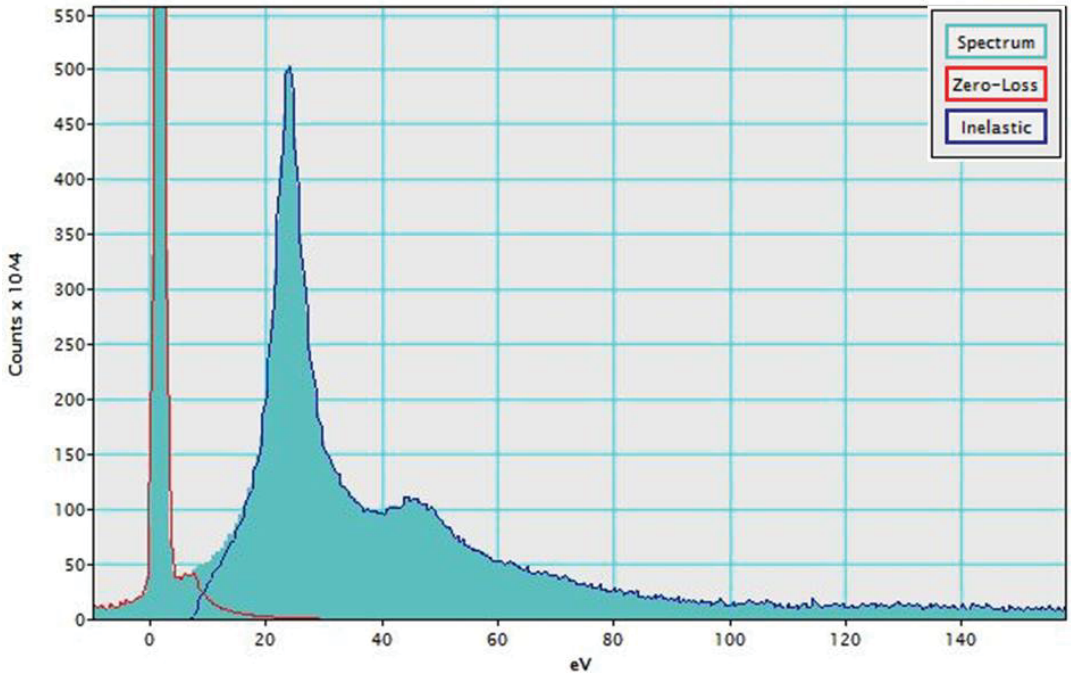

Fig. 3-1 Thickness computation from a low-loss spectrum acquired at 100 keV on SiC. Relative sample thickness = 0.74 IMFP at 100 keV

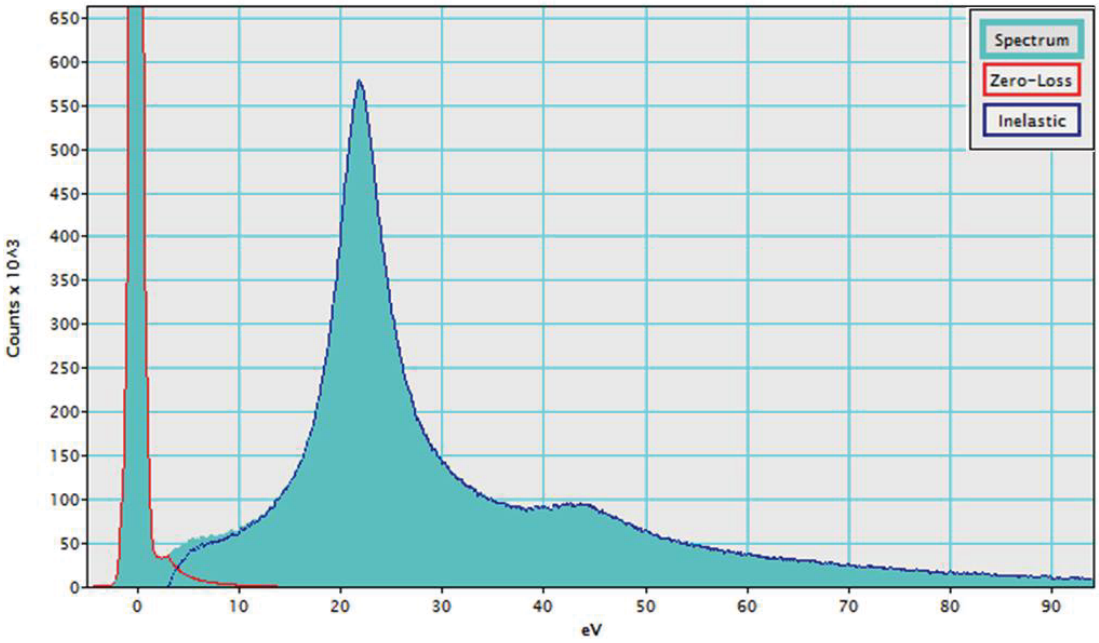

Fig. 3-2 Thickness computation from a low-loss spectrum acquired at 100 keV on SiC. Zero-Loss peak (red) integral = 320745440.0 and inelastic (blue) integral = 172935104.0. Relative sample thickness = 0.45 IMFP at 200 keV.

3.1.1. Electron IMFP in SiC

The IMFP is a very important value for the thickness estimation of a TEM sample in EELS analysis. Based on the dipole formula, the IMFP of a material with known composition could be calculated.

The most frequently used parameters for SETM in this research are the accelerating voltage of the electron beam E_0 = 100 keV or 200 keV and the collection angle β = 10 mrad. The following calculations will base on these parameters.

Dipole Formula Calculation ([65], Egerton, p296)

Realistic values of mean free path are possible by using scattering theory to parameterize λ in terms of the collection semi-angle β, the incident energy E_0, and a parameter that depends on the chemical composition of the specimen. Assuming the semi-collection angle $\beta << (E_m/E_0)^{1/2}$, implying $\beta < 15$ mrad at E_0 = 100 keV, parameterized the inelastic mean free path on the basis of a dipole formula (Malis, 1988):

$$\lambda \approx \frac{106F\left(\frac{E_0}{E_m}\right)}{\ln\left(2\beta\frac{E_0}{E_m}\right)}$$

Eq. 3-2

In this equation, λ is in nm, β in mrad, E_0 in keV, and E_m (mean energy loss) in eV; F is a relativistic factor defined by

$$F = \frac{T}{E_0} = \frac{m_0 v^2}{2E_0} = \frac{1+\frac{E_0}{1022}\ keV}{\left(1+\frac{E_0}{511}\ keV\right)^2}$$

Eq. 3-3

so F = 0.768 for E_0 = 100 keV, and F = 0.618 for E_0 = 200 keV.

For an element whose atomic number Z is known,

$$E_m \approx 7.6\, Z^{0.36}$$

Eq. 3-4

In the case of a compound, the Lenz model suggests an effective atomic number for use in Eq. 3-4:

$$Z_{eff} \approx \frac{\sum_i f_i Z_i^{1.3}}{\sum_i f_i Z_i^{0.3}}$$

Eq. 3-5

where f_i is the atomic fraction of each element of atomic number Z_i.

So, for SiC

$$Z_{eff}^{SiC} = \frac{0.5(14^{1.3} + 6^{1.3})}{0.5(14^{0.3} + 6^{0.3})} = 10.50$$

$$E_m = 7.6 \times 10.50^{0.36} = 17.72\ eV$$

At an incidence electron beam of 100 keV and collection angle β = 10 mrad,

$$\lambda = \frac{106 \times 0.768(\frac{100}{17.72})}{ln\,(2 \times 10 \times \frac{100}{17.72})} = 97.20\ nm$$

At an incidence electron beam of 200 keV

$$\lambda = \frac{106 \times 0.618(\frac{200}{17.72})}{ln\,(2 \times 10 \times \frac{200}{17.72})} = 136.43\ nm$$

The Eq. 3-4 is roughly consistent with the Lenz atomic model of inelastic scattering, but makes no allowance for differences in crystal structure or electron density; it would predict the same mean free path for graphite, diamond, and amorphous carbon, for example. And note that Lenz model yield an effective Z that may be too high, so that λ is underestimated.

EPES Measurement

By the elastic peak electron spectroscopy (EPES), IMFP could be measured experimentally [67]. The measured IMFP values λ can be fitted with a simple Bethe equation:

$$\lambda = \frac{E}{E_p^2 \beta ln\,(\gamma E)}$$

where E is the electron energy (in eV), Ep is the free-electron plasmon energy (in eV). Values of the parameters $Ep^2\beta$ and γ were obtained using the nonlinear least-squares (NLLS) algorithm from fits of the EPES IMFP measurements for polycrystalline SiC. $Ep^2\beta$ and γ are 12.09 $eV\text{Å}^{-1}$ and 0.0493 eV^{-1}, respectively.

At an incidence electron beam of 100 keV

$$\lambda = \frac{100000}{12.09 \times \ln\,(0.0493 \times 100000)}\text{Å} = 97.27 \text{ nm}$$

At an incidence electron beam of 200 keV

$$\lambda = \frac{200000}{12.09 \times \ln\,(0.0493 \times 200000)}\text{Å} = 179.88 \text{ nm}$$

The calculated value of electron IMFP of SiC agreed very well with the IMFP experiment at 100 keV, and underestimated at 200 keV.

Now plug the experiment values of IMFP and the relative thickness of the sample in to equation Eq. 3-1:

at 100 keV,

$$t = 97.27 \text{ nm} \times 0.74 = 72.0 \text{ nm}$$

at 200 keV

$$t = 179.88 \text{ nm} \times 0.45 = 80.9 \text{ nm}$$

The larger value at 200 keV is caused through a slightly thicker sample location where the low-loss EELS spectrum was collected. This change of location was necessary to protect the interface from beam damage.

3.2. Thickness measurement from CBED pattern

When recording a zone-axis pattern under conditions where $2\alpha < 2\theta_B$ (α is the convergence semi-angle and θ_B is the Bragg angle), the 000 disk of the CBED pattern usually contains concentric diffuse fringes known as Kossel-Möllenstedt (K-M) fringes. These fringes contain thickness information. The number of fringes increases by one every time the thickness increases by one extinction distance, $\xi_{\boldsymbol{g}}$. The sample thickness can be measured precisely at the point one is doing diffraction and microanalysis. For crystalline materials, the method is one of the best and the most accurate method of thickness determination. In practice, to simplify the interpretation, samples are tilted to two-beam conditions with only one strongly excited *hkl* reflection, other than measure it under zone-axis conditions.

When the thickness fringes in the CBED pattern is recorded at two-beam condition, it is easy to measure the distances between the middle of the central bright fringe and each of the dark fringes with an accuracy of about ±0.1 mm. The central bright fringe is at the exact Bragg condition where **s** = 0. The fringe spacings correspond to angles $\Delta\theta_i$ as shown schematically in Fig. 3-3(a), and from these spacings one can obtain a deviation s_i for the i^{th} fringe (where i is an integer) from the equation

$$s_i = \lambda_0 \frac{\Delta\theta_i}{2\theta_B d^2}$$

Eq. 3-6

where λ_0 is the wavelength of electrons, θ_B is the Bragg angle for the diffracting *hkl* plane, d is the *hkl* interplanar spacing, and here I will use the magnitude of s, ignoring its sign. The angle $2\theta_B$ in the CBED pattern is just the separation of the 000 and *hkl* disks.

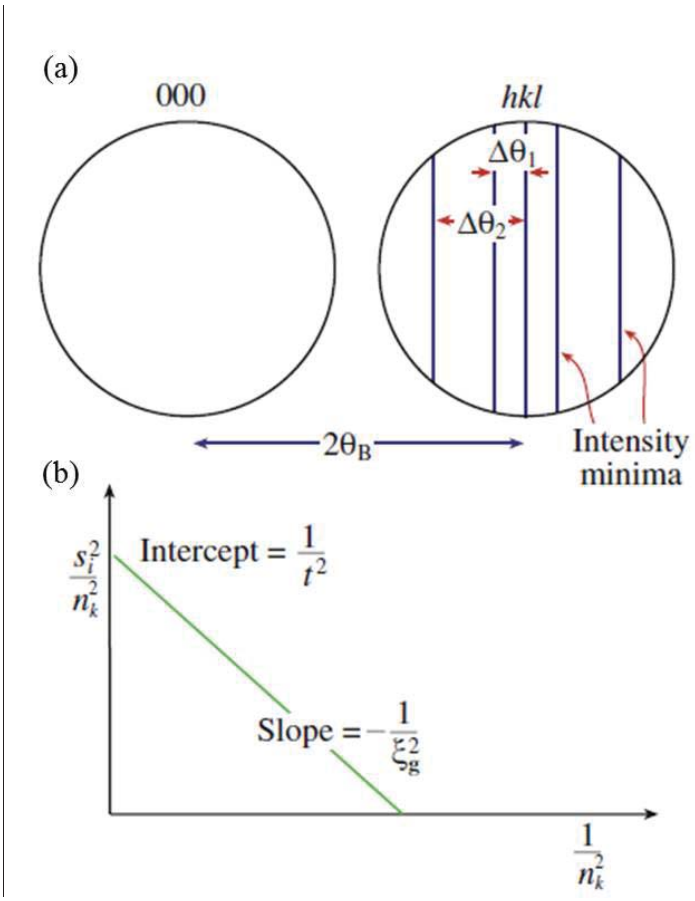

Fig. 3-3 (a) The measurements necessary to extract thickness (t) from K-M fringes. From n_i measured spacings of $\Delta\theta_i$, determine the deviation parameters s_i, then (b) plot $(s_i/n_k)^2$ against $(1/n_k)^2$. If the plot is a straight line, extrapolate to the ordinate to find t^{-2} and hence t [51].

If the extinction distance ξ_g is known, then the foil thickness t can be determine by

$$\frac{s_i^2}{n_k^2} + \frac{1}{\xi_g^2 n_k^2} = \frac{1}{t^2}$$

Eq. 3-7

where n_k is an integer (k is an integer identical to i or differing from i by a constant integer not related to λ_0). If ξ_g is unknown, then a graphical method can be used to plot the measurements for several fringes as follows.

1. Arbitrarily assign the integer n = 1 to the first fringe, which corresponds to an excitation error s_1.
2. Then assign n = 2 to the second fringe, s_2, etc.
3. Plot $(s_i/n_k)^2$ versus $(1/n_k)^2$. If the result is a straight line, the arbitrary assignment was good. That is, the relationship between i and k is given by $k = i + j$ where j is the largest integer < (t/ξ_g).
4. If the plot is a curve, then repeat the procedure by re-assigning n = 2 to the first fringe.
5. Continue to iterate until a straight line is found, as shown in Fig. 3-3(b).

From the straight-line plot, the intercept is $1/t^2$ and the slope is $-1/\xi_g^{-2}$ [51].

Sample thickness measurements were carried out on a FIB milled lamella. Fig. 3-4(a) is a HAADF image of a thin window on the lamella. On the left is SiO_2 and on the right is single crystalline SiC. The top is the frame of the thin window, which is thicker and therefore shows a brighter contrast compared with the lower part of the image. The bottom part is the thin SiC crystal. The sample became thinner gradually from top to bottom, and several measuring points were set along the thickness gradient, which were labeled b, c, d, e, and f respectively on the image. The sample tilt is ~7° off the $[1\bar{1}00]$ zone axis of 4H-SiC to achieve a two-beam condition. Only the 004 beam is strongly diffracted. The corresponding thickness fringes were shown on the right of Fig. 3-4. In each of the CBED patterns the brightest disk is 000 disk and its right neighbor is 004 disk. From Fig. 3-4 (b)-(f) one can see that more fringes propagated on thicker area, which is more convenient to derivate the correlation between $(s_i/n_k)^2$ and $(1/n_k)^2$. Up to position e

and f the sample is thin and uniform, from where EELS spectra were usually acquired. So the thickness measurements on thin areas are more essential. However, on the thin area only one or two fringes showed up, and it is impossible to calculate the thickness from the graphical method. Luckily the extinction distance ξ_g can be calculated with the graphical method at a thick area. Then the value can be substituted in to Eq. 3-7 to calculate the thickness *t*.

The measuring of $\Delta\theta_i$ is demonstrated in Fig. 3-5. Across the fringes in 000 and 004 disks in Fig. 3-5(a), one can draw a line profile, and therefrom the fringes showed as crests and troughs in the intensity profile, as shown in Fig. 3-5(b). Both the $2\theta_B$ and $\Delta\theta_i$ were measured with pixels so their ratios were dimensionless. In the CBED pattern and the corresponding intensity profile, the center of the 000 and 004 disks are marked, from where $2\theta_B$ was read as 284 pixels wide.

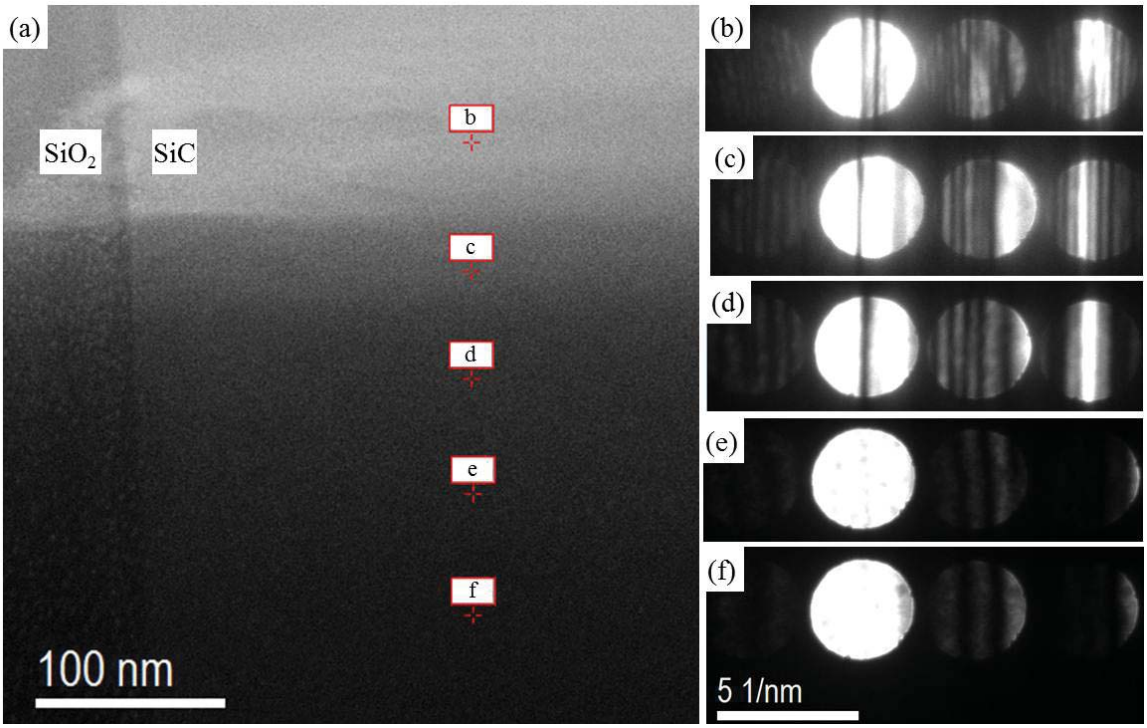

Fig. 3-4 Thickness fringes in the CBEDs acquired form SiC lamella

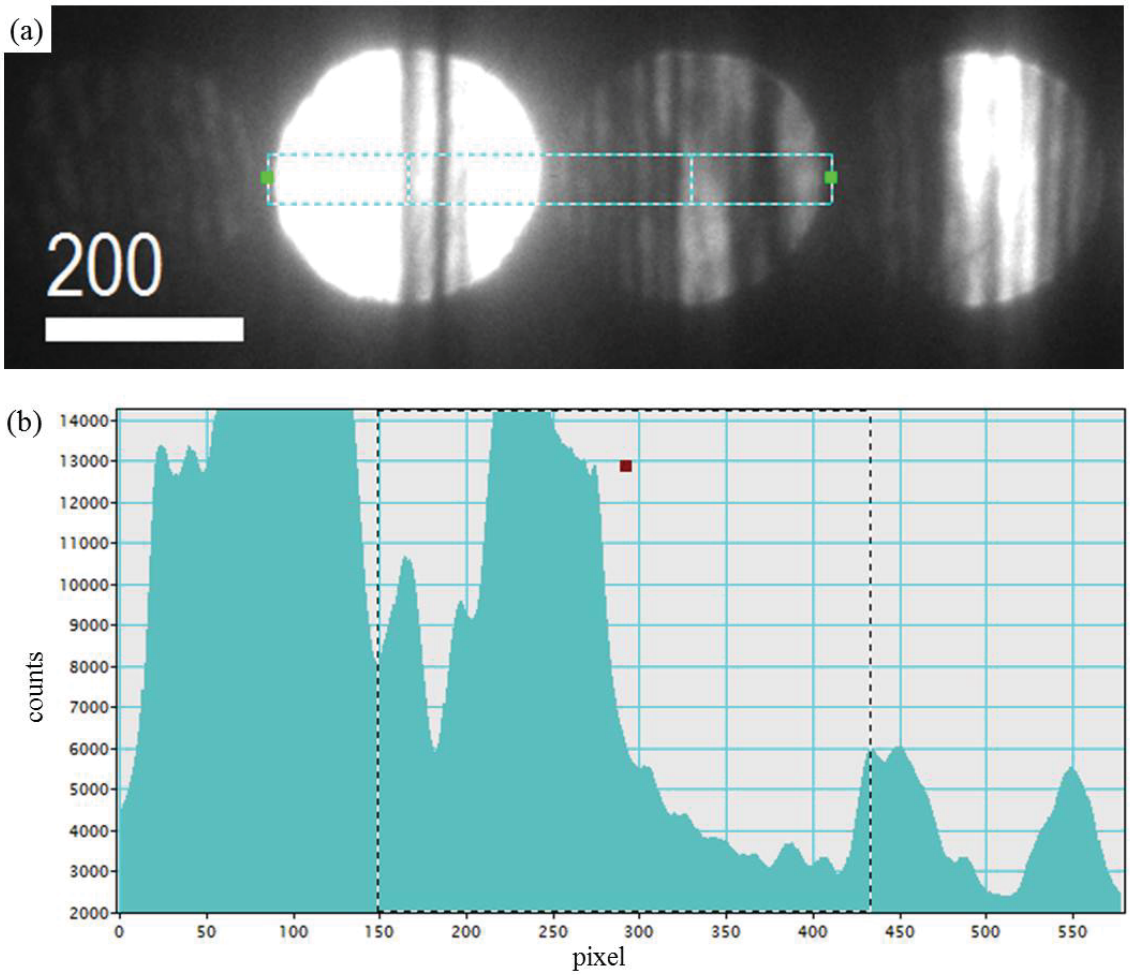

Fig. 3-5 $\Delta\theta_i$ measurement from the thickness fringes

The electron wavelength λ_0 at 200 kV is 2.51×1^{-3} nm, and $d_{(004)}$ of 4H-SiC is 0.2513 nm. Measured values of $\Delta\theta_i$ and calculations were shown in Table 3-1. The graphical plot of $(s_i/n_k)^2$ versus $(1/n_k)^2$ was shown in Fig. 3-6. From the intercept and the slope of the trend line, the thickness t = 475.1 nm and the extinction distance ξ_g = 126.8 nm were calculated out. Here it is necessary to emphasize that n started from 4 to plot a line closer to straight in the graph. It means the sample is 3 times more than the extinction distance. t/ξ_g = 3.75, which verified that the picking of the start of n and the thickness calculation were right.

Table 3-1 CBED data for thickness determination

i	**$\Delta\theta_i$**	**s_i**	**n_k**	**$1/n^2$**	**$(s/n)^2$**
1	26	3.63E-03	4	0.0625	8.25754E-07
2	46	6.43E-03	5	0.04	1.65424E-06
3	65	9.09E-03	6	0.027778	2.29376E-06
4	88.1	1.23E-02	7	0.020408	3.09585E-06
5	109.1	1.53E-02	8	0.015625	3.63491E-06
6	128.2	1.79E-02	9	0.012346	3.96565E-06

The thickness measurements on different positions of the window frame of TEM lamella varied, however the extinction distance were similar. 6 positions close the frame was measured and an average of extinction distance $\overline{\xi_g}$ = 135.5 nm.

In Fig. 3-4 (e) and (f) sample is so thin that *n* cannot start with an integer bigger than 1. Then Eq. 3-7 becomes

$$s^2 + 1/\xi_g^2 = 1/t^2$$

Then the thickness of point e and f were calculated and list in Table 3-2.

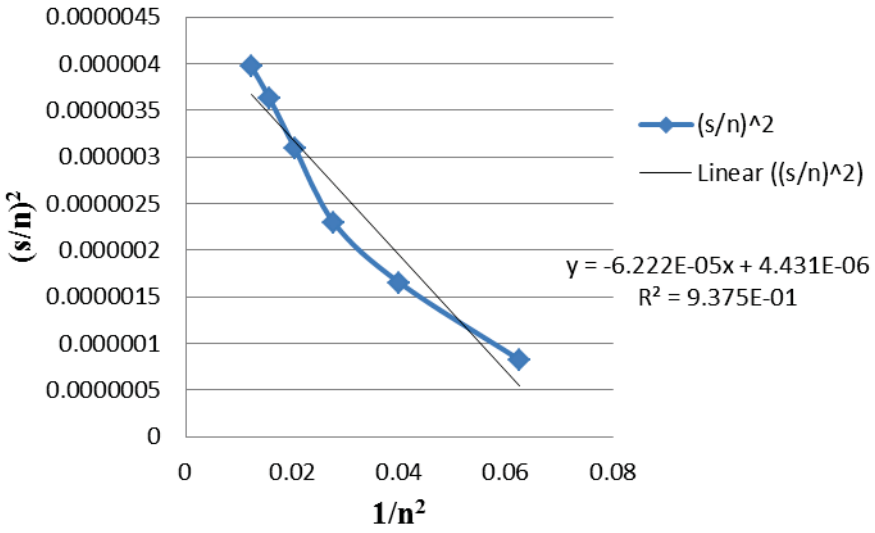

Fig. 3-6 $(s_i/n_k)^2$ versus $(1/n_k)^2$

Table 3-2 Thickness calculation at the thin area

	Δθ	**$2\theta_B$**	**s**	**$1/t^2$**	**t (nm)**
e	71.1	292	9.68E-03	1.49E-04	82.03
f	80.1	291	1.09E-02	1.75E-04	75.67

Compared the results from the two method of thickness measurement, it can be conclude that the sample had an uniform thickness of ~75 nm on SiC side near the SiC/SiO_2 interface, which is consistent with the EELS measurements.

Chapter 4. MODEL BASED QUANTIFICATION OF EELS

EELS has more advantages in light element detecting, however it requires a rather more sophisticated level of knowledge to carry the quantification out successfully. Here the conventional way of EELS quantification was briefly reviewed. Since it is not so satisfactory in practice, a more robust model based method was developed to analyze the EELS data more quantitatively.

4.1. Introduction to EELS quantification

The conventional quantification of EELS

Assuming that all the electrons have only undergone a single scattering event and forward scattered when they go through a thin sample, the absolute number of atoms per unit area of the specimen can simply be determined from EELS, according to the following equation:

$$N = \frac{I_K}{\sigma_K I_T}$$

Where N is the areal density (number of atoms per unit area) of the specimen, I_K is the intensity above background in the K edge, I_T is the total intensity in the spectrum, and σ is the ionization cross section.

If more than one element are quantified, it is easy to extend this expression to two edges from elements A and B, in which case the I_T drops out:

$$\frac{N_A}{N_B} = \frac{I_K^A \sigma_K^B}{I_K^B \sigma_K^A}$$

In reality there are some conditions, such as collecting all electrons over 4π sr, single scattering events, cannot be physically achieved, so the absolute chemical concentration and the composition ratio equation were modified to:

$$N = \frac{I_K(\beta\Delta)}{\sigma_K(\beta\Delta)I_l(\beta\Delta)}$$

$$\frac{N_A}{N_B} = \frac{I_K^A(\beta\Delta)\sigma_K^B(\beta\Delta)}{I_K^B(\beta\Delta)\sigma_K^A(\beta\Delta)}$$

where the intensity under a certain edge or the total intensity collected by the detector and the ionizing cross section became collection semi-angle (β) and background subtraction window (Δ) depended [51, 65].

The conventional way to treat core-loss EELS spectra consists of three steps. The first step is to remove the background by extrapolating a power-law function which is fitted in a region preceding the excitation edge. The second step is to remove the effect of multiple scattering by a deconvolution with the low-loss spectrum. The third step is the integration (I) of the number of counts in a certain energy region (Δ) under the thus obtained excitation edge. This number is then converted into an absolute chemical concentration (N) making use of a calculated cross section (σ) for the same energy region. Even though this method is most widely used, it has several disadvantages and inaccuracies. For the EELS quantification, the user has to choose a suitable window in order to fit the background. Depending on this choice the results may differ. Extrapolation under the excitation edge can make the outcome quite sensitive to the choice of window position. The result will depend on how far beyond the fitting region one wants to extrapolate. Furthermore, the assumption of the power law background is known to fail for wide energy regions. The second step, the multiple scattering deconvolution step, is usually based on Fourier techniques and can also introduce severe artifacts. Again choices have to be made which are not always apparent to the end user of commercial software. Finally, in the third step, cross sections are needed to convert the integrated number of counts under the excitation edge into chemical concentrations. Cross sections for excitation edges cannot be calculated exactly [65, 68].

Model based quantification of EELS

An alternative to the conventional treatment is model based quantification. In this approach, the recorded EELS spectrum is considered as an observation from which chemical or electronic information has to be extracted quantitatively. Then an expectation model with parameters was fitted to the observations. The fitted parameters can be directly related to chemical concentrations in the sample. As long as a good model is created to mimic all processes involving the EELS spectrum, the information, which is present in the spectrum in the form of physical parameters, should be accessible. Comparing to the conventional quantification there is no extrapolation and deconvolution involved and no fitting windows have to be chosen. All observations are taken into account on an equal footing [68, 69].

4.2. Microscope parameter calibration

For a quantificaiton of the ionization edges one need to know the convergence angle and collection angle accurately, which are necessary to calculate the corss section.

one can calibrate the convergence angle and collection angle by using the CBED pattern from a known crystal. Fig. 4-1 is a CBED pattern of 4H-SiC $[10\bar{1}0]$ zone axis. For a certain *hkl* disk in the CBED pattern, the Bragg angle θ_B can be easily calculated form the Bragg's law and the size can be measured from the CBED pattern, say *b*. It is the distance between the 000 disk and *hkl* disk, shown in Fig. 4-1. The diameter of the disks is determined by the size of the condenser aperture, which is the demission of the convergence angle 2α. Its size was measured as *a* in the CBED pattern. The shadow on the corner of the CCD image is the projection of the spectrum entrance aperture, which determines the collection angle 2β. A circle was drawn along with the shadow and its diameter was measured as *c* in the CBED pattern. Then the convergence angle and collection angle can be calculated with the following equations:

$$2\alpha = 2\theta_B \frac{a}{b}$$

$$2\beta = 2\theta_B \frac{c}{b}$$

During the EELS operation, the convergence angle does not change with the camera length (CL, or the post specimen projecting lens) of the electron microscope, in contrast the collection angle is inversely proportional to the camera length. Convergence semi-angle α and collection semi-angle β of Libra 200 MC were calibrated with the change of the camera length, and the results were listed in Table 4-1. The calibrate was carried out at the normal STEM operation conditions, which is the 20 μm condenser aperture, 650 μm spectrum entrance aperture running at 200 kV.

From the table one can see that the convergence angle is a constant for a certain condenser aperture. The mean value of the convergence semi-angle is 8.97 mrad for the 20 μm condenser aperture. 10000/β versus CL was plotted in Fig. 4-2, and the relationship between the collection semi-angle β and the camera length (CL) was fitted with the least-square method:

$$\frac{10000}{\beta} = 0.6718 \times CL + 3.0498$$

Collection angles can be extrapolated form the above equation if the CL is not listed on Table 4-1.

Total beam intensity, or beam current, is necessary to know for the absolute EELS quantification. It is usually measured with a nano-Ampere meter if the beam can be coupled to a Faraday cage, or measured on the virtual objective aperture (VOA) indirectly. The measured value is expressed as nA/s or (# of e^- /s). However in a spectrum the intensity is expressed with an arbitrary unit, counts. The intensity of a core-loss edge then has the unit of counts/s. In order to calculate the ratio of the intensity, the CCD camera needs to be calibrated. The total beam intensity can also be measured with the CCD camera if the beam is defocused, which reads as count. Since the exposure time of the CCD is known, the beam intensity can then expressed with the dimension counts/s. The quotient of the two values of the same beam current will give the conversion rate in the unit of e^-/counts or counts/e^-. The calibration was done for the CCD camera of Libra

200 MC, shown in Fig. 4-3. The conversion factor from counts to electrons was calculated as 0.0638 with linear regression.

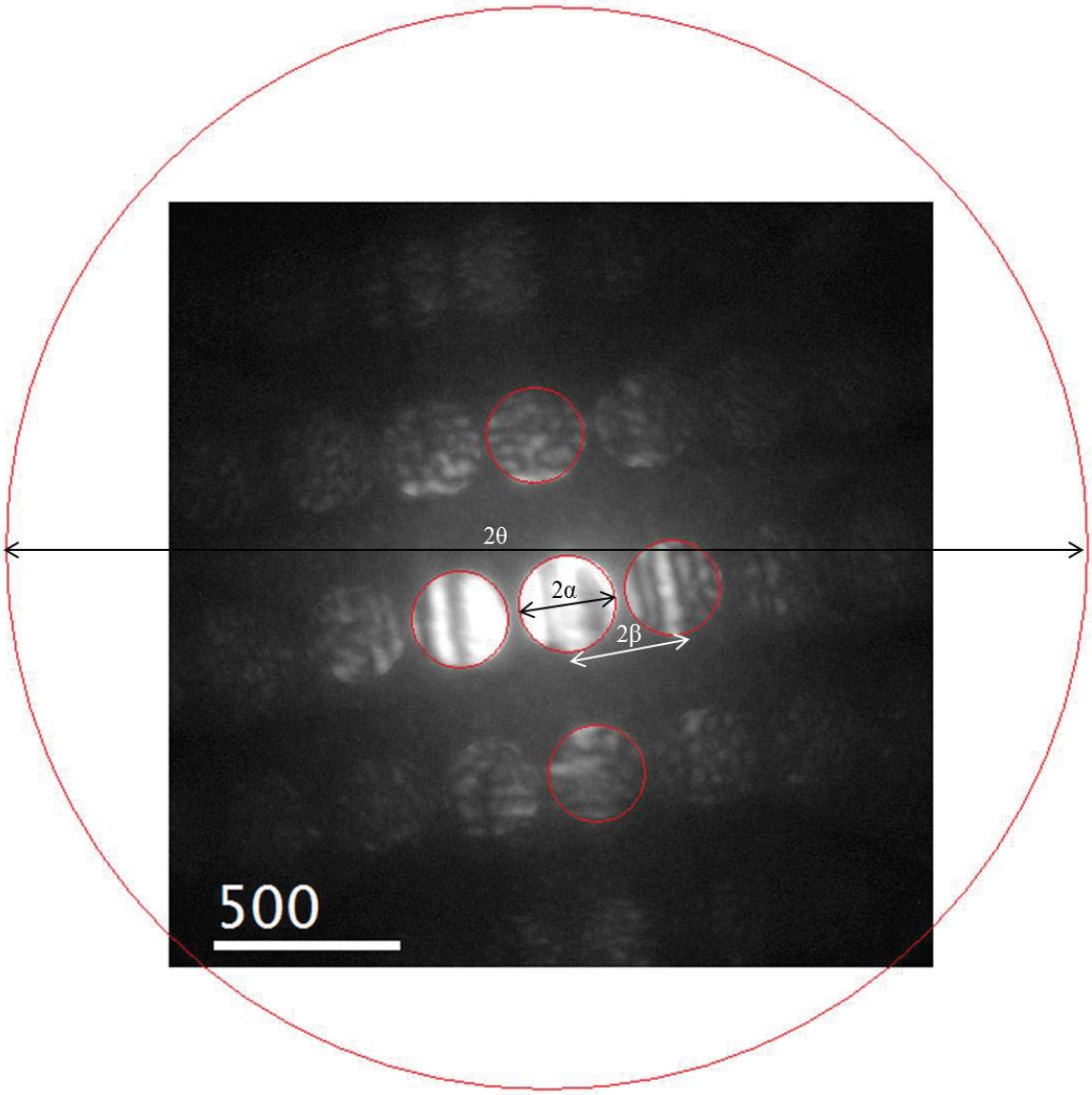

Fig. 4-1 Measurement of convergence angle and collection angle

Table 4-1 Convergence and collection semi-angle

CL (mm)	α (mrad)	β (mrad)
192	9.095768	81.00479
240	9.195876	70.44805
300	9.052863	53.49273
378	8.961913	39.65787
480	8.997955	30.27425
600	8.954683	25.46158
756	8.872334	19.60193
960	8.813049	14.96295
1200	8.942731	12.11844
1500	8.81183	10.35869

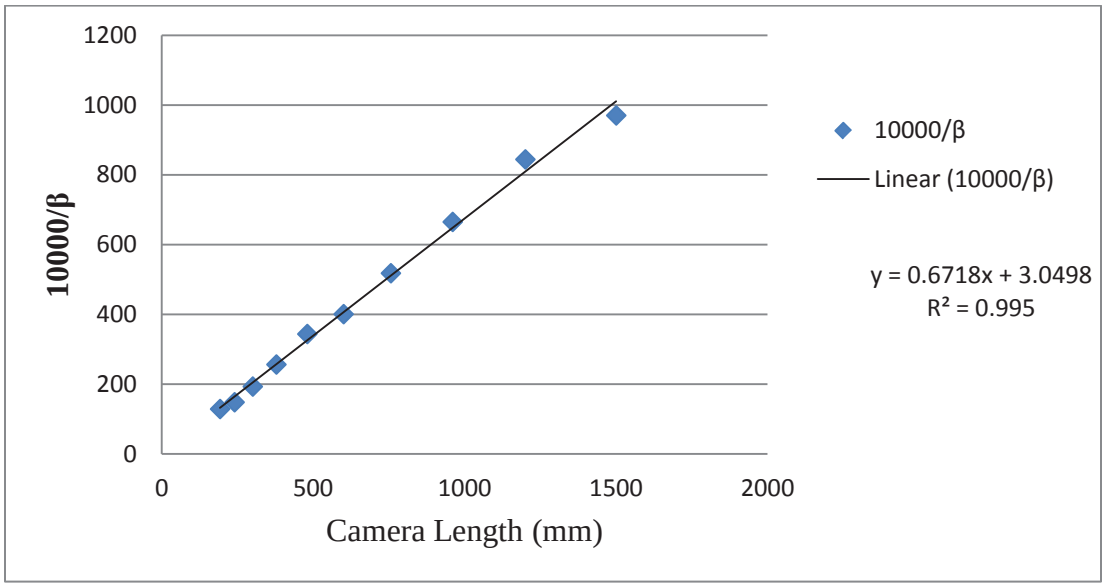

Fig. 4-2 Relationship between the collection semi-angle β and the camera length

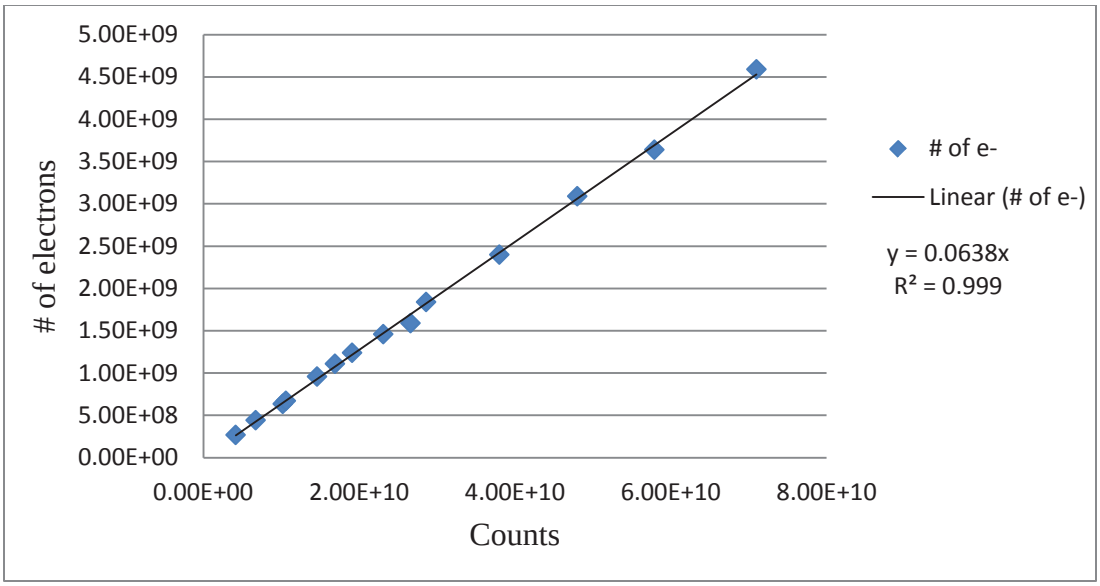

Fig. 4-3 Conversion factor of the CCD camera

With the conversion factor and the incident beam current one can calibrate the spectrum to scattering probability. Beside this, noise, signal response of the CCD camera and much more can be related to the input electrons and be studied then.

4.3. Quantifit program

A new model based quantification of EELS was developed by Duscher's group to quantify the EELS data more precisely, and all the analyzing processes were programed in to "Quantifit", which is user friendly and free [70]. Quantifit is written in python and uses a number of sophisticated packages such as matplotlib, Numpy and Scipy. The program can read spectra and spectrum images from all the usual formats. The model and data are stored in an ASCII format and therefore they can be read in almost any other program including the usual spreadsheet applications. The output of the analysis can

directly be saved in a spreadsheet and be plotted. The EELS spectrum analyses in this research were processed with “Quantifit”.

In Quantifit the model was built to fit the whole spectrum with background and cross sections excluding the solid state effected areas, demonstrated in Fig. 4-1. The original spectrum, which was filled with blue, contains a Si edge and a C edge. The model, shown in orange, fitted whole spectrum except for the edge areas containing the solid state effects. Cross sections of Si and C were convolved with a low-loss spectrum collected at the interface to match the edges. The fitting was done together with background subtraction and convolution of low-loss spectrum and cross sections. After fitting, edges and background were plotted in black and grey, respectively. The edges agree well with the background subtracted spectrum (Bgd Subt, shown in red).

Background modeling

The background intensity comes from plural scattering events which are usually associated with outer shell interactions. In addition to this, single scattering has the possible contributions to the background from the tails of preceding ionization edges. The most well-known and widely used background is the so called power law background $I = AE^{-r}$. The spectral intensity due to any single energy-loss process has a high-energy tail that approximates to a power-law energy dependence. Unfortunately, both A and r can vary across the specimen, as a result of changes in thickness, composition, incident beam energy and collection semi-angle β. That means the power law only fit in a limited energy range in a spectrum, or one have to do the background subtracting dividedly on each core loss edge.

In Quantifit the background was extended to

$$I = E^{-r} + b + cE + dE^2$$

in which the term b could move the background up or down, cE could change the slop of background and dE^2 could adjust curvature of the background.

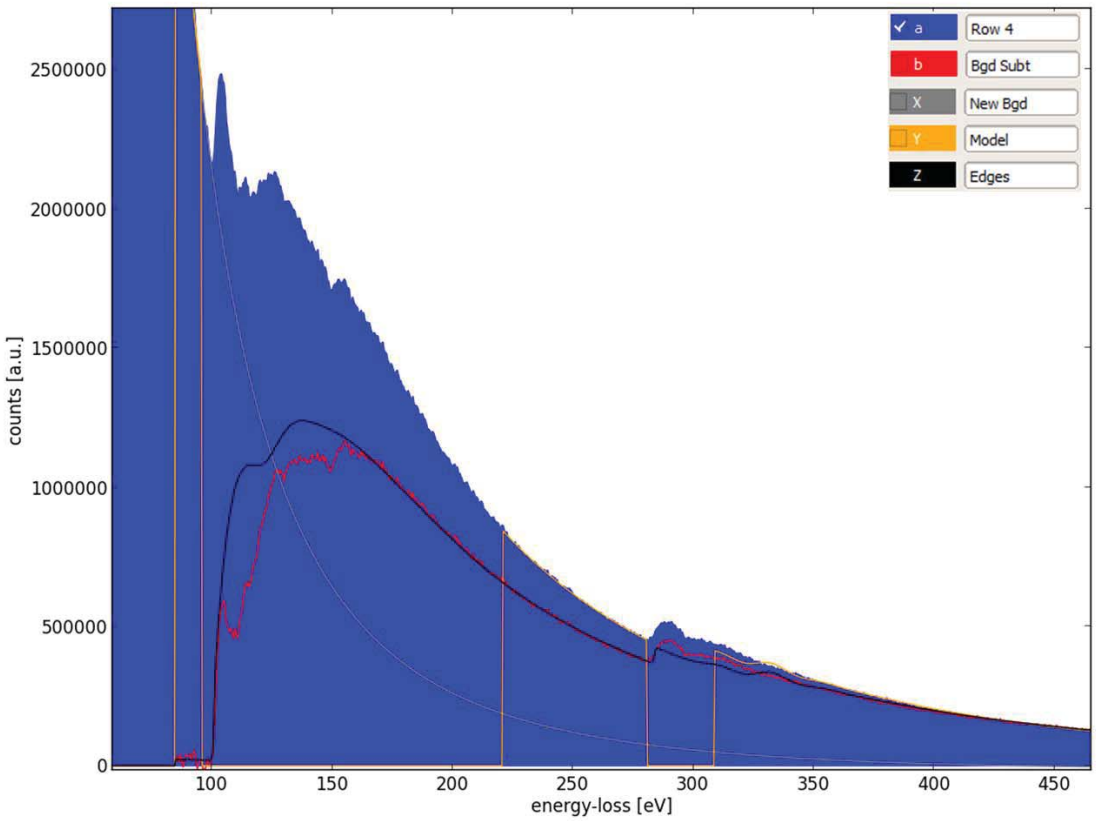

Fig. 4-4 EELS spectrum analyzed with Quantifit

Core-loss edge modeling

An ionization cross section of an atom can be theoretically calculated based on the single scattering assumption. As a result of the strong binding to the nucleus, inner shell excitation was therefore described to a good approximation using single atom models.

The simplest way of estimating the cross section is based on wave mechanics of the hydrogen atom. By approximating the atom to an isolated hydrogen atom with a charge on the nucleus equal to the atomic number Z of the atom, the Schrödinger's wave equation of the atom can be expressed analytically as the hydrogen atom wave function.

In consideration of the actual nuclear charge *Ze* and screening of the nuclear field by the remaining (Z-1) electrons, an effective nuclear charge is used in the Schrödinger's equation. In this way cross sections can be calculated with a modest amount of computing, and the cross sections are called hydrogenic cross sections.

Accurate wave functions have now been computed for most atoms by iterative solution of the Schrödinger equation with a self-consistent atomic potential. Hartree-Slater (HS) method represents a simplification of the Hartree-Fock (HF) procedure by assuming a central field within the atom. The resulting wave functions are close to those obtained using the HF method but require much less computing. The radial component of the ground state wave function has been tabulated by Herman and Skillman. For calculating the cross section, the final state radial function is obtained by solving the radial Schrödinger equation for a net energy, and the cross sections calculated in this way are HS cross sections.

In reality plural-scattering occurs when the e-beam penetrates a TEM sample, in contrast all the calculated cross sections are based on single scattering. Furthermore, the solid state effects change energy dependence of cross sections and of the scattered intensity. All the difficulties make it impractical to fit the near-edge fine structure of a core-loss edge in a real spectrum. The model used in Quantifit fits the whole spectrum with background and cross section excluding the solid state effected areas. A low-loss spectrum contains the thickness information of the sample, which is a measurement of the plural scattering effect. The plural scattering effect is then included in the model by a convolution of the ideal single scattering ionization edge and the low-loss spectrum.

The model can be expressed as:

$$M(\mathrm{E}) = \mathrm{aE}^{-\mathrm{r}} + (\mathrm{b} + \mathrm{cE} + \mathrm{dE}^2) + \mathrm{p_A}(\sigma_\mathrm{A}(\mathrm{E}) \otimes \mathrm{L}(\mathrm{E})) + \mathrm{p_B}(\sigma_\mathrm{B}(\mathrm{E}) \otimes L(E)) + \mathrm{p_C}(\sigma_\mathrm{C}(\mathrm{E}) \otimes L(E)) + \cdots$$

Eq. 4-1

Then the element concentration can be deduced from the fitting parameters in the model as:

$$\frac{N_A}{N_B} = \frac{I_K^A \sigma_K^B}{I_K^B \sigma_K^A} = \frac{(p_A\ \sigma_A\ )\sigma_B}{(p_B \sigma_B)\sigma_A} = \frac{p_A}{p_B}$$

Eq. 4-2

Both a composition profile and elemental mapping can be extracted from an EELS spectrum image.

Thickness correction is important during EELS data quantification. A model with a low-loss spectrum correction can improve the fitting a lot. Fig. 4-2 (a) is a fitting with the thickness correction. The Si and C cross sections were convolved with a low-loss spectrum collected at SiC side near the SiC/SiO_2 interface. Comparing with Fig. 4-2 (b) one can see that the edges match the 'Bgd Subt' much better.

Here the hydrogenic cross sections were used to avoid the artifacts with long energy range fitting, shown in Fig. 4-3 (a). Usually the Hartree-Slater cross sections are more accurate estimations for the scattering cross sections. However, Hartree-Slater cross sections are tabulated only up to a certain energy-loss. Beyond the tabulated values the cross section is often extrapolated with a power law. This extrapolation causes a negative background when applying the whole model fitting for a large energy range (from 80 eV to 650 eV in my analysis), which is obviously wrong, as demonstrated in Fig. 4-3 (b). Hartree-Slater cross sections are more accurate close to the edge onset; these areas are however excluded in the model based approach. In contrast, the model based analysis using hydrogenic cross sections fits the spectrum better in this situation.

After the model fitting, composition profiles can be deduced from the parameters in Eq. 4-1. From the composition one can see that the thickness correction is essential for the accuracy of the quantification. Without a thickness correction, the Si and C composition ratio in SiC, plotted with dash lines in Fig. 4-7, diverged from 50%, which is obviously wrong. And an amount of oxygen showed up in SiC, which are actually the noise in the spectrum and the error in the model. In this research O has a smaller cross section and higher energy loss compared with Si and C, and the concentration is tiny near the interface. Therefore a small error in the model or noise in the spectrum will cause a big fluctuation for oxygen.

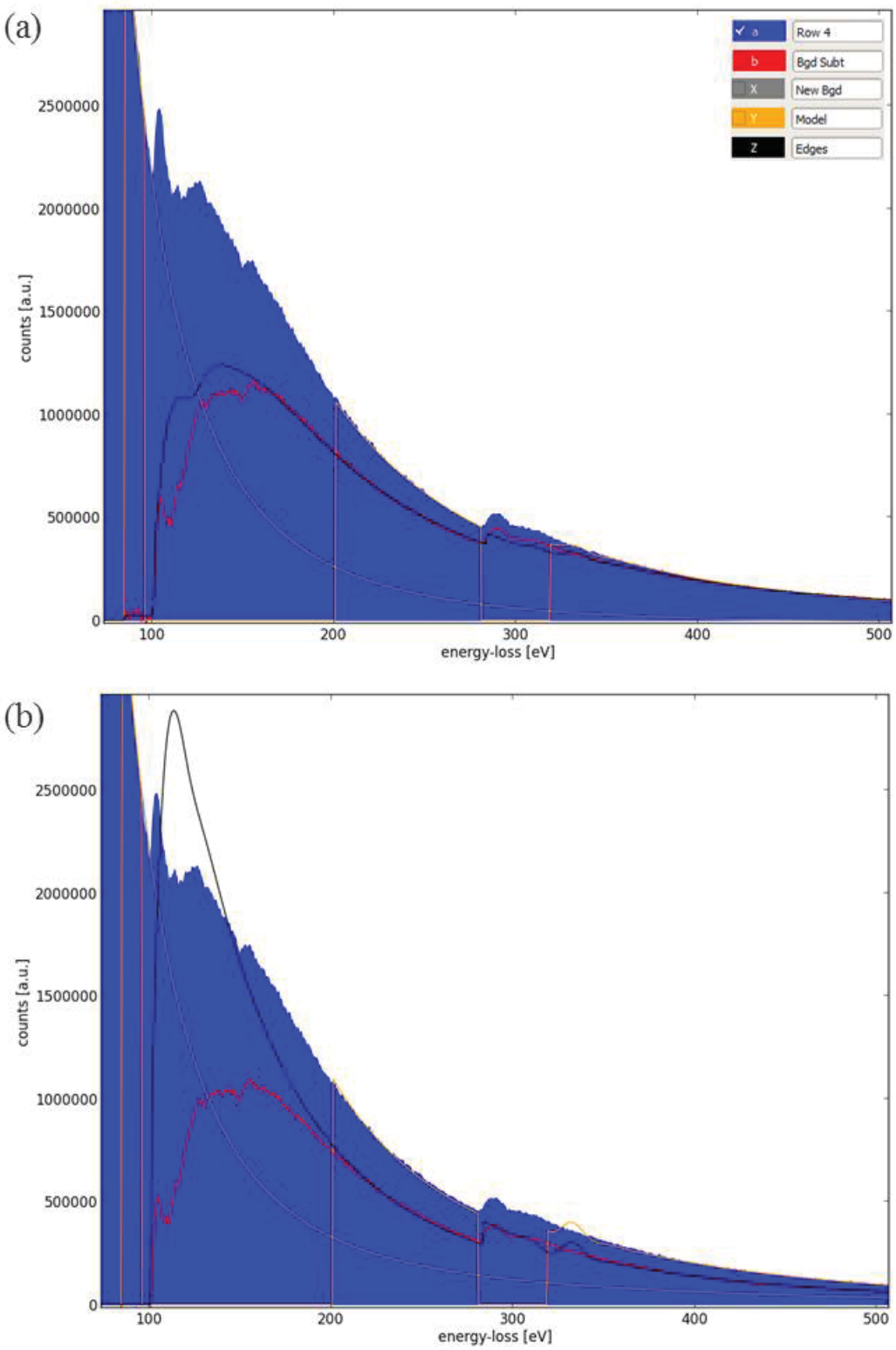

Fig. 4-5 Model fitting (a) with and (b) without low-loss correction

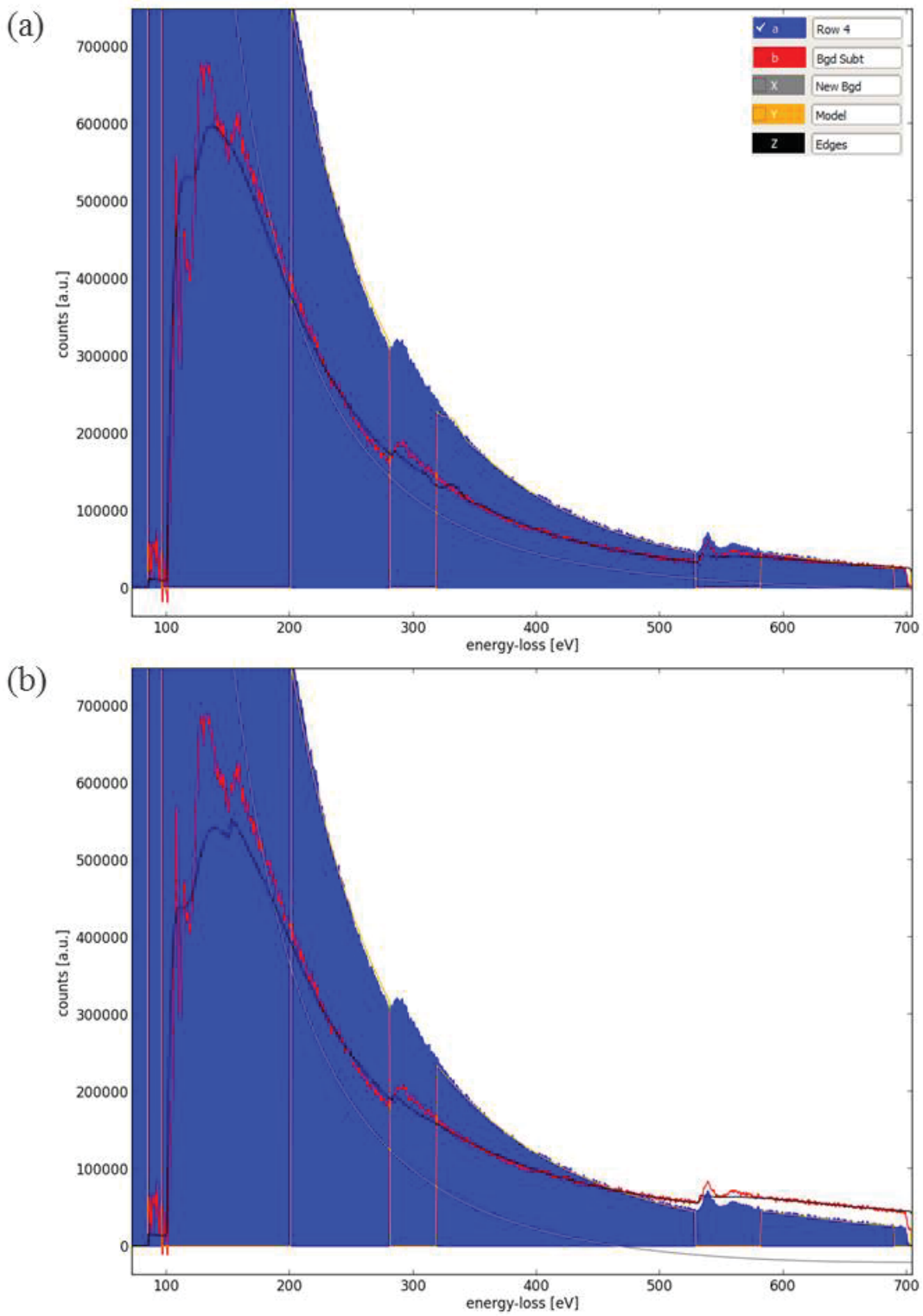

Fig. 4-6 (a) Hydrogenic cross sections and (b) HS cross sections used in the model

When the low-loss spectrum convolution was applied in the model, the Si and C compositions convergent to ~50% (solid lines in Fig. 4-7, Fig. 4-8) in the bulk SiC side, and the quality of O decrease to zero in SiC (orange line in Fig. 4-7, green line in Fig. 4-8), or decrease significantly to an error tolerance level even a wrong low-loss spectrum was used (orange dash line in Fig. 4-8).

A statistical survey was carried out on the results plotted in Fig. 4-7, and was tabulated in Table 4-2. The statistids of the compositions was from the bulk SiC side, which has a known component of 50% Si, 50% C and no oxygen. The standard deviation (STD DEV) of the composition is quite small, even when there is no thickness correction. This demonstrats that the model is very robust.

The real error was defined as:

$$\text{Real Error} = (STD\ DEV)/average \times 100\%,$$

And the absolute error (ABS Error) was defined as:

$$|average - composition| \,/\, composition \times 100\%$$

From the statics one can find that the model can give a reliable result with ~4 at.% error, which is a great improvement compared to the convetional quantification method with an error of 30% or higher [71].

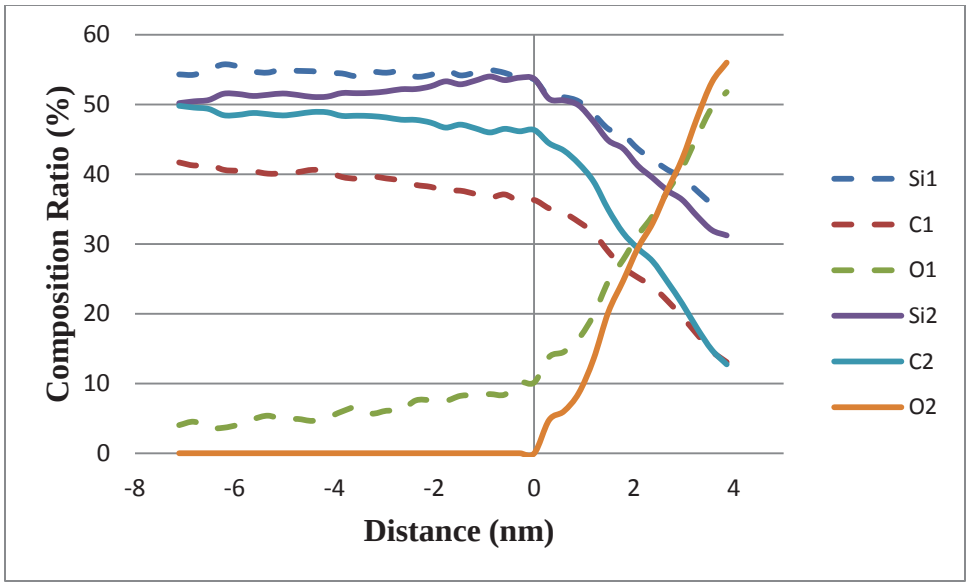

Fig. 4-7 Composition profile across interface without low-loss correction (1) and with low-loss correction (2)

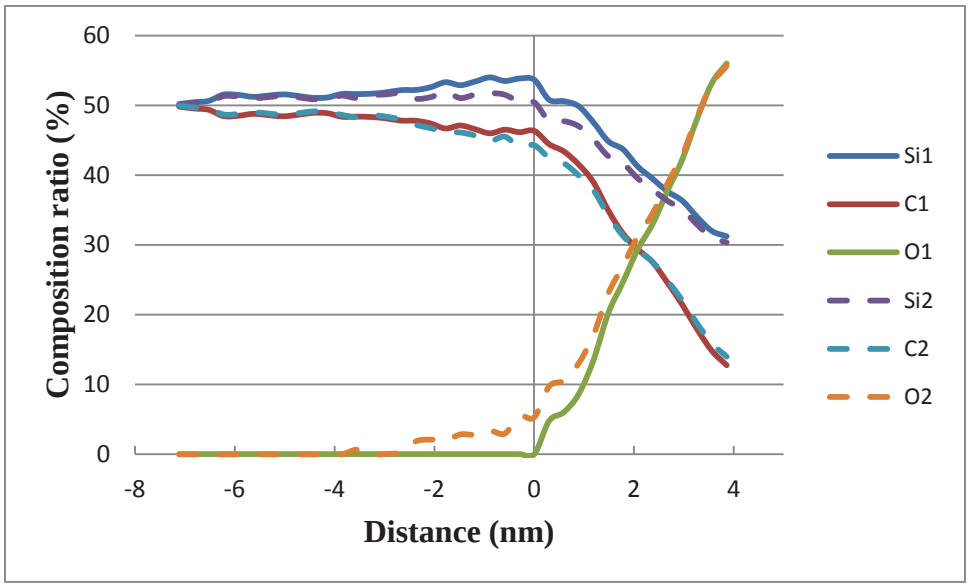

Fig. 4-8 Composition profile across interface corrected with different low-loss spectrum: (1) thickness = 0.551 IMFP, (2) thickness =1.001 IMFP

Table 4-2 Precision of the model based EELS quantification

	Si1	**C1**	**O1**	**Si2**	**C2**	**O2**
composition (%)	50	50	0	50	50	0
average (%)	54.55034	39.17427	6.275388	52.02685	47.97315	0
STD DEV (%)	0.485886	1.66721	1.939835	1.09787	1.09787	0
Real Error (%)	0.890711	4.255881	30.9118	2.110199	2.288509	0
ABS Error (%)	9.10068	21.65146		4.05369	4.05369	

Chapter 5. GEOMETRY OF THE INTERFACE

The steps of the vicinal surface are well-defined defect structures of atomic size for nucleation of low-dimensional nanostructures. Therefore the steps may enhance the epitaxial growth on the vicinal surface, or they can tune properties of functionalized nanostructure grown on the vicinal surface. Because of this reason the off-axis cut substrate are widely used. Similarly, the SiC substrates are intentionally cut with an off-axis cut angle. The substrates with a 4° or 8° off-axis cut along [11$\bar{2}$0] direction on Si face of SiC are widely used in SiC based MOSFETs, although the dielectric SiO_2 layer could be grown on an on-axis plane of SiC substrate.

The atomic structures between the on-axis cut and off-axis cut interface of SiC based devices are obviously different. And the SiC/SiO_2 interface is generally considered to be the cause for the reduced electron mobility of SiC power devices. To identify the role of interface in the mobility degradation, it is important to build a clear understanding of the interface structure between SiC andSiO_2. Vicinal interfaces with an 8° off-axis cut and an on-axis cut interface were studied in this chapter.

5.1. Tilting series

Seeing a vicinal interface from different crystallographic orientations the interface showed quite different morphologies. Fig. 5-1 is an example of that. Two TEM lamellas milled form the MOSFET fabricated on an off-axis cut SiC substrate. The off-axis cut is 8° off the [11$\bar{2}$0] direction on Si face of the SiC substrate. Fig. 5-1 (a) is a HAADF image of SiC near the interface with the [11$\bar{2}$0] zone axis. The top of Fig. 5-1(a) with a brighter contrast is bulk SiC (crystalline), and the lower part is SiO_2 (amorphous). From this zone axis, the steps at the interface cannot be seen. The projection of steps at the interface looks sharp and flat, like an on-axis cut interface. Fig. 5-1 (b) is a HAADF image of SiC near the interface with the [1$\bar{1}$00] zone axis. Steps and terraces on the vicinal interface can be clearly seen. However, the distribution of the steps is not uniform. The insets on

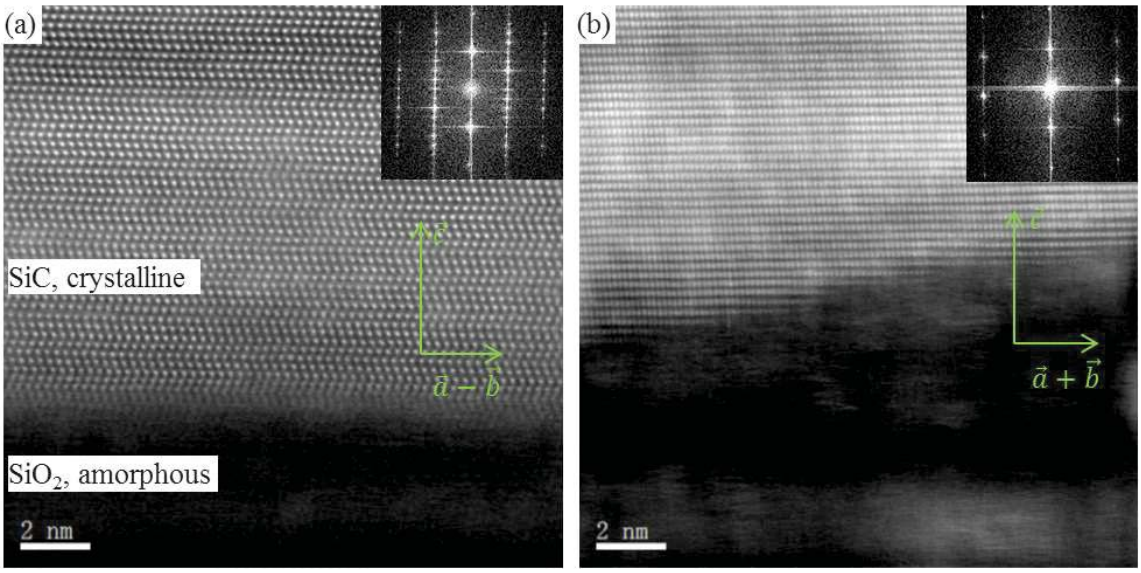

Fig. 5-1 (a) HAADF image with [11$\bar{2}$0] zone axis shows a flat edge at the interface. (b) HAADF image with [1$\bar{1}$00] zone axis shows steps and terraces at interface. The insets on the up right corners are the FFT diffractograms of the corresponding images. The green vectors show the directions in the images according to the basis vectors of 4H-SiC unit cell.

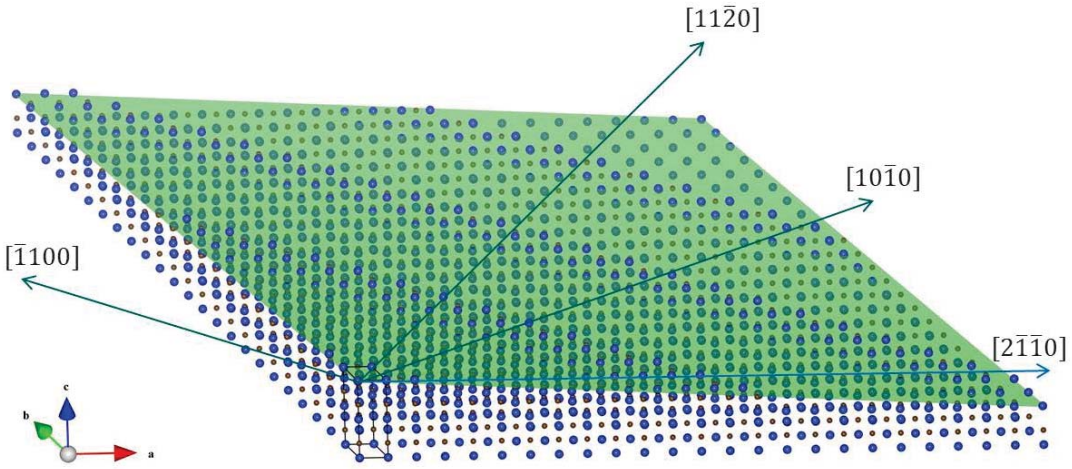

Fig. 5-2. Schematic of an 8° off-axis cut along [11$\bar{2}$0] direction on SiC (0001) face.

the upright corners of Fig 5-1 (a) and (b) are the fast Fourier transform (FFT) diffractograms of the corresponding images. The FFT diffractogram can represent the viewing direction of the image.

Cutting a crystal with a few degrees off a close packed direction at a close packed or low index plane will produce a vicinal surface. Steps of a vicinal surface can only be directly seen in TEM when the e-beam is perpendicular to the off-axis cut direction; otherwise it is a projection of steps.

To understand the vicinal surface better, an atomic model is shown in Fig. 5-2. (0001) Si face of 4H-SiC was cut along [11$\bar{2}$0] direction ($\vec{a}+\vec{b}$ direction) with 8° off. It can be represent by a (1 1 $\bar{2}$ 48) crystal plane. The clean SiC (1 1 $\bar{2}$ 48) plane consists of (0001) terraces with close-packed steps along [1$\bar{1}$00] direction ($\vec{a}-\vec{b}$ direction, or edge-on direction), which is perpendicular to the off-axis cut direction. In an ideal case the average terrace width is 12 atomic columns or 18.4 Å for one monatomic step. The steps of the vicinal surface could be seen along [1$\bar{1}$00] direction, and give a flat projection along [11$\bar{2}$0]. Based on the crystallography of vicinal interface, lamellas along the above mentioned crystallographic directions were milled with FIB technique and examined with TEM.

When the viewing direction changes, the steps caused by the off-axis cut will project differently in a TEM image. Thus the off-axis cut angle measured form the image will change. In the SiC vicinal surface model shown in Fig. 5-3(a), the off-axis cut goes along the black arrow, and the off-axis cut angle is denoted as α_0. If a TEM lamella is made along the off-axis cut direction, the viewed off-axis angle is α_0. However, if a TEM lamella is cut along the red arrow, the viewed off-axis cut angle will become to α_1. The geometry relationship of the two lamellas was sketched in Fig. 5-3(b). The red lamella can be interpreted as tilting the black one along the SiC [0001] direction with an angle θ. Form the schematic diagram it is easy to deduced that

$$\tan(\alpha_1) = \tan(\alpha_0) \cdot \cos(\theta)$$

Eq. 5-1

Since the TEM image is a 2D projection of a 3D objective, one should be careful to conclude on what he/she has seen just form a certain direction. The Zeiss Libra 200 MC TEM has a double tilting stage with a large tilting range (±70° around the sample holder rod and ±30° perpendicular to the sample holder), which enable the 3D tomography of a sample. A tilting series was carried out to image the vicinal interface in various crystallographic directions.

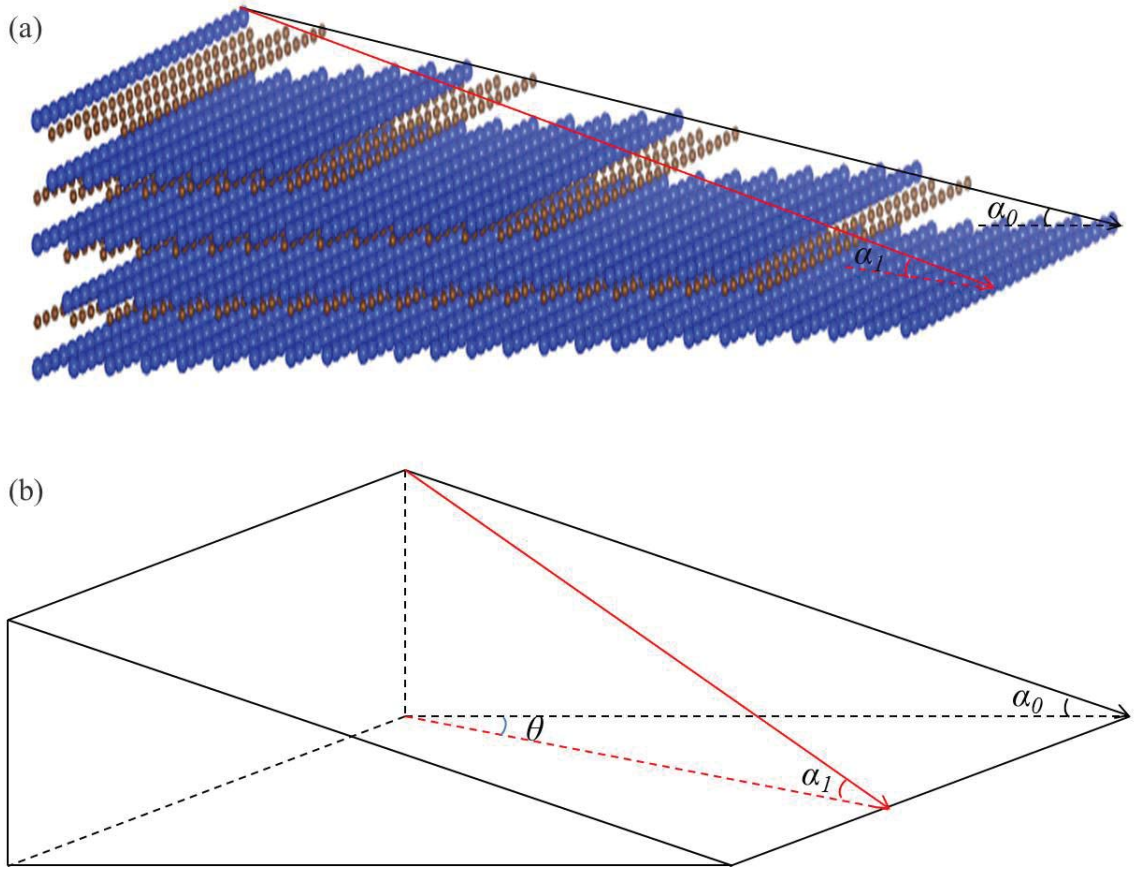

$$\tan(\alpha_1) = \tan(\alpha_0) \cdot \cos(\theta)$$

Fig. 5-3 Change of off-axis cut angle with different viewing direction

Before dong the tilting series, one need to be clear about the crystallographic directions of 4H-SiC. Viewing along c axis, the directions at (0001) plane is denoted in Fig. 5-4.

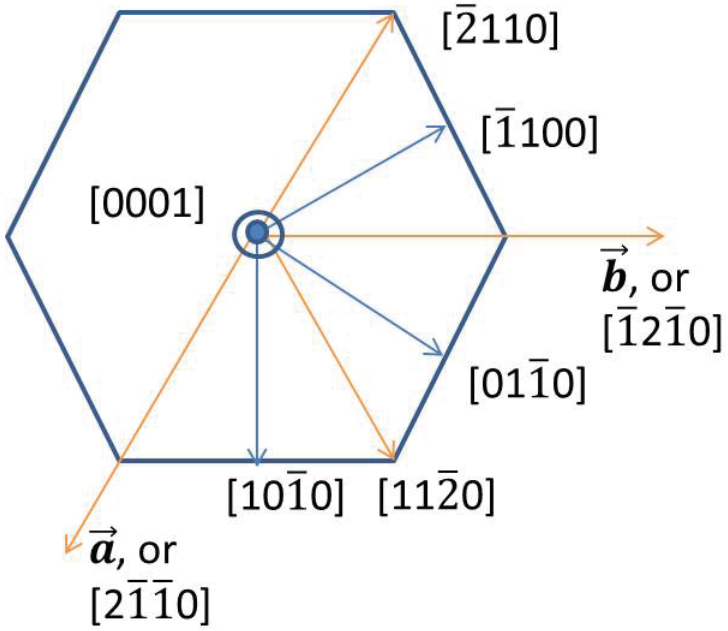

Fig. 5-4 Crystallographic directions of 4H-SiC

A lamella was milled along the off-axis cut direction ([11$\bar{2}$0]) and was examined first with the Libra 200 MC TEM. Fig. 5-5 is a HRTEM image of SiC at the interface viewing along the [1$\bar{1}$00] zone axis. The viewing direction is perpendicular to the off-axis cut direction [11$\bar{2}$0]. This viewing direction is the edge-on direction, from which direction all edges of the steps on the vicinal interface can be seen directly. The measured off-axis cut angle is 8.725°. Since the TEM lamella was prepared by FIB milling, gallium ions agglomerated into clusters and adsorbed on the surface of the TEM lamella, as labeled in Fig. 5-5 and Fig.5-6. Some of the gallium clusters formed crystalline nano particles.

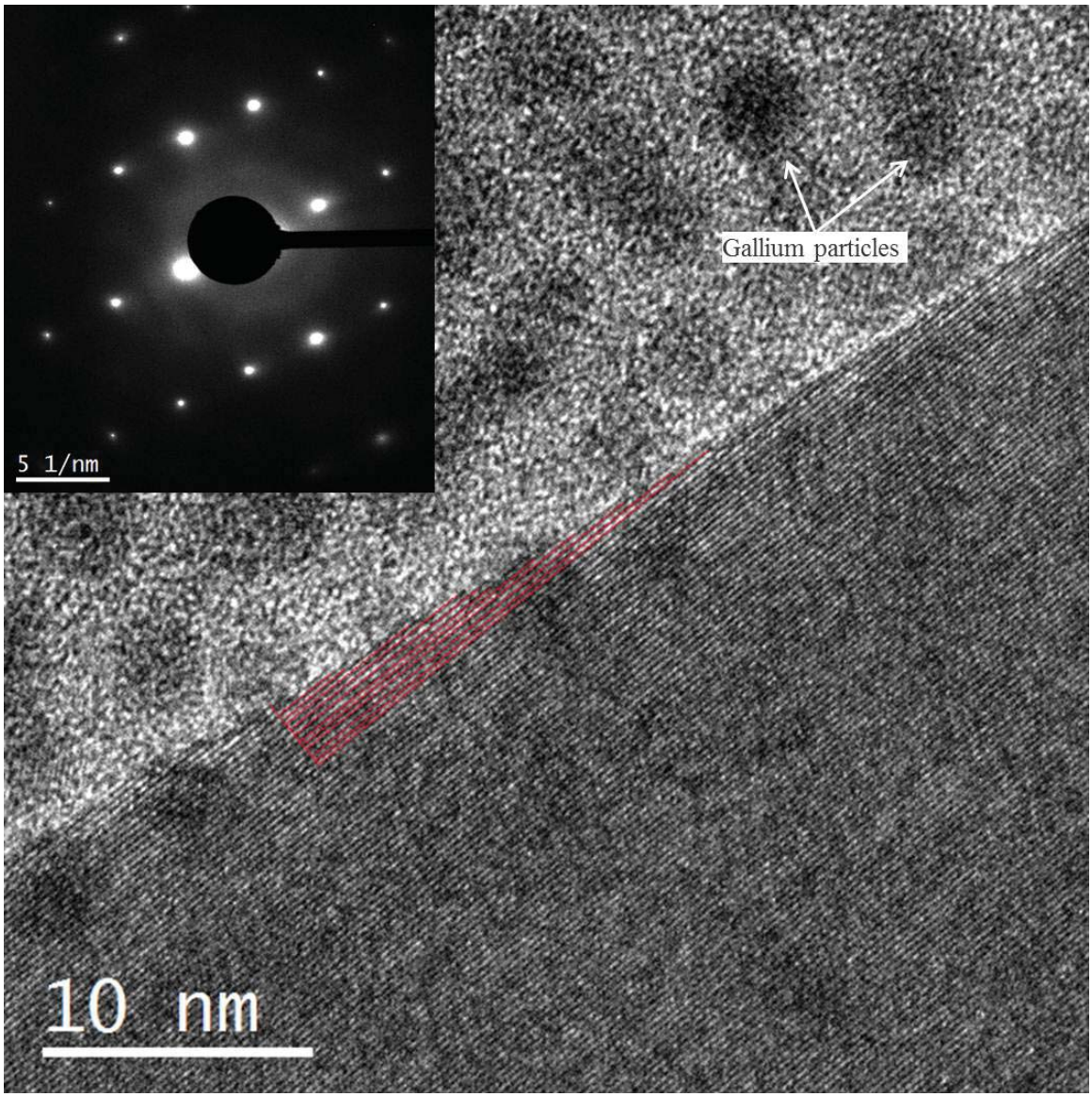

Fig. 5-5 HRTEM image of SiC at the interface viewing along [$1\bar{1}00$] zone axis. The viewing direction is perpendicular to the off-axis cut direction [$11\bar{2}0$]. The measured off-axis cut angle α_1 = 8.725°. The inset on top left is the selected area diffraction pattern of the image. The particles in the image are gallium cluster residues.

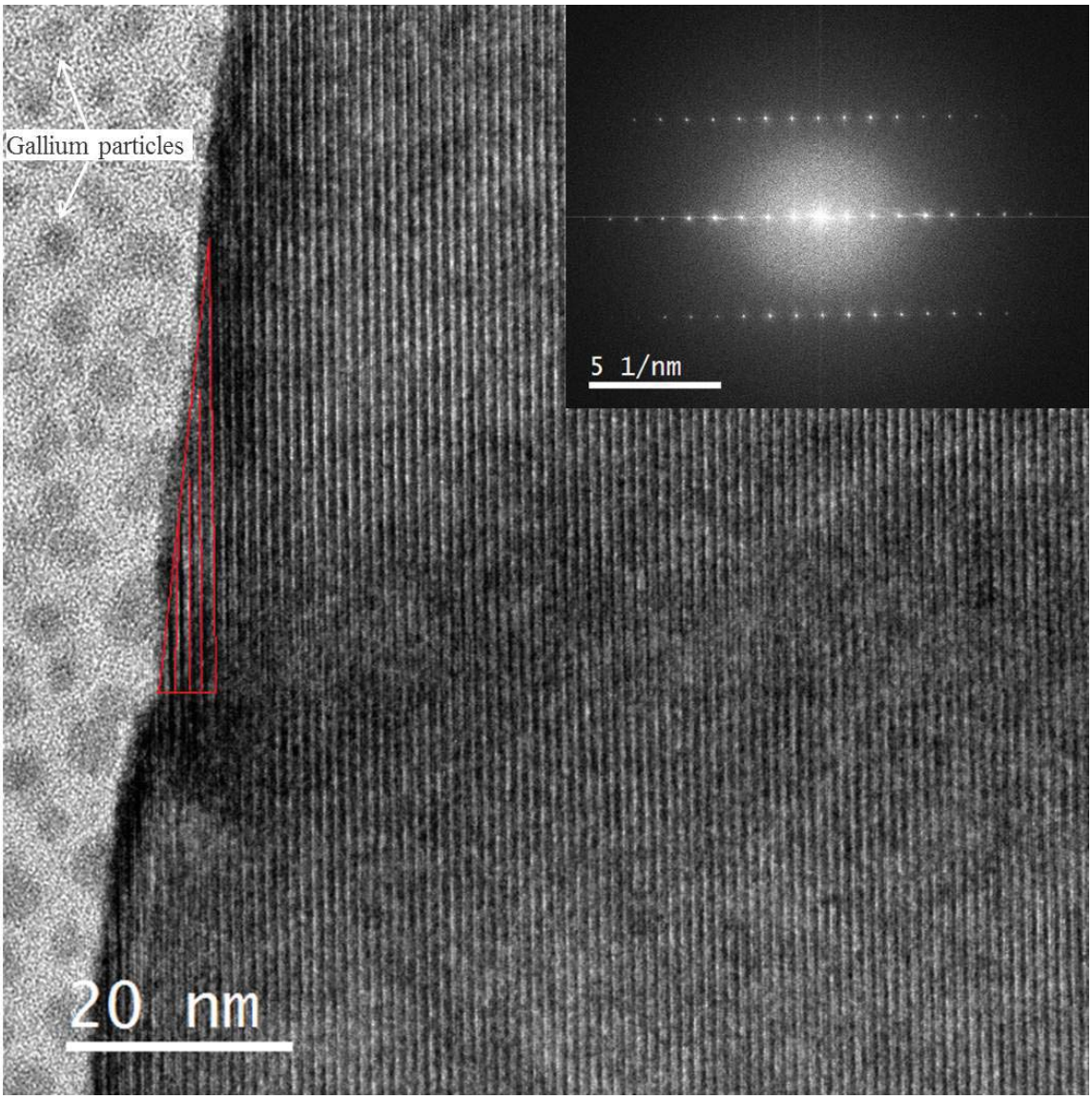

Fig. 5-6 HRTEM image of SiC at the interface viewing along $[2\bar{1}\bar{1}0]$ zone axis. Sample is tilted 30° away from the off-axis cut direction. The measured off-axis cut angle α_1 = 7.216°. The inset on top right is the FFT diffractogram of the image. Some steps below the red lines bunched together to form a nano-facet. The particles in the image are gallium cluster residues.

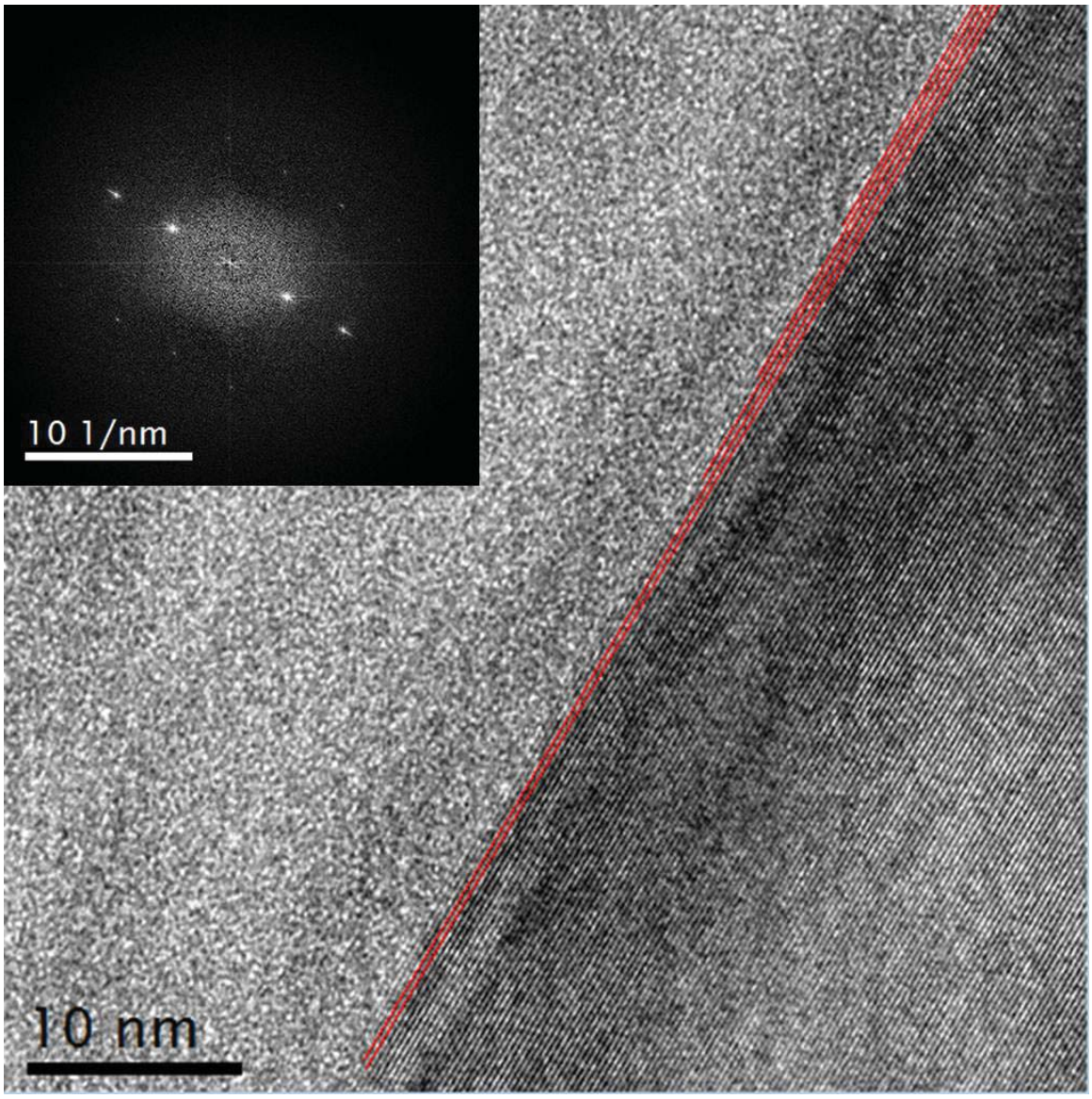

Fig. 5-7 HRTEM image of SiC at the interface viewing along [$10\bar{1}0$] zone axis. Sample is tilted 60° away from the off-axis cut direction. The measured off-axis cut angle α_1 = 4.166°. The inset on top is the FFT diffractogram of the image.

If the sample is tilt along the ***c*** direction of 4H-SiC 30° to the next low order Laue zone, $[2\bar{1}\bar{1}0]$ zone axis, the off-axis cut angle projected on the TEM image should become to 7°, according to Eq. 5-1. The image was shown in Fig. 5-6, and the measured off-axis angle α_1 is = 7.216°, which is the expected value. One can also see that some steps below the red lines in Fig. 5-6 bunched together to form a nano facet.

While tilting the sample along ***c*** direction of 4H-SiC another 30° to $[10\bar{1}0]$ zone axis, the projected off-axis cut angle will become to 4° according to Eq. 5-1. It is hard to image a so high-tilted sample directly in TEM because the window frame of the TEM lamella will shield the electron beam. However, the crystallographic structure of the lamella will be the same if one tilt a lamella milling along $[\bar{1}100]$ direction 30° to $[\bar{1}2\bar{1}0]$ direction. Now viewing the TEM lamella along $[10\bar{1}0]$ zone axis, the results are shown in Fig. 5-7. The measured off-axis angle α_1 is 4.166°.

From this tilt series the steps and terraces of the off-axis cut SiC/SiO_2 vicinal interface were imaged carefully. The results confirmed that the off-axis cut is 8° off the $[11\bar{2}0]$ direction, and the projections of the steps appeared differently from different viewing direction. Terraces or steps were not evenly distributed as the ideal case. The unevenly distributed steps bunched together at some positions to form nano facets at the interface.

5.2. Through focal series

To elucidate the crystal structure of the vicinal interface vividly, through focal series were performed along the $[11\bar{2}0]$ zone axis. A 3D atomic structure of the vicinal interface was constructed from the through focal Z-contrast image series. The interface structure of a 12 frame series is shown in Fig 5-8. In each frame the SiO_2 at the lower left corner was set to be transparent and the edges of steps were highlighted with green lines. The focus increment was 20 Å. Seeing through $[11\bar{2}0]$ direction, a 18.4 Å (~2 nm) change in focus is corresponding to a distance of one (0004) plane of SiC. From the lower left to up right of Fig. 5-8, an average of one atomic line vanished for each 2 nm focus increment. Those lines are the (0004) planes of SiC on the off-axis cut steps. The results agreed very well

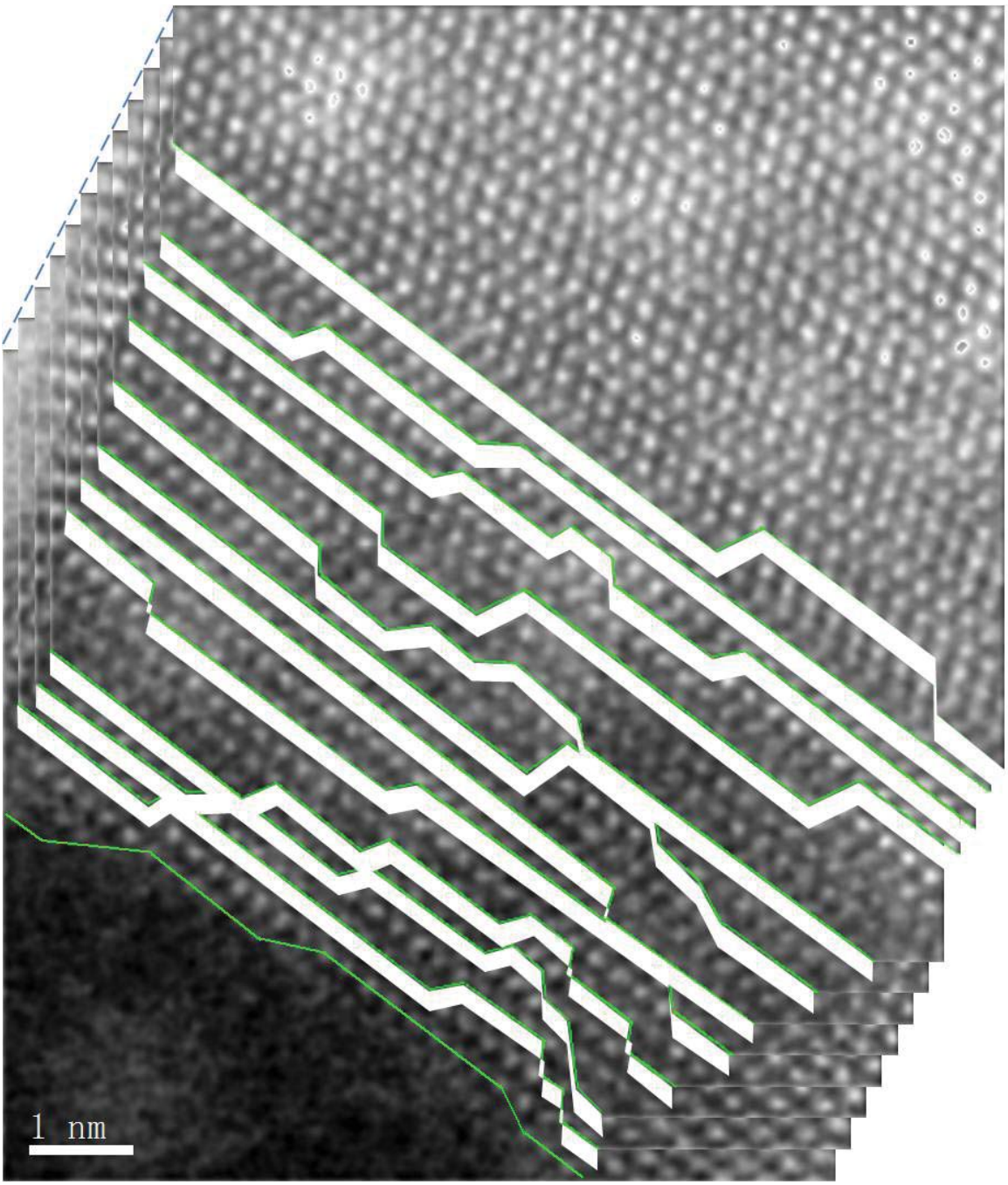

Fig. 5-8. Through focal Z-contrast image series with a focal step 20 Å along [11$\bar{2}$0] zone axis. Step edges were highlighted and the amorphous SiO_2 part at the lower left corner of each frame was set to be transparent. Monoatomic steps showed up one by one with every changing focus depth.

with the model in Fig 5-2. It is for the first time that a 3D SiC/SiO_2 vicinal interface was resolved directly with STEM.

From the atomic resolution Z-contrast through focal image series one can clearly see that the vicinal surface was not as flat as the ideal case. Steps of the vicinal interface are not always straight. In contrast, kinks were very common and widely distributed on the steps, and protruded in and out the terraces. Also, steps bunching can be seen.

A vicinal surface deviating from the ideal not only has steps and terraces along the off-axis cut direction, but kinks along the steps. This deviation from the ideal is defined as the roughness of a vicinal surface/interface. And the steps will undergo bunching and meandering during the oxidation process[72, 73]. Some steps can bunch together to form micro facets, which will further increase the roughness of the interface.

In the literature, epitaxial growths on the vicinal surface, such as MgO film on Ag (100) vicinal surface [74] and NaCl film on Ge (100) vicinal surface [75], were studied. Mosaic patterns formed during the epitaxial growth in order to relax the strain caused by lattice mismatch between substrate and epitaxial film. Although SiO_2 does not have an epitaxial relationship with the SiC substrate, the Si-O bond is quite strongly covalent and directional. Similarly, the crystal structure of the SiC/SiO_2 vicinal interface will affect the oxide growth, and further, affect the electronic properties of devices. Furthermore, the compositions at the interface will obviously be affected by the viewing directions. These effects will be discussed in the next chapter.

Chapter 6. COMPOSITIONS OF THE INTERFACE

A clear understanding of the crystallography of the SiC/SiO_2 interface is the first step to interpret the compositions and the transition layer width at the interface. The transition region is a state between the SiC substrate and SiO_2 layer, and composition profiles across it show how the compositions change from SiC to SiO_2. Since the transition layer width is directly connected to the performance of transistors, this knowledge may then be used to improve processing conditions. The morphology and crystallographic direction of the interface can be determined with Z-contrast imaging and the composition profiles can be extracted from spectrum images (SI). When interpreting the composition profiles we should correlate the changes with the measuring direction because the steps of the vicinal interface will be projected differently along different directions. STEM imaging with simultaneous EELS spectra is a good way to achieve this goal. Transition regions of off-axis cut samples with 2 different directions were examined. An on-axis cut sample was also investigated. All those results are discussed in the following paragraphs.

A sample with the vicinal interface was studied first. An 8° off-axis sample was observed along the off-cut direction. Fig. 6-1(a) is a HAADF image at SiC/SiO_2 interface viewing along $[11\bar{2}0]$ direction. While performing the STEM image scan, a simultaneous EELS spectrum was recorded with the pixel size of 2.5 Å to form an EELS spectrum image, shown in Fig. 6-1(b). A large pixel size in the spectrum images was necessary to prevent the interface from strongly focused e-beam damage. And a sub-pixel scanning with a shorter dwell time was also conducted to collect these SI. Thus the resolution of the simultaneous EELS spectra was only limited by pixel size, which was in turn limited by the sample stability under the electron beam. The scanning area for EELS spectra is indicated by the green box in Fig. 6-1(a). The pixels in each column were summed, shown in the red rectangle, to give a higher signal-to-noise ratio spectrum. The areal density of each element in the sample was extracted from the spectrum. Composition profiles at the interface were then calculated and curves were plotted in Fig. 6-1(c). The sum of all the element compositions was normalized to 100%.

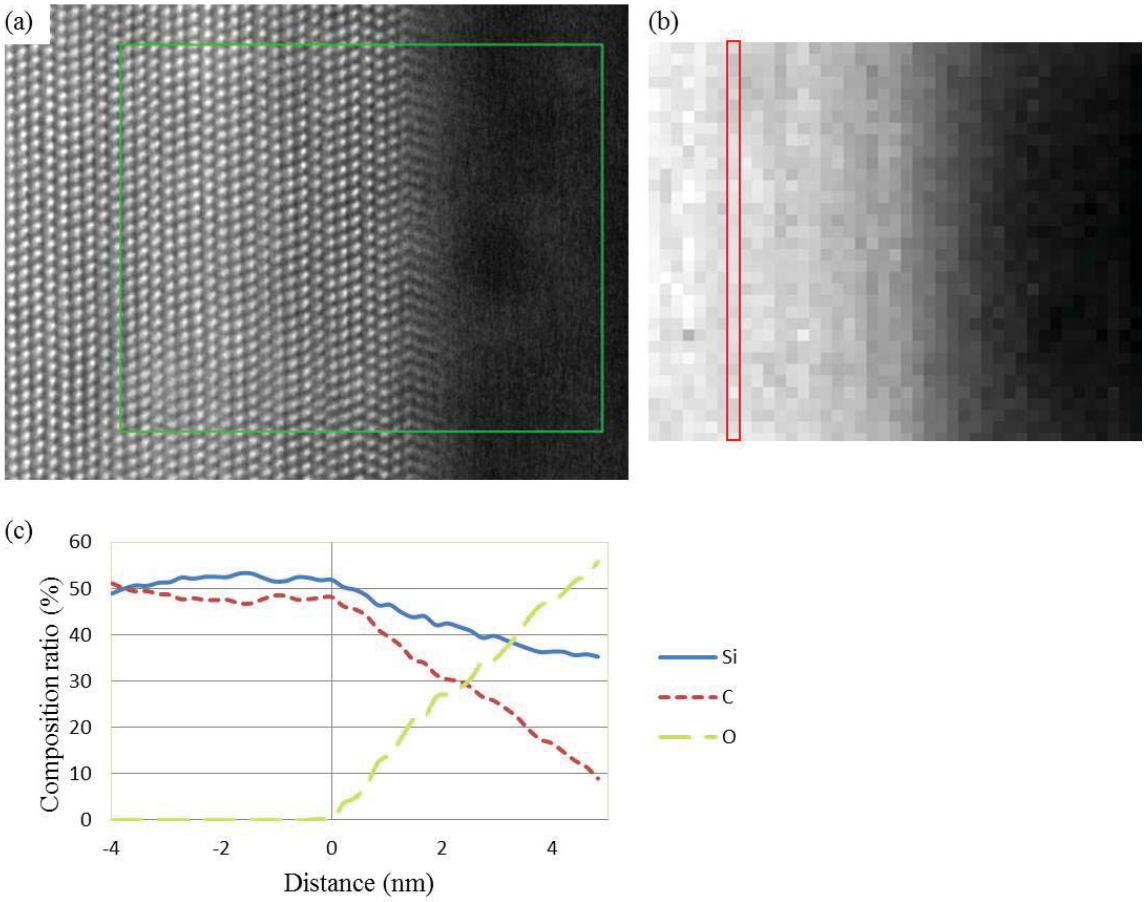

Fig. 6-1 (a) is an HAADF image of 4H-SiC viewing along [11$\bar{2}$0] zone axis. SiC substrate has an 8° off-axis cut along that direction. In the green box EELS spectra were collected to form a spectrum image, shown in (b), with a pixel size of 2.5Å. Spectra in every column of the spectrum image are added up to form a high signal-to-noise ratio spectrum. (c) is the element composition profiles extracted from the spectrum image.

From the composition profile shown in Fig. 6-1(c) one can see that in the bulk SiC part (left side) the Si and C were 50 at% respectively. This result showed the high reliability of the analysis technique, because no further adjustment was performed. Oxygen was not detected in SiC as expected. The beginning of the interface was defined by the presence of oxygen. Beyond the interface a gradual decrease of silicon and increase of oxygen were observed. However, quite a large amount of carbon can still be detected in a more than 5 nm range, which is much larger than a measurement error. This implies that the steps and kinks caused by the off-axis cut at the interface play a non-negligible role, and have to be considered in the interpretation of TEM results of the vicinal interfaces.

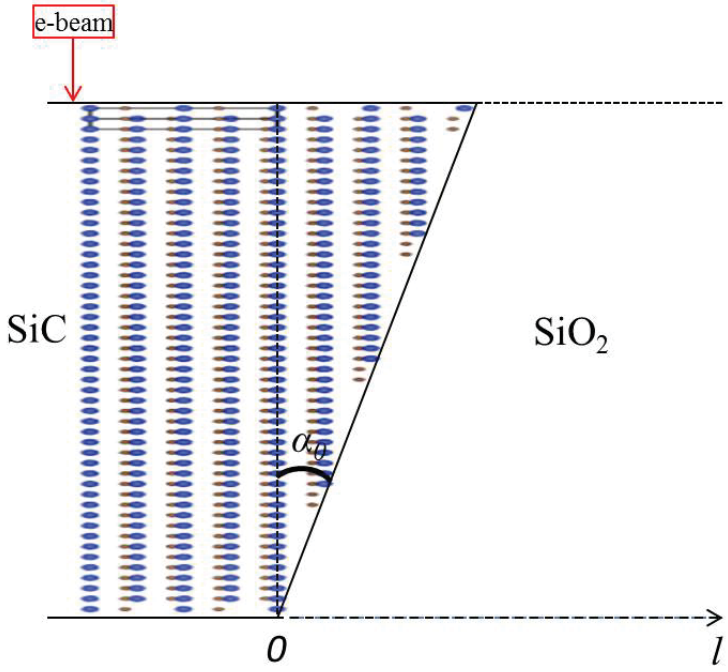

Fig. 6-2 Schematic diagram of the e-beam scan across the SiC/SiO_2 vicinal interface

Since the e-beam is parallel to the off-axis cut direction, the projection of the vicinal interface appears sharp like an on-axis interface. In fact the projection is a terraced region of SiC and SiO_2, shown in Fig. 6-2. A vicinal interface model was built as following: A 50 nm thick sample will have the combined region with a width of *50·tan(8°)* nm, about 7 nm. If the distance from the start of interface is *l*, the concentration of elements (Si, C and O) in this terraced region should be a function of *l*. In order to build these functions, it is assumed that the amorphous oxide layer of SiC has the same density as α-quartz. If the atomic density of Si atoms in 4H-SiC is *D*, the atomic density of Carbon in SiC is *D*, Silicon in SiO_2 is *0.55D*, and Oxygen in SiO_2 is *1.1D*. Then at the position *l*:

Number of Si or C in SiC in a unit volume:

$$\frac{7-l}{7} \times D$$

Number of Si in the oxide in a unit volume:

$$\frac{l}{7} \times 0.55D$$

Total number of Si in a unit volume:

$$\frac{7-l}{7} \times D + \frac{l}{7} \times 0.55D$$

So the composition ratio of C/Si and O/Si are

$$\mathrm{C/Si} = \frac{7-l}{7-0.45l}$$

Eq. 6-1

$$\mathrm{O/Si} = \frac{1.1l}{7-0.45l}$$

Eq. 6-2

Plotting the Eq. 6-1 and Eq. 6-2 in Fig. 6-3(a) and (b) respectively. They agree with the experimental data well. Projection of steps along the measuring direction is a sufficient explanation for change in chemical composition. The result means that the interface of

SiC/SiO_2 is chemically sharp and there is no nonstoichiometric region. The small composition deviation between the measured and the calculated value may be ascribed to the roughness of the vicinal interface or to the precision of the method.

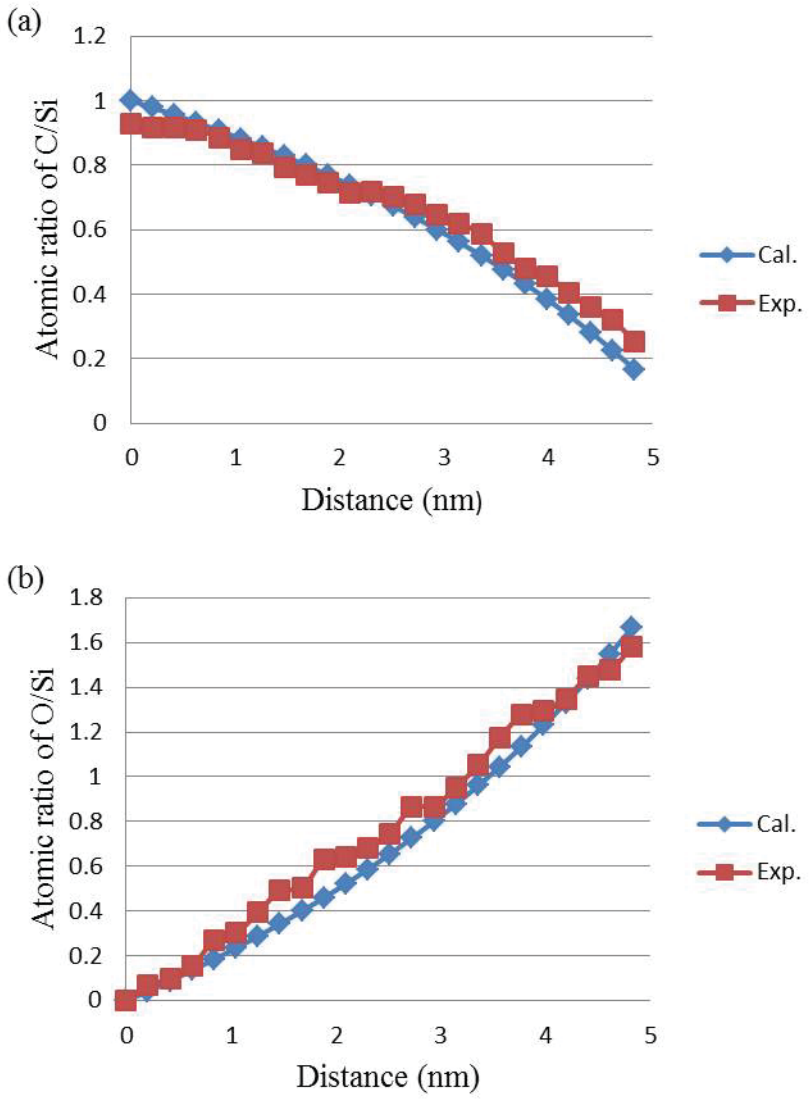

Fig. 6-3 (a) and (b) are the composition ratio of carbon/silicon and oxygen/silicon respectively, from the interface to the SiO_2 side of the sample. The red square curve is the experimental data and blue diamond curve is the calculated values.

To increase the confidence in determining the roughness from composition profiles derived from EELS spectra, a sample with steps parallel with the e-beam was studied. If the off-axis cut sample was tilted to the step edge-on direction to eliminate the artificial projection of vicinal interface, abrupt chemical change from SiC to SiO_2 should be seen. In order to verify this claim, another sample normal to $[1\bar{1}00]$ direction was examined with the same method described above. Fig. 6-4(a) is a Z-contrast image of the sample with simultaneous EELS spectrum at the interface. Steps and terraces at the vicinal interface were clearly observed, and the SiC/SiO_2 interface was abrupt. According to the composition profiles extracted from the spectrum image one can see that the left side is perfect SiC and the right side is SiO_2, and at the interface a nonstoichiometric region of less than 2 nm is observed. The disordered region again demonstrated that the interface was not flat at atomic scale. The unevenly distributed terraces go in and out from the vicinal surface a few atomic layers, corresponding to a ~2 nm roughness. The roughness of the interface may explain the ~2 nm composition fluctuation region.

To further study the roughness at interface, an on-axis cut sample was examined. Indeed very few steps were observed in the atomic resolution TEM, as shown in Fig. 6-5, and a chemically abrupt interface was observed. The STEM/EELS results shown in Fig. 6-6 are a Z-contrast image and composition profiles at the interface. The pixel size is 1 nm for the simultaneous EELS spectra. The interface has a fluctuating region of 2 pixel width. The real width of the transition region cannot be bigger than 2 nm because of the resolution limit of pixel size. As it is mentioned in chapter 4, elemental maps can also be extracted form a spectrum image. Si, C and O compositions were calculate in every pixel in the spectrum image. Each pixel in the spectrum image have a one to one corresponding relationship to the pixel in the Z-contrast image shown in Fig. 6-7(a) and then the elemental maps formed. The element mapping is displayed in Fig. 6-7 (b), (c) and (d). At the interface, fluctuations of each element in the mapping are the same with the corresponding composition profile, but displayed in two dimensions. The roughness of the on axis-cut interface is in agreement with the roughness of the off-axis cut sample.

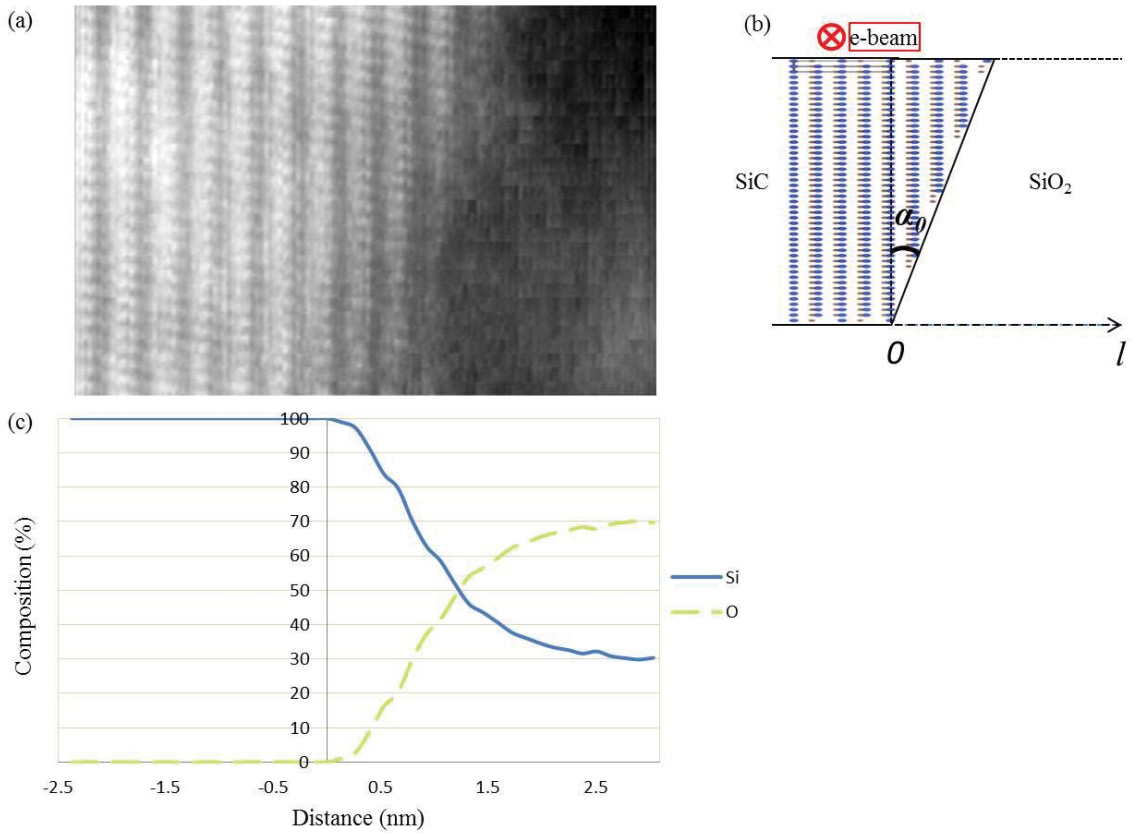

Fig. 6-4 (a) Z-contrast image of the interface viewing along [1$\bar{1}$00] zone axis. (b) shows the relationship between electron beam direction and the interface. From [1$\bar{1}$00] zone axis the steps can be clearly seen. Simultaneous EELS spectra are collected at this area and the Si and O composition profiles are plotted in (c).

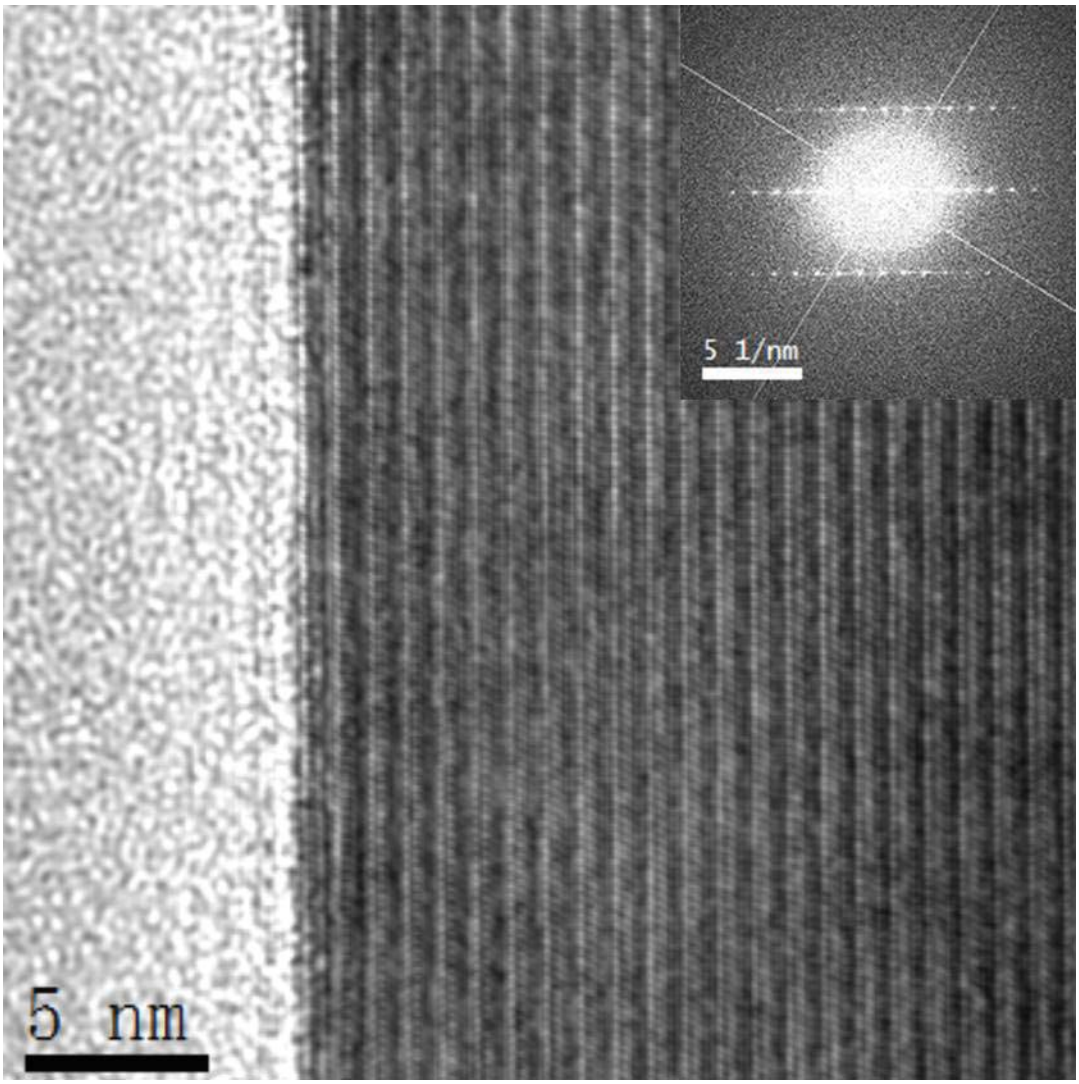

Fig. 6-5. HRTEM image of an on-axis cut sample interface along [11$\bar{2}$0] zone axis. Abrupt 4H-SiC/SiO_2 interface was observed. The insert at top right is the FFT diffractogram of the HRTEM image.

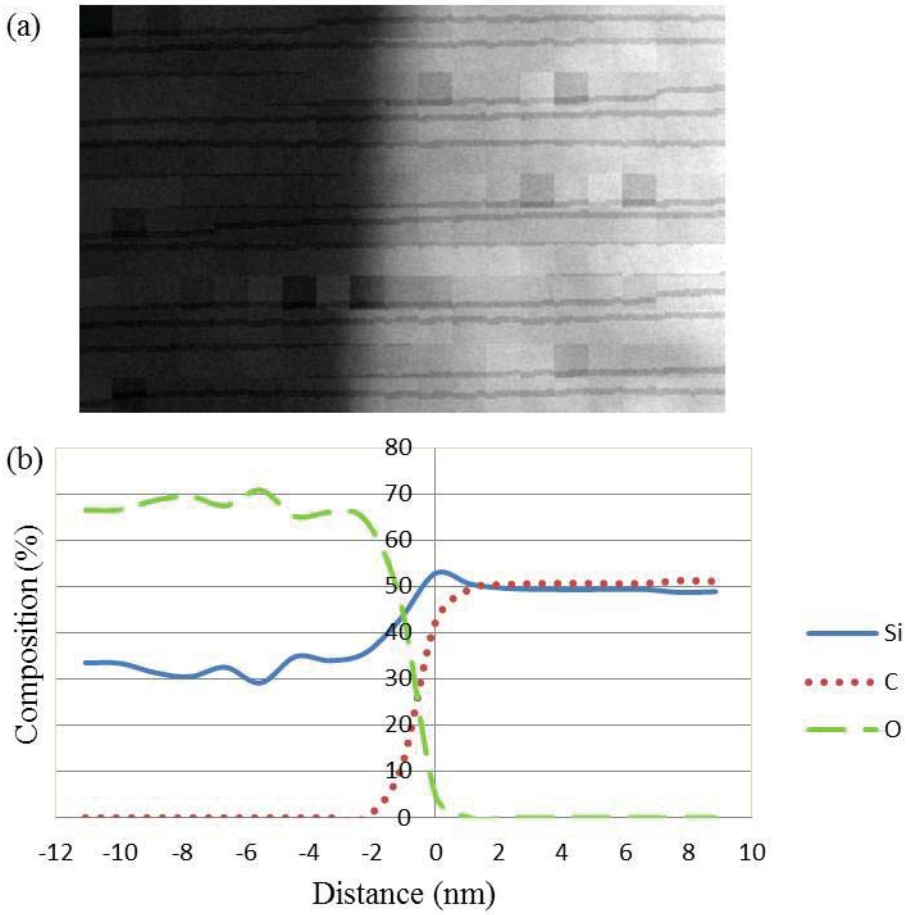

Fig. 6-6 (a) Z-contrast image of an on-axis cut sample at the interface. Simultaneous EELS spectra were collected at this area and the Si, C and O composition profiles are plotted in (b).

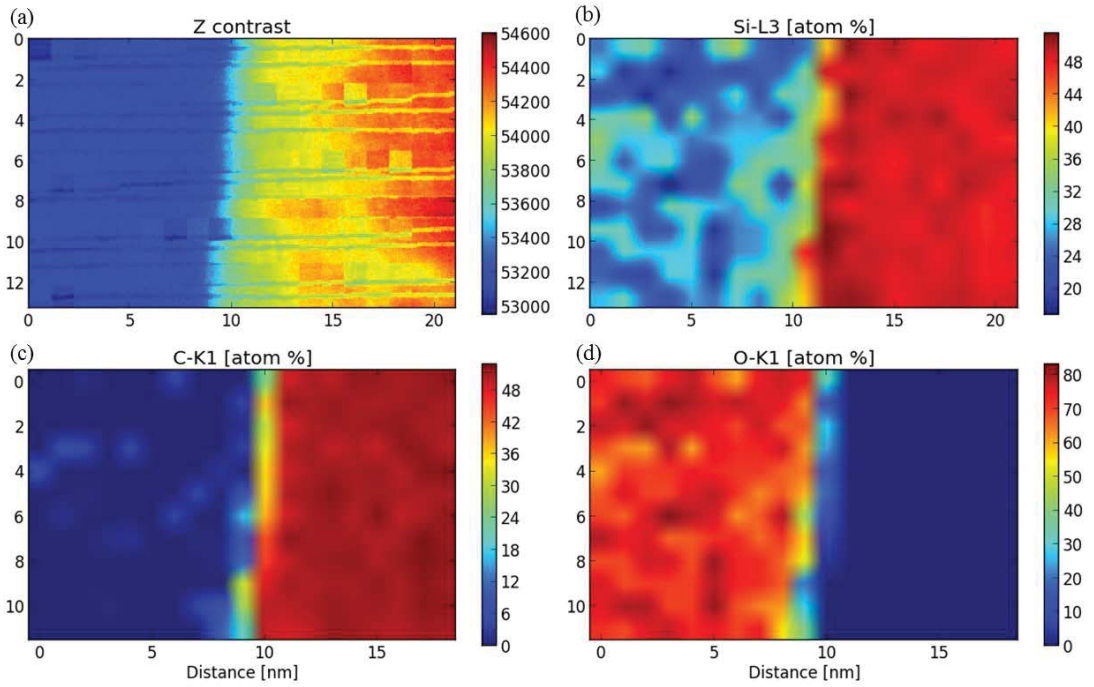

Fig. 6-7 Z-contrast image of the on-axis cut sample at the interface and the corresponding elemental maps of Si, C and O.

The three representative conditions give strong evidence that the SiC/SiO_2 interface, including the on-axis cut, is not absolutely flat but has a roughness in atomic scale. The roughness amplitude of kinks, step endings and nano-facets at interface (or generally speaking, roughness of the interface) in various directions is less than 2 nm, and has the same dimensions as the inherent transition layers of the SiC/SiO_2 interface reported by Biggerstaff et al.[35]. The roughness is independent of crystallographic orientation.

Chapter 7. CHEMOMETRICS ANALYSIS

If one see closely the fine structure of the Si edges at SiC/SiO_2 interface, the start of Si edges change gradually from 99.8 eV at SiC side to 104 eV at SiO_2, as shown in Fig. 7-1. The energy-loss near-edge structure (ELNES) of an ionization edge represents approximately a local density of states of the atom giving rise to the edge. According to this common claim, one may guess that the bonding state of Si at the interface was different from that in SiC or in SiO_2, and thus an intermediate bonding state such as Si-C-O may exist in the interface. Actually the change of the ELNES here is misleading because of the roughness of the interface. Atomic models representing the roughness contain too many atoms to launch a first principle calculation for the Si bonding states. In quantum molecular dynamics simulations the excess carbon bonded to Si atoms at the interface will segregate over picosecond time scale though it has up to 20% carbon excess [36]. In contrast, it is more reliable if the excess carbon at interface was ascribed to the overlap of SiC steps and SiO_2 layers. In this chapter the composition at the interface is interpreted from the analytical chemistry point of view.

In the analytical chemistry various spectroscopic techniques, such as hyphenated chromatography, emission-excitation fluorescence spectroscopy and multipulse nuclear magnetic resonance spectroscopy, were developed to map the chemical composition of a mixture. In modern chemometrics a comprehensive approaches were developed to extract the concentrations of a mixed system from the multivariate chemical measurement techniques. Chemometrics was introduced by Svante Wold [76] and Bruce R. Kowalski [77] in the early 1970s. Wold defined it as “how do we get chemical relevant information out of measured chemical data, how do we represent and display this information, and how do we get such information into data?’’ [76]. If one treats the SiC/SiO_2 interface as a multicomponent mixture, it will be quite simple and can be classified to the so called white multicomponent system in chemometrics. In a white multicomponent system the spectra of the chemical species present in the samples, or spectra from samples that contain possible coexisting interference in addition to the desired species, are all available. Then the aim is just to determine quantitatively the concentrations of some or

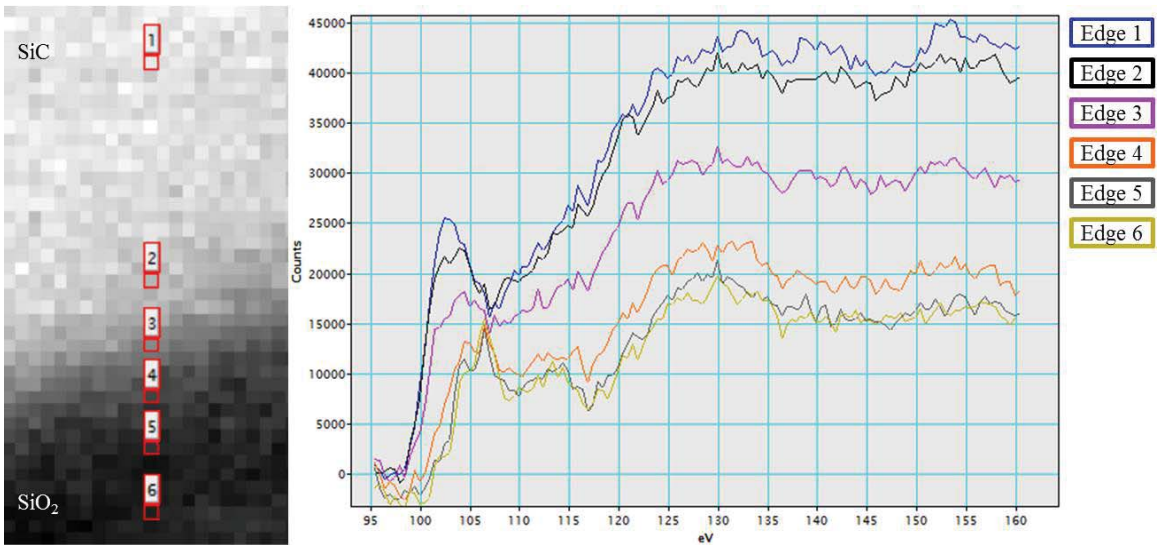

Fig. 7-1 The change of Si edge from SiC to SiO_2 at the interface

all chemical species. Methods for this kind of analysis are relatively mature and do almost always provide excellent results [78].

In a white multicomponent system the component in the system is already known and their spectra can be used as the sensitivity coefficient spectral vectors. Multivariate data obtained from spectral analysis can be approximated as linear systems according to the Beer-Lambert law:

$$\boldsymbol{x} = c_1\boldsymbol{s_1} + c_2\boldsymbol{s_2} + \cdots + c_n\boldsymbol{s_n} + \boldsymbol{e}$$

Where $\boldsymbol{x}$ is the response vector (spectrum) measured from a mixture, $\boldsymbol{s_i}$ ($i = 1, 2, 3,\ldots, n$) is the spectrum form a pure component in the mixed system and $\boldsymbol{c_i}$ is the concentrations. $\boldsymbol{e}$ is a residual vector containing measurement noise.

Fig. 7-2 is an EELS spectrum image at SiC/SiO_2 interface, taken with Libra 200 MC TEM. Spectrum in each pixel is a measurement response. The SiC/SiO_2 interface was vertical and spectra in each vertical column were added up to give a high signal to noise

ratio spectrum. Each of the add-up spectrums can be treated as a column vector X_i and then formed a response matrix X. In the spectrum image, the first left column and the last right column can be assumed as pure SiC and SiO_2 respectively because they were far enough from the interface. These two column vectors built up the sensitivity matrix Y. The concentrations of SiC and SiO_2 in each X_i were unknown and they were put into a concentration matrix C. According to the Beer-Lambert law,

$$\boldsymbol{X}_{(n,M)} = \boldsymbol{Y}_{(n,2)} \cdot \boldsymbol{C}_{(2,m)} + \boldsymbol{e}$$

Eq. 7-1

The concentrations of each component can be obtained by solving the above equation [79].

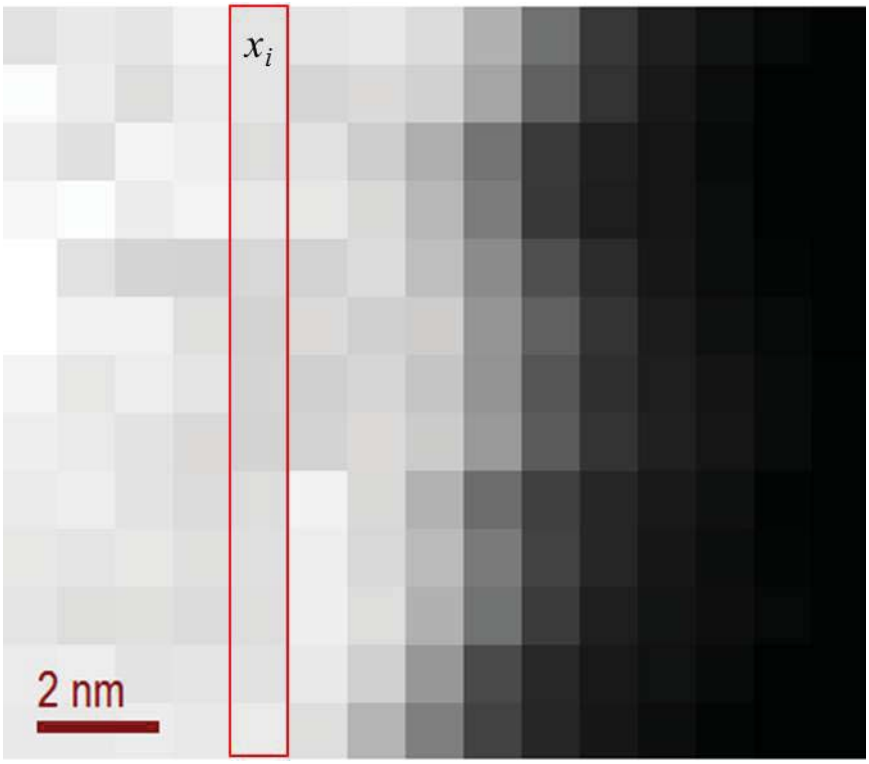

Fig. 7-2 Spectrum image at SiC/SiO_2 interface

Eq. 7-1 was built based on the assumption that the number of components and the corresponding standard spectra in the mixed system has already been known. In practice the number of chemical components may change if interactions occurred after mixing. Therefore, without a correct estimation of the number of chemical components in the system, the correct resolution seems to be impossible.

In a measured response matrix X, the chemical components in it are represented by chemical rank. However, with measurement errors present in data and other pitfalls in real chemical measurements, correct chemical rank in the two-way data is not trivial at all. If there were no measurement noises and other pitfalls in measurements, the mathematical rank (the number of independent variables and/or objects in the two-way data) and chemical rank should be the same. The determination of the mathematical rank of a noise-free matrix is trivial. A simple way is to reduce the matrix to the row-echelon form by means of Gaussian elimination and account the number of nonzero rows. However, determination of the chemical rank of a measurement data matrix is a very difficult task because of (1) the presence of measurement noise and their nonassumed distributions, (2) heteroscedasticity of the noise, (3) background and baseline shift arising from the instruments, and (4) collinearity in the measurement data. Thus, in order to avoid these pitfalls, pretreatment of two-way data and local factor analysis becomes very important.

In general, principal-component analysis (or factor analysis) is used in chemometrics to solve the problem of estimating chemical rank in two-way data because it can be used to decompose the matrix into several independent and orthogonal principal components. The number of independent and orthogonal principal components corresponds to the number of the chemical species in the mixture. The principal component analysis can be achieved by singular value decomposition (SVD) of matrix X, and the mathematical formula is expressed as following:

$$\boldsymbol{X = USV^T}$$

Here $\boldsymbol{U}$ is the column orthogonal matrix (all columns of $\boldsymbol{U}$ are orthogonal to each other). Every column in the column orthogonal matrix $\boldsymbol{U}$ is the left eigenvector of the matrix $\boldsymbol{X}$.

S is a diagonal matrix. It collects the singular values with its diagonal elements which equal to the square root of the eigenvalues of covariance matrix $\boldsymbol{X}^T\boldsymbol{X}$. $\boldsymbol{V}^T$ is a row orthogonal matrix (all the column vectors of ***V*** are orthogonal to one another). Every row in the row orthogonal matrix V^T is the right eigenvector of the matrix ***X***. The SVD of matrix X is illustrated as in Fig. 7-4. The SVD can be done in matlab as *[**U**,**S**,**V**] = SVD(**X**)*. [80]

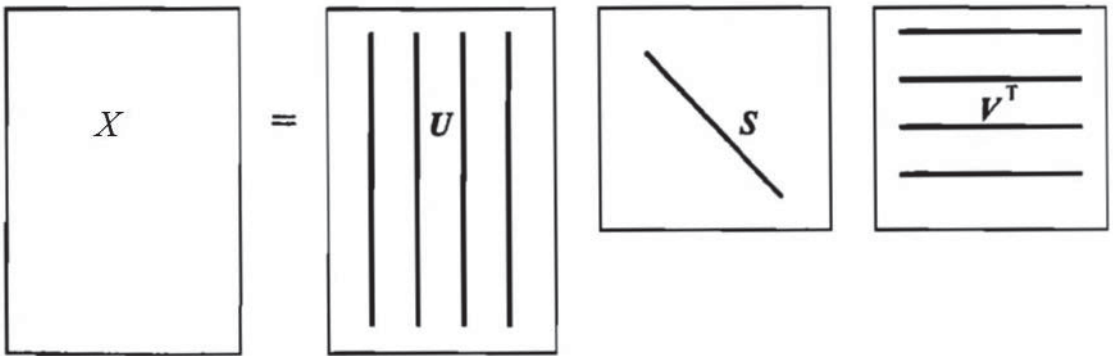

Fig. 7-3 Singular value decomposition (SVD) of matrix X

For calculation efficiency only the Si edge of an EELS spectrum (90 eV- 200 eV) was used to construct the response matrix X, since the L edge of silicon has a more significant change between SiC and SiO_2 while K edges of carbon and oxygen do not. Using the SVD method to calculate the singulars of the matrix, and the results were tabulated in Table 7-1. One can see that the first two singular values are significantly larger than the remaining twelve eigenvalues. This means only two chemical components were in the interface region, and the remaining with small singular values were from the background noise.

Table 7-1 Singular values of the response matrix *X*

Number	**Singular value/10^8**
1	5.8893
2	0.3794
3	0.0110
4	0.0029
5	0.0020
6	0.0019
7	0.0019
8	0.0018
9	0.0017
10	0.0017
11	0.0016
12	0.0015
13	0.0013
14	0.0013

The chemical rank mapping of the matrix X proved that the assumption in Eq. 7-1 was reasonable. Thus, the least square solution of the concentration matrix can be solved by

$$\boldsymbol{C} = (\boldsymbol{Y}^T\boldsymbol{Y})^{-1}\boldsymbol{Y}^T\boldsymbol{X}$$

Eq. 7-2

It is easy to perform the calculations in matlab, and the results were listed in Table 7-1. Considering the density difference of SiC and SiO_2, the concentration should be calibrated. Four SiC formula units are included in of the unit cell of 4H-SiC with the volume 82.859 $Å^3$, and three SiO_2 formula units are included in the unit cell of α-quartz with the volume 112.985 $Å^3$. Thus the number of formula unit SiC per unit volume is 1.818 times of the number of formula unit SiO_2 per unit volume. The calibrated relative concentrations of SiC were listed in the Table 7-2 too.

Table 7-2 Relative concentration of SiC and SiO_2 across the interface

SiC	**SiO_2**	**SiC Calibrated**
1	0	1.818
0.984919	0.016177	1.790583
0.959872	0.045528	1.745048
0.919753	0.092113	1.672111
0.854743	0.162952	1.553922
0.764131	0.260929	1.389189
0.642533	0.386323	1.168125
0.502251	0.527832	0.913092
0.359582	0.669625	0.65372
0.237425	0.789659	0.431638
0.142949	0.881047	0.259882
0.070605	0.947013	0.12836
0.022887	0.985331	0.041609
0	1	0

The spectrums in Fig. 7-2 were analyzed with Quantifit, and the relative atomic composition profiles of Si, C and O were shown in Fig. 7-4(a) as references. According to Table 7-2 the relative atomic composition of Si, C and O can be calculate, and the results were plotted in Fig. 7-4(b). Atomic composition ratios of C/Si and O/Si were calculated based on the data form Quantifit analyzing, chemometrics analyzing and the vicinal interface model respectively; and the results are shown in Fig. 7-5. The data calculated from the vicinal interface model was plotted to 6.9 nm, because beyond 7 nm

the terraced interface is end. The results from Quantifit analyzing, chemometrics analyzing are very close, and both of them agree with the vicinal interface model. What's more, the chemometrisc method can be used in the whole range of the measured range across the interface, and the results can be compared with the results from Quantifit analyzing. The results showed no stoichiometric change at SiC/SiO_2 interface. The interface is crystallographically rough but chemically abrupt.

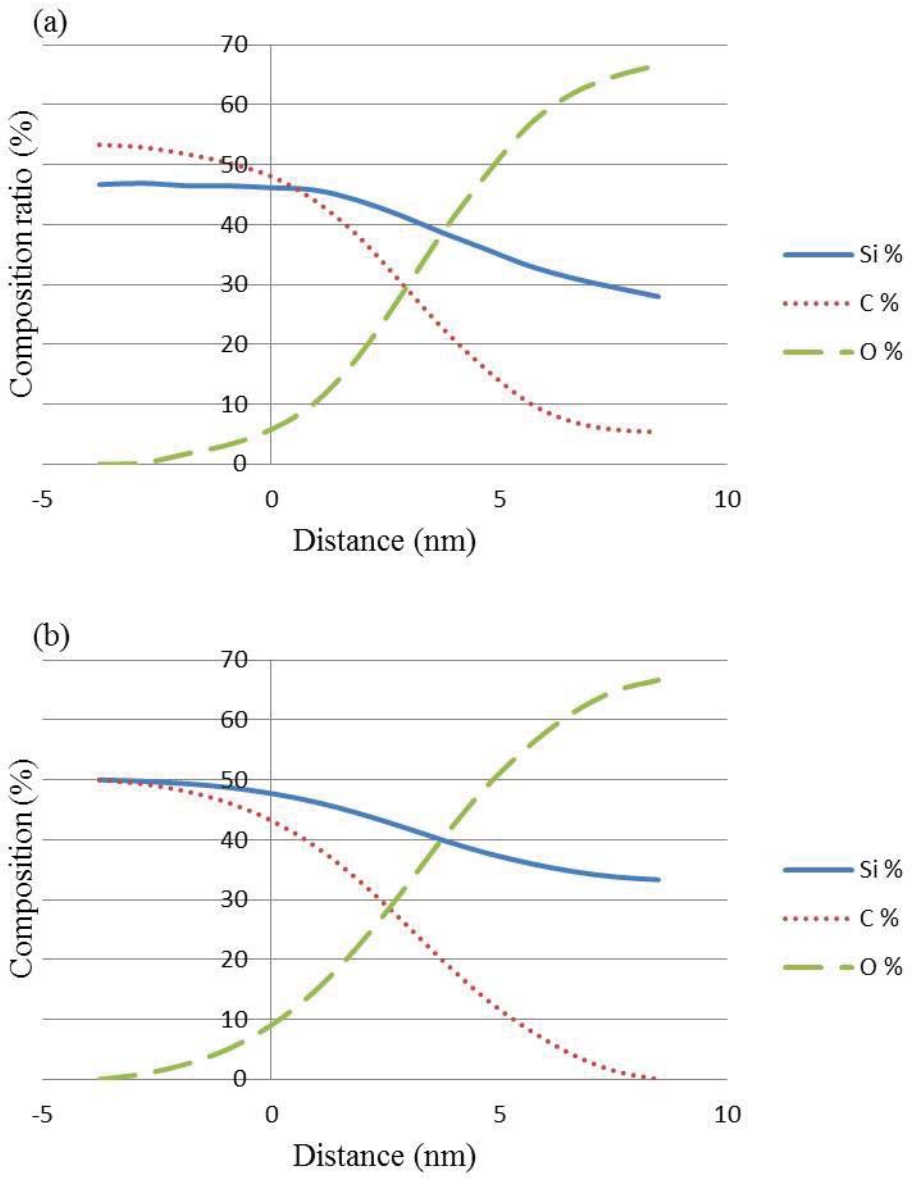

Fig. 7-4 (a) Relative atomic composition profiles of Si, C and O extracted with Quantifit. (b) Relative atomic composition profiles of Si, C and O calculated with chemometrics method.

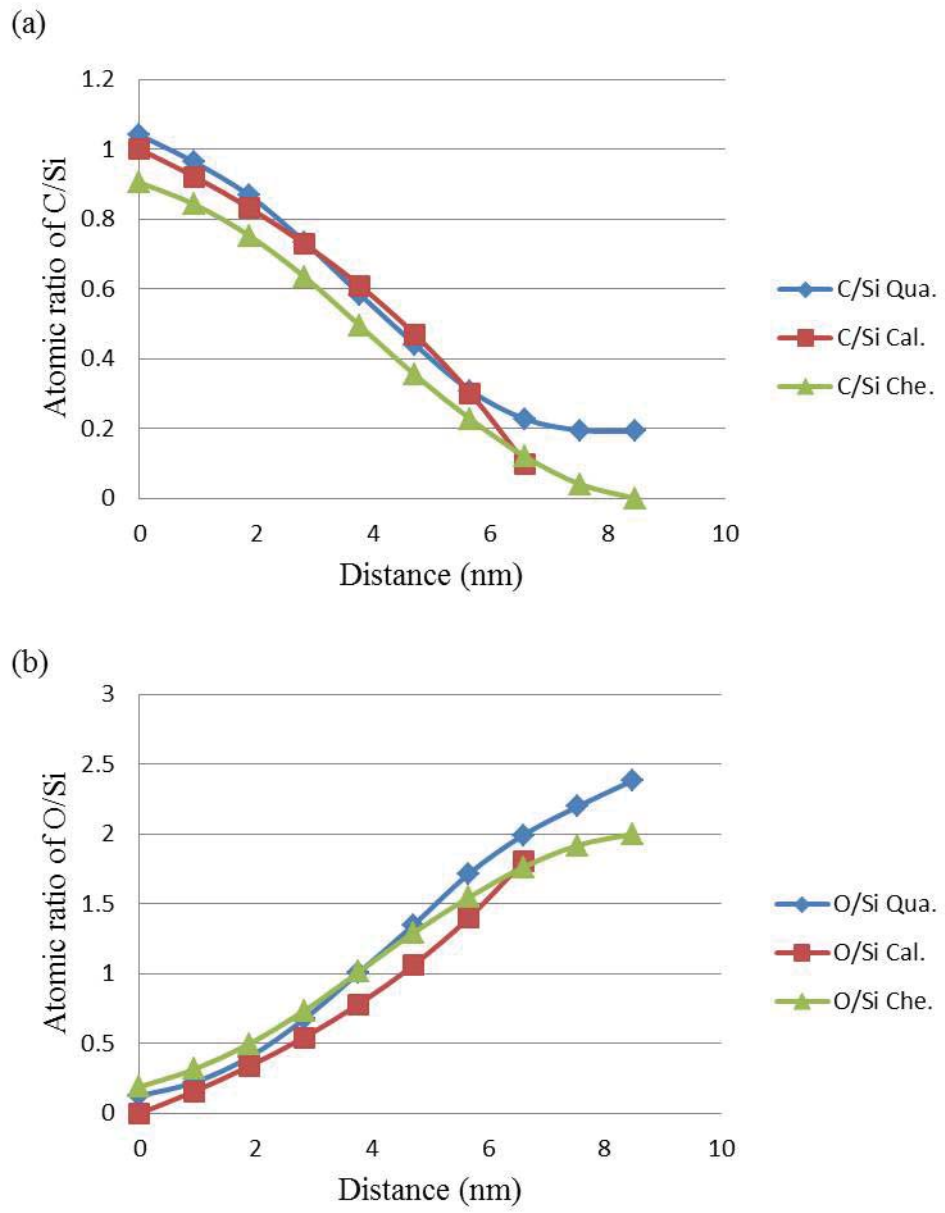

Fig. 7-5 (a) Atomic ratio of C/Si and (b) atomic ratio of O/Si. Data from Quantifit analyzing is plotted with blue diamond curve, data from the vicinal interface model is plotted with red square curve and data from chemometrics analyzing is plotted with green triangle curve.

Chapter 8. DISSCUSSION AND CONCLUSION

The structure of kinks, steps, terraces and facets at the SiC/SiO_2 vicinal interface were atomically resolved. The atomic steps and facets deviating from the ideal off-axis cut plane caused the atomic scale roughness of the interface. Comparing the roughness of the off-axis cut interface with that of the on-axis cut interface, they have the same intrinsic value of ~2 nm. That means the roughness is independent of crystallographic orientation, which explains that no distinct mobility anisotropy when the MOSFET channel direction varies on (0001) plane [27, 81, 82].

Chemical compositions of Si, C and O across the SiC/SiO_2 interface were quantitatively determined with a new model based method. The results showed no stoichiometric change. And a chemometrics approach conformed to this conclusion. The transition region was caused by roughness of the interface.

An ideal vicinal surface with periodically distributed terraces and steps would not introduce any mobility degradation because Bloch waves with the periodicity of the steps would allow the electrons to move without scattering. Any deviation from this periodicity at the interface will act as scattering centers. In Si/SiO_2 interfaces a 0.09 Å displacement of Si atoms in a monolayer could affect electronic transport close to the interface and lower the inversion-layer mobility [43]. Similarly these kinks and steps in SiC/SiO_2 interface should be electrically active and be a source of mobility degradation whether the current runs parallel, perpendicular or in a random orientation to the step ledge. However, the Si/SiO_2 interface and SiC/SiO_2 interface are different.

The Si/SiO_2 interface is crystallographically abrupt but chemically rough. The suboxide and oxygen protrusions deviate from the ideal crystal plane for few atomic layers, which is a short-wavelength fluctuation, or an elemental interface roughness defects. The significant reduction in low-electron-density mobilities observed in Si based MOSFETs are due to long-wavelength channel thickness fluctuations, and not to scattering from elemental interface roughness defects. Improved device fabrication processes that reduce or eliminate these long-wavelength fluctuations could result in a mobility increase of up

to 100% [45]. In Si based devices, bulk mobilities are only cut by a factor of two in the channel adjacent to the Si/SiO_2 interface [23].

In contrast to the Si/SiO_2 interface, the SiC/SiO_2 interface is crystallographically rough but chemically abrupt. The roughness of the SiC/SiO_2 interface is about 2 nm, which is larger than the short-wavelength fluctuation at Si/SiO_2 interface. The observed step bunching causes nano-facets, which also likely change the atomic structure of the interface and scatter the electrons heavier. Steps reduced the electron mobility of graphene film grown on SiC vicinal surface to one tenth of the mobility at terrace regions [83]. On the other hand, the composition profiles demonstrated that there was no suboxide at SiC/SiO_2 interface, or more conservatively speaking, very rear Si suboxide existed at the SiC kinks. A chemically sharp SiC/SiO_2 interface model was shown in Fig. 8-1 [84]. The two dimensional 2D periodic supercell "slab" contained four (0001) double-layers of 4H-SiC and two SiO_2 layers, and the SiC surface is terminated without defects or dangling bonds. In this short range the change from SiC to SiO_2 is chemically abrupt, and the interface would be disturbed by roughness in a longer range. In SiC/SiO_2 interface, the roughness causes both short-wavelength and long-wavelength fluctuations, which is inherent to the interface. The interface electrons with an 2D nature in the channel of SiC MOSFETs may be especially susceptible to these scattering centers caused by the imperfect vicinal interface [85]. Interface roughness act as 2D scattering centers, which contribute to the reduced electron channel mobility.

The rough interface decreased not only the channel mobility, but also the reliability of the MOSFETs. The reliability of SiO_2 dielectric layer in a SiC MOSFET is determined by tunneling current, and the tunneling current is exponentially dependent on the electric field in the dielectric [86]. Electric field will be enhanced on the kink protrusions through the edge effect. The locally strong electric field may greatly increase the failure possibilities of the dielectric layer at the SiC/SiO_2 interface, which in turn would reduce the reliability of SiC MOSFETs.

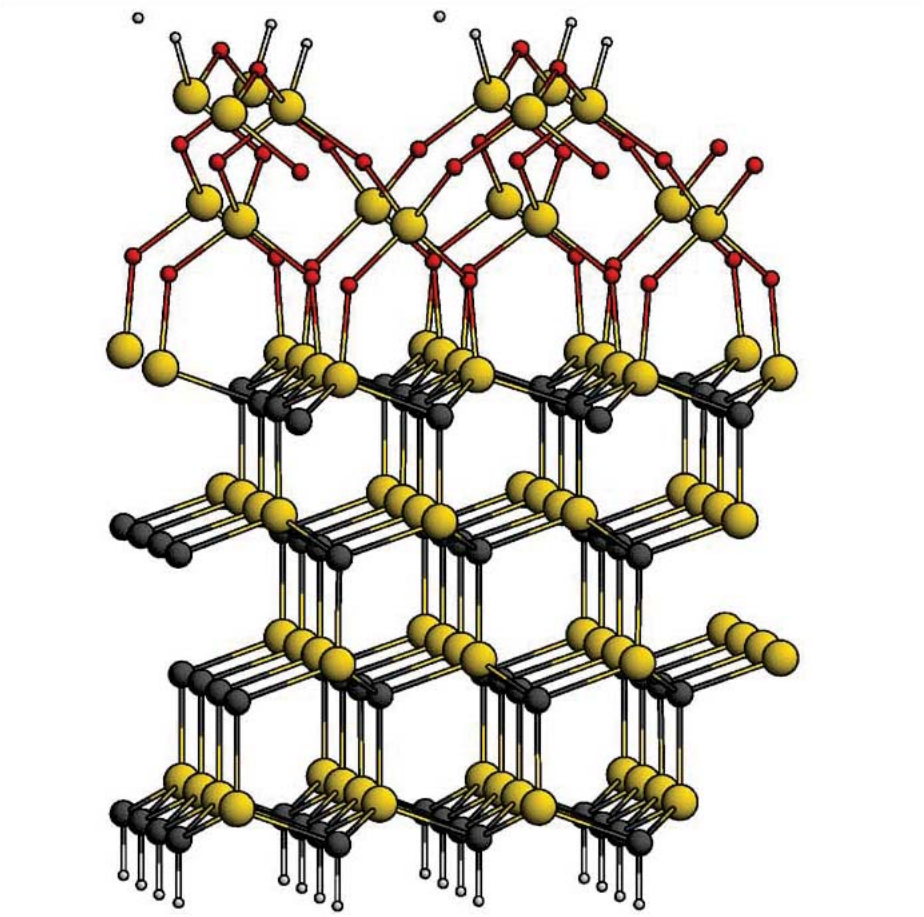

Fig. 8-1 The chemically sharp SiC/SiO_2 interface mode. O, small red spheres; C, medium sized black spheres; Si, large, yellow spheres, H, small light grey sphere [84].

8.1. Conclusion

A 3D atomic structure of SiC/SiO_2 vicinal interface was directly resolved for the first time by a powerful 5^{th} order aberration corrected STEM. EELS spectra were quantified via a new model based method and chemical compositions at the SiC/SiO_2 interface were extracted from the model based quantification more precisely than ever. The compositions of the SiC/SiO_2 vicinal interface were also calculated via a vicinal interface model and a chemometrics approach. All the results agree and from these findings it is concluded that steps and facets deviating from an ideal crystal plane caused the roughness of the of SiC/SiO_2 interface. The crystallographic roughness of the interface gave rise to the contrast of transition layers reported in the literature. The compositions at interface were stoichiometric SiC and SiO_2, and the fluctuations were due to the roughness of the vicinal interface. The roughness can be reduced by anneal to its intrinsic value of less than 2 nm. This roughness is a most likely feature of the SiC/SiO_2 interface that could contribute to the reduced electron channel mobility and reliability of the MOSFETs.

LIST OF REFERENCES

1. Saddow, S.E. and A. Agarwal, eds. *Advances in Silicon Carbide Processing and Applications*. 2004, Artech House. 228.
2. Tairov, Y.M. and V.F. Tsvetkov, *Investigation of growth processes of ingots of silicon carbide single crystals.* Journal of Crystal Growth, 1978. **43**(2): p. 209-212.
3. Brezeanu, G. *Silicon carbide (SiC): a short history. an analytical approach for SiC power device design*. in *Semiconductor Conference, 2005. CAS 2005 Proceedings. 2005 International*. 2005.
4. Wikipedia, *http://en.wikipedia.org/wiki/Silicon_carbide*.
5. Roccaforte, F., et al., *Surface and interface issues in wide band gap semiconductor electronics.* Applied Surface Science, 2010. **256**(19): p. 5727-5735.
6. 江东亮, et al. (2005) *中国材料工程大典 第8 卷 无机非金属材料.*
7. 王占国, 陈立泉, and 屠海令, eds. *中国材料工程大典 第11 卷 信息公粮材料工程（上）*. Vol. 11. 2005, 化学工业出版社: 北京.
8. Millan, J., *Wide band-gap power semiconductor devices.* Circuits, Devices & Systems, IET, 2007. **1**(5): p. 372-379.
9. Heine, V., C. Cheng, and R.J. Needs, *A COMPUTATIONAL STUDY INTO THE ORIGIN OF SIC POLYTYPES.* Materials Science and Engineering B-Solid State Materials for Advanced Technology, 1992. **11**(1-4): p. 55-60.
10. Palisaitis, J., R. Vasiliauskas, and G. Ferro (2008) *Epitaxial growth of thin films, Physics of Advanced Materials Winter School*.
11. Kelly, J.F., G.R. Fisher, and P. Barnes, *Correlation between layer thickness and periodicity of long polytypes in silicon carbide.* Materials Research Bulletin, 2005. **40**(2): p. 249-255.
12. Deal, B.E., *The Oxidation of Silicon in Dry Oxygen, Wet Oxygen, and Steam.* Journal of The Electrochemical Society, 1963. **110**(6): p. 527-533.
13. Bose, B.K., *Global Warming: Energy, Environmental Pollution, and the Impact of Power Electronics.* Industrial Electronics Magazine, IEEE, 2010. **4**(1): p. 6-17.
14. Chelnokov, V.E., *SiC bipolar devices.* Materials Science and Engineering B-Solid State Materials for Advanced Technology, 1992. **11**(1-4): p. 103-111.

15. Sei-Hyung, R., et al. *10 kV, 5A 4H-SiC Power DMOSFET*. in *Power Semiconductor Devices and IC's, 2006. ISPSD 2006. IEEE International Symposium on*. 2006.
16. Hull, B., et al. *Proceedings of ECSCRM 2008, Sep 7-11, Barcelona, Spain (2008)*. 2008.
17. Callanan, R.J., et al. *Recent progress in SiC DMOSFETs and JBS diodes at Cree*. in *Industrial Electronics, 2008. IECON 2008. 34th Annual Conference of IEEE*. 2008.
18. CREE. Available from: http://www.cree.com/Power/Products.
19. Kasap, S.O., ed. *Principles of Electronic Materials and Devices*. Third Edition ed. 2005.
20. Honstein, G., C. Chatillon, and F. Baillet, *Thermodynamic approach to the vaporization and growth phenomena of SiC ceramics. II. The SiC surface under oxidative conditions.* Journal of the European Ceramic Society, 2012. **32**(5): p. 1137-1147.
21. Senzaki, J., et al., *Excellent effects of hydrogen postoxidation annealing on inversion channel mobility of 4H-SiC MOSFET fabricated on (11(2)over-bar-0) face.* Ieee Electron Device Letters, 2002. **23**(1): p. 13-15.
22. Dhar, S., et al., *Effect of nitric oxide annealing on the interface trap density near the conduction bandedge of 4H-SiC at the oxide/(11(2)over-bar0) 4H-SiC interface.* Applied Physics Letters, 2004. **84**(9): p. 1498-1500.
23. Pantelides, S.T., et al., *Si/SiO2 and SiC/SiO2 Interfaces for MOSFETs – Challenges and Advances.* Materials Science Forum, 2006. **527-529**: p. 935-948.
24. Chung, G.Y., et al., *Nitrogen passivation of deposited oxides on n 4H–SiC.* Applied Physics Letters, 2002. **81**(22): p. 4266-4268.
25. Jamet, P., S. Dimitrijev, and P. Tanner, *Effects of nitridation in gate oxides grown on 4H-SiC.* Journal of Applied Physics, 2001. **90**(10): p. 5058-5063.
26. Sharma, Y.K., et al., *High-Mobility Stable 4H-SiC MOSFETs Using a Thin PSG Interfacial Passivation Layer.* Electron Device Letters, IEEE, 2013. **34**(2): p. 175-177.

27. Lu, C.-Y., et al., *Effect of process variations and ambient temperature on electron mobility at the SiO₂/4H-SiC interface.* Electron Devices, IEEE Transactions on, 2003. **50**(7): p. 1582-1588.
28. Wang, Y., et al., *The Effect of Gate Oxide Processes on the Performance of 4H-SiC MOSFETs and Gate-Controlled Diodes.* Electron Devices, IEEE Transactions on, 2008. **55**(8): p. 2046-2053.
29. Ryu, S.H., et al., *Critical Issues for MOS Based Power Devices in 4H-SiC.* Materials Science Forum, 2009. **615-617**: p. 743-748.
30. Sharma, Y.K., et al., *Phosphorous passivation of the SiO2/4H–SiC interface.* Solid-State Electronics, 2012. **68**(0): p. 103-107.
31. Roccaforte, F., et al., *Critical issues for interfaces to p-type SiC and GaN in power devices.* Applied Surface Science, 2012. **258**(21): p. 8324-8333.
32. Chang, K.C., et al., *High-resolution elemental profiles of the silicon dioxide/4H-silicon carbide interface.* Journal of Applied Physics, 2005. **97**(10).
33. Chang, K.C., et al., *High-carbon concentrations at the silicon dioxide-silicon carbide interface identified by electron energy loss spectroscopy.* Applied Physics Letters, 2000. **77**(14): p. 2186-2188.
34. Zheleva, T., et al., *Transition layers at the SiO2/SiC interface.* Applied Physics Letters, 2008. **93**(2): p. 3.
35. Biggerstaff, T.L., et al., *Relationship between 4H-SiC/SiO2 transition layer thickness and mobility.* Applied Physics Letters, 2009. **95**(3).
36. Shen, X., et al., *Excess carbon in silicon carbide.* Journal of Applied Physics, 2010. **108**(12).
37. Zhu, X.G., et al., *Structure and stoichiometry of (0001) 4H-SiC/oxide interface.* Applied Physics Letters, 2010. **97**(7).
38. Watanabe, H., et al., *Synchrotron x-ray photoelectron spectroscopy study on thermally grown SiO2/4H-SiC(0001) interface and its correlation with electrical properties.* Applied Physics Letters, 2011. **99**(2): p. 3.
39. Taillon, J.A., et al., *Systematic structural and chemical characterization of the transition layer at the interface of NO-annealed 4H-SiC/SiO2 metal-oxide-semiconductor field-effect transistors.* Journal of Applied Physics, 2013. **113**(4).

40. Gurevich, A.B., et al., *Heterogeneous nucleation of oxygen on silicon:Hydroxyl-mediated interdimer coupling on Si(100)-(2×1).* Physical Review B, 1998. **58**(20): p. R13434-R13437.
41. Windl, W., et al., *Characterization and Modeling of Atomically Sharp Perfect Si:Ge/SiO2 Interfaces.* ECS Transactions, 2006. **3**(7): p. 539-549.
42. Buczko, R., S.J. Pennycook, and S.T. Pantelides, *Bonding Arrangements at the Si-SiO_2 and SiC-SiO_2 Interfaces and a Possible Origin of their Contrasting Properties.* Physical Review Letters, 2000. **84**(5): p. 943-946.
43. Bongiorno, A., et al., *Transition Structure at the Si(100)SiO_2 Interface.* Physical Review Letters, 2003. **90**(18): p. 186101.
44. Li, G., *Growth and Properties of Boron Phosphide Films on Silicon Carbide*, in *Department of Material Science and Engineering*. 2013, the University of Tennessee: Knoxville.
45. Evans, M.H., et al., *First-Principles Mobility Calculations and Atomic-Scale Interface Roughness in Nanoscale Structures.* Physical Review Letters, 2005. **95**(10): p. 106802.
46. Powell, J.A., et al., *IMPROVED BETA-SIC HETEROEPITAXIAL FILMS USING OFF-AXIS SI SUBSTRATES.* Applied Physics Letters, 1987. **51**(11): p. 823-825.
47. Choyke, W.J., H. Matsunami, and G. Pensl, *Silicon Carbide: Recent Major Advances*. 2004, Berlin: Springer.
48. Burton, W.K., N. Cabrera, and F.C. Frank, *The Growth of Crystals and the Equilibrium Structure of their Surfaces.* Philosophical Transactions of the Royal Society of London. Series A, Mathematical and Physical Sciences, 1951. **243**(866): p. 299-358.
49. Lagally, M.G. and Z. Zhang, *Materials science: Thin-film cliffhanger.* Nature, 2002. **417**(6892): p. 907-910.
50. Tegenkamp, C., *Vicinal surfaces for functional nanostructures.* Journal of Physics: Condensed Matter, 2009. **21**(1): p. 013002.
51. Williams, D.B. and C.B. Carter, *Transmission Electron Microscopy: A Textbook for Materials Science*. 2009, New York: Springer.

52. Jesson, D.E. and S.J. Pennycook, *Incoherent Imaging of Thin Specimens Using Coherently Scattered Electrons.* Proceedings of the Royal Society of London. Series A: Mathematical and Physical Sciences, 1993. **441**(1912): p. 261-281.
53. Jesson, D.E. and S.J. Pennycook, *Incoherent Imaging of Crystals Using Thermally Scattered Electrons.* Proceedings of the Royal Society of London. Series A: Mathematical and Physical Sciences, 1995. **449**(1936): p. 273-293.
54. Nion_Company. Available from: http://www.nion.com/products.html.
55. Mullejans, H. and J. Bruley, *ELECTRON-ENERGY-LOSS SPECTROSCOPY (EELS) - COMPARISON WITH X-RAY-ANALYSIS.* Journal De Physique Iv, 1993. **3**(C7): p. 2083-2092.
56. GlobalSino. *http://www.globalsino.com/micro/TEM/TEM9998.html*. 2012.
57. Duscher, G. *Electron Energy Loss Spectroscopy*. Available from: http://web.utk.edu/~gduscher/eels.html.
58. Abrahams, M.S. and C.J. Buiocchi, *Cross-sectional specimens for transmission electron microscopy.* Journal of Applied Physics, 1974. **45**(8): p. 3315-3316.
59. Biggerstaff, T.L., *Atomic Scale Characterization of the Origin of Mobility Loss at the SiC/SiO_2 Interface*, in *Materials Science and Engineering*. 2008, North Carolina State University: Raleigh.
60. Wirth, R., *Focused Ion Beam (FIB) combined with SEM and TEM: Advanced analytical tools for studies of chemical composition, microstructure and crystal structure in geomaterials on a nanometre scale.* Chemical Geology, 2009. **261**(3–4): p. 217-229.
61. Kato, N.I., *Reducing focused ion beam damage to transmission electron microscopy samples.* Journal of Electron Microscopy, 2004. **53**(5): p. 451-458.
62. GmbH, C.Z.N., ed. *AURIGA series Modular CrossBeam workstation Instruction Manual*. 2010.
63. Zeiss_Company. Available from: http://microscopy.zeiss.com/microscopy/en_de/products/fib-sem-instruments/auriga.html#introduction.
64. GmbH, C.Z.N., ed. *Libra 200 Operation Manual*.

65. Egerton, R.F., *Electron Energy-Loss Spectroscopy in the Electron Microscope*. 3rd ed. 2011, New York: Springer.
66. *EELS Analysis Help Manual 1.8.2*, Gatan Inc.
67. Krawczyk, M., et al., *Measured electron IMFPs for SiC.* Surface and Interface Analysis, 2006. **38**(4): p. 644-647.
68. Verbeeck, J. and S. Van Aert, *Model based quantification of EELS spectra.* Ultramicroscopy, 2004. **101**(2-4): p. 207-224.
69. Verbeeck, J. and G. Bertoni, *Model-based quantification of EELS: is standardless quantification possible?* Microchimica Acta, 2008. **161**(3-4): p. 439-443.
70. Duscher, G. *Quantifit*. Available from: http://web.utk.edu/~gduscher/Quantifit/index.html.
71. Hofer, F. and P. Golob, *QUANTIFICATION OF ELECTRON ENERGY-LOSS SPECTRA WITH K-SHELL AND L-SHELL IONIZATION CROSS-SECTIONS.* Micron and Microscopica Acta, 1988. **19**(2): p. 73-86.
72. Rost, M., P. Šmilauer, and J. Krug, *Unstable epitaxy on vicinal surfaces.* Surface Science, 1996. **369**(1–3): p. 393-402.
73. Verga, A., *Vicinal surface growth: bunching and meandering instabilities.* cond-mat.mes-hall, 2012: p. arXiv:1207.4354v1.
74. Kramer, J., et al., *Growth and surface morphology: epitaxial MgO films and the Ag(1,1,19) substrate.* Surface Science, 2003. **537**(1–3): p. 265-275.
75. Tegenkamp, C., et al., *Stepped NaCl films grown epitaxially on Si-precovered vicinal Ge(100).* Surface Science, 2000. **466**(1–3): p. 41-53.
76. Wold, S., *Chemometrics; what do we mean with it, and what do we want from it?* Chemometrics and Intelligent Laboratory Systems, 1995. **30**(1): p. 109-115.
77. Brown, S.D., *Has the chemometrics revolution ended? Some views on the past, present and future of chemometrics.* Chemometrics and Intelligent Laboratory Systems, 1995. **30**(1): p. 49-58.
78. Liang, Y.-Z., O.M. Kvalheim, and R. Manne, *White, grey and black multicomponent systems: A classification of mixture problems and methods for their quantitative analysis.* Chemometrics and Intelligent Laboratory Systems, 1993. **18**(3): p. 235-250.

79. Liang, Y.-Z. and R.-Q. Yu, *化学计量学 （Chemometrics）*. 2003, 北京: 高等教育出版社.

80. CHAU, F.-T., et al., *Chemometrics: from basics to wavelet transform*. 2004, Hoboken, New Jersey: John Wiley & Sons, Inc.,.

81. Yano, H., et al., *High channel mobility in inversion layers of 4H-SiC MOSFETs by utilizing (112~0) face*. Electron Device Letters, IEEE, 1999. **20**(12): p. 611-613.

82. Liu, G., *private communication, Dept. Electrical & Computer Engineering, Rutgers University*.

83. Kuramochi, H., et al., *Role of atomic terraces and steps in the electron transport properties of epitaxial graphene grown on SiC*. AIP Advances, 2012. **2**(1): p. -.

84. Knaup, J.M., et al., *Theoretical study of the mechanism of dry oxidation of 4H-SiC*. Physical Review B, 2005. **71**(23): p. 235321.

85. Potbhare, S., et al., *A quasi-two-dimensional depth-dependent mobility model suitable for device simulation for Coulombic scattering due to interface trapped charges*. Journal of Applied Physics, 2006. **100**(4): p. -.

86. Singh, R. and A.R. Hefner, *Reliability of SiC MOS devices*. Solid-State Electronics, 2004. **48**(10–11): p. 1717-1720.

VITA

Peizhi Liu was born in Biyang county, Henan province in China, where he finished his primary and secondary education. Then he enrolled in the Central South University in Hunan province and obtained a Bachelor of Engineering in Materials Science and Engineering in June 2009. After that he was recommended to continue his education in the graduate school of Central South University, and in the summer of 2010 he obtained a scholarship from China Scholarship Council to pursuit his PhD study abroad.

In fall 2010 Peizhi enrolled in the graduate school of the University of Tennessee and started his PhD study with the major of Materials Science and Engineering under Dr. Gerd Duscher. During his PhD study Peizhi was a research assistant in Dr. Duscher's research group. Peizhi's research mainly focused on the structural characterizations and property analyses of semiconductor interfaces and 2D materials at atomic level by using analytical electron microscopy. Beside his research, Peizhi also worked as a teaching assistant in the advanced electron microscope laboratory of the Joint Institute for Advanced Materials, the University of Tennessee. Along his way to PhD, Peizhi earned a concurrent Master of Science degree in December of 2012.